5

Millimeter-Wave Materials

Hitoshi Ohsato
Nagoya Industrial Science Research Institute and Nagoya Institute of Technology, Nagoya, Japan
Microelectronics Research Unit, University of Oulu, Oulu, Finland

5.1 Introduction: New Frontiers of Millimeter-Wave Dielectrics

In 2013, *Nikkei Electronics* (NE) magazine [1] reported that millimeter-wave wireless communications has begun to spread to public welfare systems in Japan. Millimeter-wave communications have reached runways to takeoff after many twists and turns. Figure 5.1 shows the frequency assignments made by the Ministry of Internal Affairs and Communications (MIC) for millimeter waves from 30 GHz (1 cm) to 300 GHz (1 mm) [2]. The wireless gigabite (WiGig) for millimeter-wave wireless communications uses 60 (57 to 66) GHz and vehicle radar use 60 (60–61) GHz, 76 (76–77) GHz, and 79 (77–81) GHz.

The standard millimeter-wave communication in the 60 GHz zone converges to "IEE802.11ad.," because of its usage in a public welfare apparatus as WiGig. This has the highest data communication speed of 7 G bits per second at a short communication distance of approximately 10 m with advanced properties such as security and power control. Non-compressed millimeter-wave wireless communications with a high data transfer rate [3] have been developed to support the individual system interface, which connects PC peripheral devices and a data bus for high definition television (HDTV), monitors, and projectors, as shown in Figure 5.2a. Furthermore, millimeter-wave communication can be applied to radar for pre-crash safety systems [4], as shown in Figure 5.2b. Although the 60 GHz zone was assigned in Japan in 1995, the 76 GHz zone is used now, which is also the assigned one internationally. The 79 GHz zone is designed for next generation millimeter-wave radar. The 79 GHz radar is better than the 76 GHz radar in terms of distance, speed, and angle resolutions. However, the detection distance of 76 GHz is better than that of

Microwave Materials and Applications, First Edition.
Edited by Mailadil T. Sebastian, Rick Ubic and Heli Jantunen.
© 2017 John Wiley & Sons, Ltd. Published 2017 by John Wiley & Sons, Ltd.

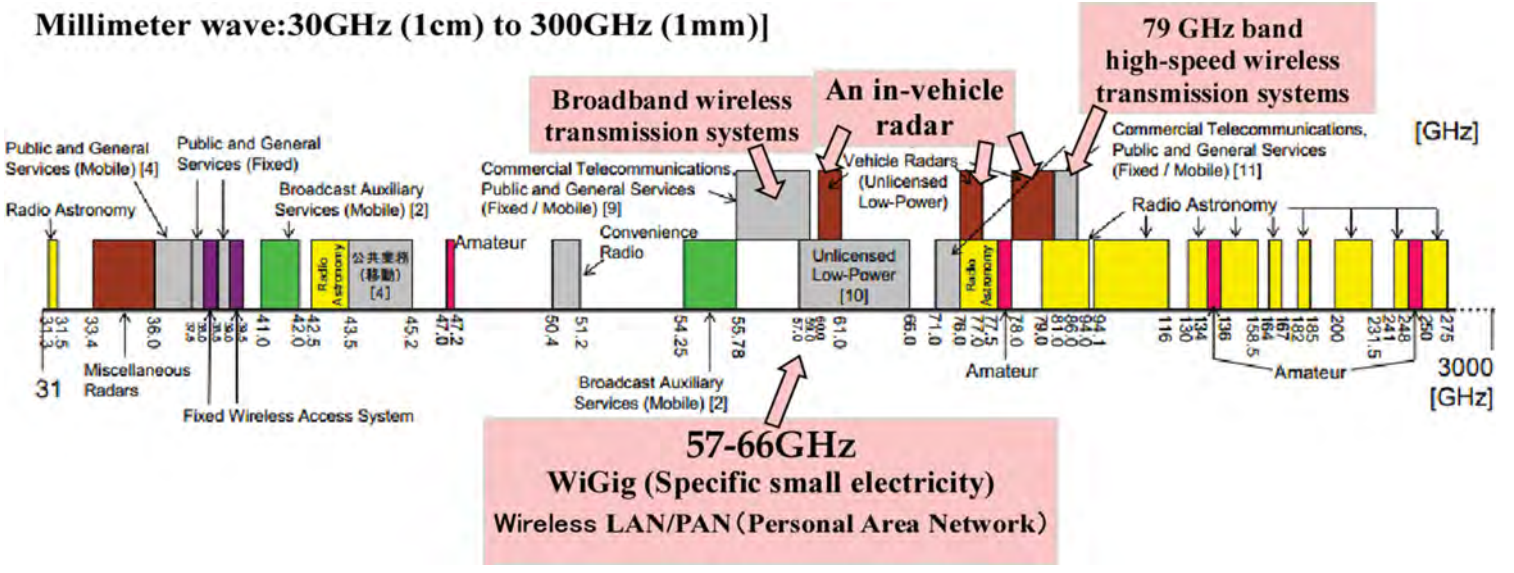

Figure 5.1 *Millimeter-wave layout list of 30 GHz (1 cm) to 300 GHz (1 mm) of Ministry of Public Management, Home Affairs, Posts and Telecommunications in Japan [2].*

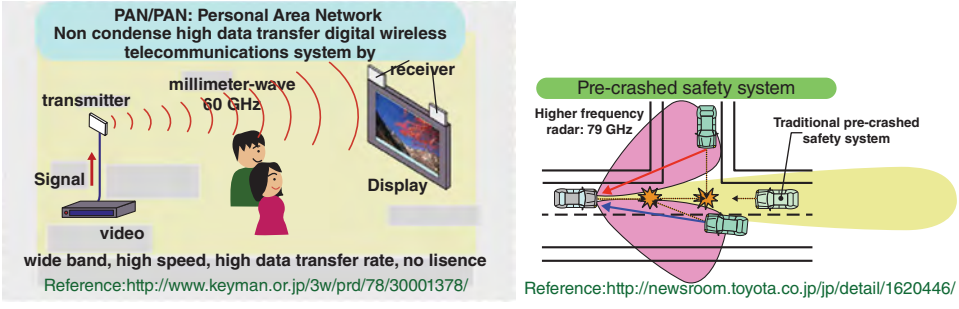

(a) (b)

Figure 5.2 *Usage of millimeter-wave: (a) Non-condense high data transfer digital wireless telecommunications system (LAN/PAN) [3]. (b) Millimeter-wave radar on the pre-crashed safety system [4]. Source: Reproduced with permission of TOYOTA News Release 2009.*

79 GHz. Hence the 76 GHz band is better for the detection of a distant car. On the other hand, the 79 GHz band is better for the detection of near people. Vehicle radar systems such as the advanced emergency braking system and autonomous emergency braking (AEB) are increasingly becoming essential internationally [5].

Table 5.1 shows the properties of ceramics and resin substrates for millimeter-wave communications. The ceramics exhibit superior properties on dielectric losses ($\tan\delta$), temperature coefficient of resonant frequency (τ_f), thermal conductivity, and linear expansion (CTE). The dielectric losses ($\tan\delta$) of ceramics are smaller than that of resin by one order

Table 5.1 *Properties of ceramics and resin-based substrate*

	Ceramics			Ceramics + resin	Resin	
Properties	A443 (Kyocera)	Willemite	Willemite–11 wt% TiO_2	AD1000 (Arlon)	MEGTRON4 (Panasonic)	FR-4
ε_r	9.6	6.6	9.39 (60 GHz)	10.7 (10 GHz)	3.8	4.3
$\tan\delta$	5×10^{-4}	6.8×10^{-5}	4.8×10^{-4}	23×10^{-4}	5×10^{-3}	$1.6\ 10^{-2}$
τ_f (ppm/K)	–60	–61	–0.69	178	–	–
T_g (K)	None	None	None	–	176	170
Thermal conductivity (W/mK)	–	–	3.3	0.81	–	0.34
$\sigma(x)$	6.9	–	–	8	12–14	11–13
$\sigma(z)$	6.9	10	10	20	35	60
Dimensional precision (μm)	15	–	–	–	50	75

T_g: glass-transition temperature, σ: linear expansion coefficient, –: not available.

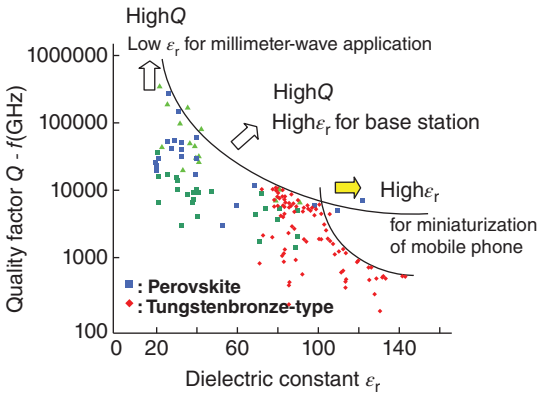

Figure 5.3 *Direction of development of microwave dielectrics designed on a figure: Qf as a function of ε_r. Source: Adapted from Ohsato et al. 2004 [9].*

of magnitude: especially, tan δ is 6.8×10^{-5} (15 GHz) for normal willemite [6,7] and 4.8×10^{-4} (60 GHz) for willemite with near zero τ_f. The τ_f is achieved near zero –0.69 ppm/K at 57.95 GHz, which is the allowable frequency for millimeter-wave radar for a vehicle [8], and for picture transmission as described in Section 5.4.2. Moreover, the thermal conductivity is also superior by three times, which is a very important property for high-density integrated devices. The linear expansion coefficient is also small by 1/6 as compared with FR-4 resin. Therefore, the use of ceramic substrates is strongly recommended for the high-quality devices in millimeter-wave communications. Moreover, mobile equipment applying low-temperature co-fired ceramics (LTCC) are integrated and reduce the size while producing high performance.

Figure 5.3 shows the three development directions of microwave dielectrics, which is presented in the variation of quality factor (Qf) as a function of the dielectric constant ε_r [9]. The Qf and ε_r are discussed in Section 5.2. The curve in Figure 5.3 shows the outline of the upper limit of Qf obtained for a given ε_r. The first direction with a high ε_r is mainly used in the miniaturization of mobile phone components. The second one, with a high Q and a high ε_r, is in demand for use in mobile phone base stations. The third direction, with a high Q and a low ε_r, is for devices working in the millimeter-wave range. This direction is the new frontiers of microwave dielectrics [5], because the utilizable frequency region is expanding towards the millimeter wave due to the shortage of conventional radio frequency (RF) regions.

Dielectrics for the microwave region [10] have been researched for a long time, with some excellent materials [11–16] developed and used for practical applications. Some of them, such as complex perovskite [14] with high quality factors are used for millimeter-wave wireless communication. Recently, millimeter applications have received much attention. The dielectrics with a high quality factor (Q), low dielectric constant (ε_r), and near-zero temperature coefficients of the resonant frequency (τ_f) are desired for usage as vehicles for millimeter-wave communication [17, 18]. Most of the useful candidate materials with low ε_r and high Qf exist in the silicates such as forsterite (Mg_2SiO_4) [19–22], willemite (Zn_2SiO_4) [23], and cordierite/indialite ($Mg_2Al_4Si_5O_{18}$) [24, 25]. The low ε_r and high Qf

is attributed to the reduced rattling in the silicate tetrahedra based on covalency, as described in Section 5.4.5 [25–28].

In this chapter, the dielectric properties for millimeter-wave materials with emphasis on silicates such as forsterite, willemite, cordierite/indialite glass ceramics and other dielectrics such as alumina, spinel, etc. are discussed.

5.2 Dielectric Properties for Millimeter Wave [29]

5.2.1 Quality Factor *Q*

Microwave dielectric materials for millimeter-wave applications are termed as millimeter-wave dielectrics [17]. The wave number increases in the millimeter-wave region, as shown in Figure 5.4a and b. Dielectric losses are generated by dielectric polarization accompanied by the electromagnetic wave. Therefore, as the wave number increases, dielectric losses also increase. The dielectric materials with low loss ($\tan\delta$), that is, high Q, are desirable for practical applications. The quality factor $Q = 1/\tan\delta$.

The presence of defects and impurities in crystals that produce polars increase losses, as shown in Figure 5.5a and b, respectively. The example of impurities present in the forsterite ceramics synthesized using high purity raw materials are given in Section 5.4.1 [17]. The presence of grain boundaries also produce polars (Figure 5.5c). Therefore the grain growth in the ceramics decreases the dielectric losses. In the case of Al_2O_3, it is found [30, 31] that the Qf values increased with grain size, as seen in Figure 5.43b. These losses, which are based on impurities and defects, are of extrinsic origin whereas intrinsic losses are based on the crystal structure such as symmetry and ordering. In the case of complex perovskite such as $Ba(Mg_{1/3}Ta_{2/3})O_3$ (BMT), $Ba(Zn_{1/3}Ta_{2/3})O_3$ (BZT), and $Ba(Zn_{1/3}Nb_{2/3})O_3$ (BZN) with order–disorder transition, high symmetry brings low loss/high Q instead of ordering [32]. The cordierite/indialite ceramics [24] is also an example of high Q materials according to high symmetry, as described at Section 5.4.3. In the case of pseudotungstenbronze solid solutions without phase transition, the compositional ordering brings low loss/high Q.

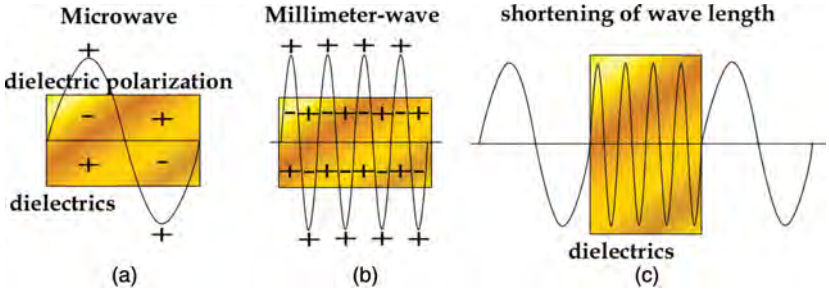

Figure 5.4 *(a) When irradiated by electromagnetic waves, the materials should resonate due to changing dielectric polarization under alternating electromagnetic fields. (b) Dielectric losses increase with an increase in frequency. (c) ε_r causes a shortening of wavelength λ in dielectrics. Source: Adapted from Ohsato [17, 32].*

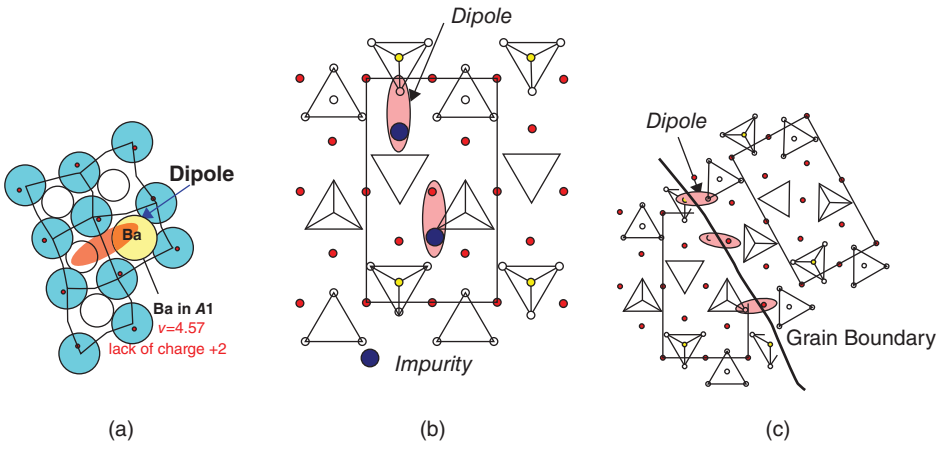

Figure 5.5 *Origin of extrinsic losses produced by (a) defects, (b) impurities), and (c) grain boundary.*

5.2.2 Dielectric Constant ε_r

The dielectric constant ε_r causes a shortening of wavelength λ in dielectrics, as shown in Figure 5.4c according to the following equation:

$$\lambda = \lambda_0/\varepsilon_r^{1/2} \tag{5.1}$$

Here, λ_0 is the wavelength in a vacuum. In the microwave region, the ε_r value is expected to be large for the miniaturization of mobile communication equipment. In the millimeter-wave region, the ε_r value is expected to be small. As the wavelength is in the millimeter order, miniaturization is not needed. There are other more important phenomena such as the time delay T_{PD} according to the following equation:

$$T_{PD} = \sqrt{\varepsilon_r}/c \tag{5.2}$$

Here, ε_r is the dielectric constant and c is the velocity of light. The time delay is desirable in order to improve the speed of the signal.

5.2.3 Temperature Coefficient of Resonant Frequency τ_f

The τ_f is required to be near 0 ppm/°C for global usage in different environmental temperatures. Millimeter-wave radar for an anticollision system is located in the extreme condition in front of the radiator, with a high temperature from the radiator and high and low temperatures from outside air in the summer time and winter time, respectively. Therefore, near zero τ_f is needed. The τ_f has a relationship with the temperature coefficient of dielectric constant τ_ε as follows:

$$\tau_f = -(\alpha + \tau_\varepsilon/2) \tag{5.3}$$

where α is the thermal expansion coefficient.

Most millimeter-wave compounds with a low ε_r have a large negative τ_f, such as alumina: –65 ppm/°C and forsterite: –70 ppm/°C. The τ_f of these millimeter-wave dielectrics was improved by two different methods. The first requires the addition of materials with the opposite sign (i.e., a positive τ_f). The addition of rutile with $\tau_f = +450$ ppm/°C can adjust the τ_f of the compound in question [19, 20, 23, 33]. The second method is to adjust the τ_f to near 0 ppm/°C by the formation of the solid–solution phases [34]. This is the preferred method because of the small degradation of *Qf*.

5.3 Candidates of Millimeter-Wave Dielectrics

The origin of ε_r was considered by differences of crystal structures, as shown in Figure 5.6 [17]. Silicates with a low ε_r are formed by the tetrahedral framework of SiO_4 (Figure 5.6a), with 45% ionic bonds and 55% covalent bonds, described later in Section 5.4.5. Covalent bonds reduce ε_r because the rattling effect of the cations in a polyhedron should reduce as a result of the high bond strength. On the other hand, titanates (Figure 5.6c), with a large ε_r such as $SrTiO_3$, are formed by a TiO_6 octahedral framework, which is almost of ionic bond and has space for ionic displacement. In the case of aluminates, although Al ions also occupy an octahedral framework, the Al ions located in the pair octahedral on the threefold axis repel each other, as shown in Figure 5.6b. The Al ions are immovable in the octahedron and produce a medium ε_r. The order of ε_r is as follows:

$$\varepsilon_{r\ \text{silicate}} < \varepsilon_{r\ \text{aluminate}} < \varepsilon_{r\ \text{titanate}}$$

Silicates with a low ε_r are good candidates for millimeter-wave dielectrics [17], and germanate and phosphate also are constructed with GeO_4 and PO_4 tetrahedron with covalent features described later in Sections 5.4.5 and 5.4.8, respectively. The important millimeter-wave dielectrics are listed in Table 5.2.

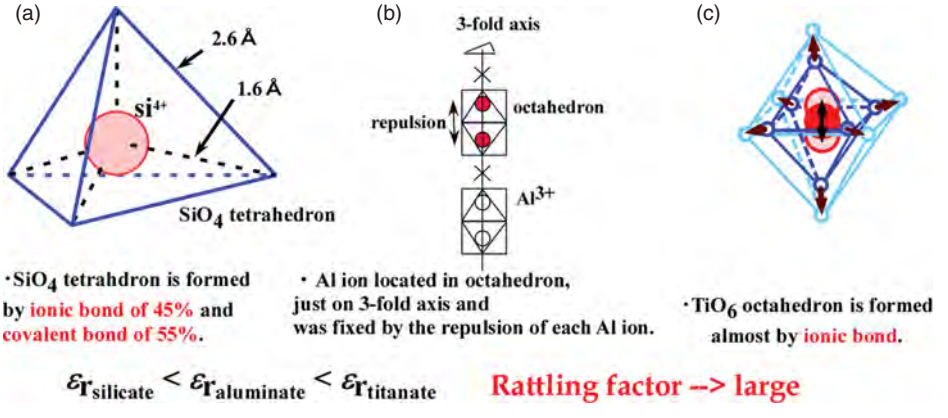

Figure 5.6 *Dielectric constants due to crystal structure: (a) SiO_4 tetrahedron, (b) Al_2O_3, and (c) TiO_6 octahedron. Source: Adapted from Ohsato 2005 [17].*

Table 5.2 *Main millimeter-wave dielectrics*

Material	ST (°C)	Crystal system	SG	ε_r	Qf (GHz)	τ_f (ppm/°C)	Reference
Mg_2SiO_4 (fosterite)	1450	Orthorhombic	*Pbnm*	6.8	270000	−67	77*
Zn_2SiO_4 (willemite)	1340	Trigonal	$R\bar{3}$	6.6	219000	−61	23
$Mg_2Al_4Si_5O_{18}$ (cordierite)	1440	Orthorhombic	*Cccm*	6.2	40000	−25	34*
Ni-doped cordierite (deform to indialite)	1390–1440	Orthorhombic/ hexagonal	*Cccm*/ *P6mcc*	6.2	99110	−30	51
Indialite (glass ceremics)	1300	Hexagonal	*P6/mcc*	4.7	210000	−27	24
$Ca_{0.99}Mg_{0.01}SiO_3$ (wollastonite)	1290/2 h	Monoclinic	$P2_1/a$	6.5	62400	−43	53*
$CaSiO_3$ + 1 wt% Al_2O_3 (wollastonite)	1250	Monoclinic	$P2_1/a$	6.7	24600		72*
α-$CaSiO_3$ (wollastonite)	1500/2 h	Monoclinic	*C2/c*	6.8	42200	−19	26
$SrSiO_3$	1540/2 h	Monoclinic	*C2/c*	6.8	13100	−66	26
$(Ca_{1-x}Sr_x)SiO_3$ ($x = 0.8$)	1490/2 h	Monoclinic	*C2/c*	6.62	66700	−40	26
$CaMgSi_2O_6$ (diopside)	1300/3 h	Monoclinic	*C2/c*	7.4	59700	−42	118*
$CaMgSi_2O_6$ (diopside)	CIP:1300	Monoclinic	*C2/c*	7.6	121380	−66	27
$MgSiO_3$ (enstatite)	1380/13 h	Orthorhombic	*Pbnm*	6.7	121200	−17	71*
Zn_2GeO_4 (Ge–willemite, olivine)	1300	Trigonal	$R\bar{3}$	6.9	102700	−32	65*
Mg_2GeO_4 (Ge–forsterite) + 3 wt% B_2O_3 (olivine)	1200/4 h	Orthorhombic	*Pnma*	6.5	91000	−28	54*
$NaAlSi_3O_8$ (albite)	1025	Triclinic	$C\bar{1}(P\bar{1})$	5.5	11200	−5	25*
$Na_{0.8}Ca_{0.2}Al_{1.2}Si_{2.8}O_8$ (plagioclase)	1100	Orthorhombic	$P\bar{1}$	5.8	17600	−7	71
$K_{0.67}Ba_{0.33}Ga_{1.33}Ge_{2.67}O_8$ (feldspar)	1020	Monoclinic	$P2_1/a$	5.9	94100	−25	72
Al_2O_3+0.5wt%TiO_2	1550/5 h	Trigonal	$R\bar{3}c$	10	453000	9	76
Al_2O_3 (corundum)	1550/5 h	Trigonal	$R\bar{3}c$	10	335000	−60	247*
Al_2O_3 (corundum)	1550	Trigonal	$R\bar{3}c$	10.1	680000	−60	18, 30
Al_2O_3 (corundum)	1400/8 h	Trigonal	$R\bar{3}c$	10	634000	−40	75
Al_2O_3 + 500 ppm TiO_2 (corundum)		Trigonal	$R\bar{3}c$	10	500000	10	74
Nano Al_2O_3 + 0.5 wt% TiO_2 (corundum)	1400	Trigonal	$R\bar{3}c$	10.8	680000	14	285
$0.9Al_2O_3$–$0.1TiO_2$ (corundum)	1300/2 h	Trigonal	$R\bar{3}c$	12.4	148000	2	77
Al_2O_3–TiO_2:MnO (corundum)	1300	Trigonal	$R\bar{3}c$	12.4	274000	0	336
$Mg_4Nb_2O_9$ (corundum)	1200/10 h	Trigonal	$P\bar{3}c1$	12.4	194000	−71	79

(*continued*)

Table 5.2 *(Continued)*

Material	ST (°C)	Crystal system	SG	ε_r	Qf (GHz)	τ_f (ppm/°C)	Reference
$Mg_4Ta_2O_9$ (corundum)	1450	Trigonal	$P\bar{3}c1$	11.5	347000	−70	80
Mg_4NbSbO_9 (corundum)	1500	Trigonal	$P\bar{3}c1$	12.5	280000	−45	338
$Mg_4(Nb_{2-x}V_x)O_9$ (x = 0.0625) (corundum)	1025	Trigonal	$P\bar{3}c1$	11.6	160250	−75	310
$Mg_4Nb_2O_{9+3}$ wt% LiF (corundum)	950/10 h	Trigonal	$P\bar{3}c1$	12.6	116410	−72	248
$MgAl_2O_4$ (spinel)	1650/3 h	Cubic	$Fd\bar{3}m$	8.5	105000	−63	85
$ZnAl_2O_4$ (spinel)	1375	Cubic	$Fd\bar{3}m$	8.5	56000	−79	33
$0.79ZnAl_2O_4$–$0.21Mg_2TiO_4$ (spinel)	1550	Cubic	$Fd\bar{3}m$	9.6	160800	−65	226∗
$MgGa_2O_4$ (Mg–gallium spinel)	1410	Cubic	$Fd\bar{3}m$	9.5	117000	−4	86
$ZnGa_2O_4$ (Zn–gallium spinel)	1385	Cubic	$Fd\bar{3}m$	10.4	94600	−27	87
$MgGa_2O_4$ (Mg–gallium spinel)	1560	Cubic	$Fd\bar{3}m$	9.2	298000	−63.5	89
$MgZn_2O_4$ (Zn–gallium spinel)	1550	Cubic	$Fd\bar{3}m$	9.8	220000	−64	88
$Mg_3B_2O_6$(MgO–25 mol% B_2O_3) (kotoite)	1320	Orthorhombic	$Pnmn$	7.2	310000	−60.6	95
$Zn_3B_2O_6$	925/4 h	Triclinic	$I2/c$	6.7	58500	−58	98
$LaBO_3$	1300	Orthorhombic	$Pmcn$	11.8	76900	−52	100
$LiMgPO_4$ (olivine)	950	Orthorhombic	$Pmnb$	6.6	79100	−60	58
$LiMg_{0.95}Co_{0.05}PO_4$ (olivine)	875/2 h	Orthorhombic	$Pmnb$	7	111200	−54	102
$SrCuP_2O_7$	925	Monoclinic	$P2_1/n$	7	101110	−62	104
$YbPO_4$ (xenotime)	1600	Tetragonal	$I4_1/amd$	8.2	71600	−28	133
$CePO_4$ (monazite)	1400/2 h	Monoclinic	$P2_1/n$	11.6	68300	−46	133
$Ca_{2+x}La_6(SiO_4)4(PO_4)O_2$ (x=2) (apatite)	1475/4 h	Hexagonal	$P6_3/m$	13.8	27900	−11	313
$Mg_3(VO_4)_2$	1050	Orthorhombic	$Cmca$	9.4	65500	−90	106
$Mg_2Co(VO_4)_2$	1000	Orthorhombic	$Cmca$	9.2	107500	−97	106
$MgCo_2(VO_4)_2$	900/5 h	Orthorhombic	$Cmca$	9.4	78900	−95	221∗
$Mg_3(VO_4)_2$–$0.2Ba_3(VO_4)_2$	950/5 h	Orthorhombic	$Cmca$	11	114000	−58	107
$Mg_3(VO_4)_2$–$0.5Ba_3(VO_4)_2$ + 0.0625 wt%	950/5 h	Orthorhombic	$Cmca$	13	74000	−6	107
$Ca_5Co_4(VO_4)_6$ (garnet)	875	Cubic	$Ia\bar{3}d$	10.1	95200	−63	259∗
MgO (periclase)	1490	Cubic	$Fm3m$	7.9	113600	16.4	141∗
MgO (periclase)	1490	Cubic	$Fm3m$	7.9	113600	16.4	141∗

ST: synthesis temperature, SG: space group,∗: Reference [42].

5.4 Specialized Study

In this section, silicate compounds, such as forsterite, willemite, indialite/cordierite glass ceramics, and other silicates such as wollastonite and diopside, are presented first. Although feldspar ceramics are mainly silicates, they are presented in the "substituted Ge for Si" section because feldspar ceramics with good properties are Ge-substituted for Si. As the germanates also show similar properties to those of silicates in terms of ionicity and covalency, Ge-forsterite, Ge-willemite, and feldspar-substituted Ge for Si are presented. Moreover, non-silicates with low ε_r and high Q, such as alumina including new-type corundum, spinel, borates, and phosphates are presented.

5.4.1 Forsterite

5.4.1.1 Synthesized High-Q Forsterite

Forsterite ceramics synthesized using high-purity raw materials are compared with commercially available materials in Table 5.3. The synthesized high-purity forsterite ceramics showed lower dielectric losses of $\tan\delta = 9.6 \times 10^{-5}$ measured at 23 GHz frequency than a commercial one of $\tan\delta = 8.4$ to 17×10^{-4} for 23 GHz, which are comparable with a quality factor Qf of 240 000 and approximately 10 000 GHz, respectively, as shown in Figure 5.7. The synthesized forsterite was single phase with high relative density of 96 to 98% [17, 35, 36]. Surface microstructures of a commercially available forsterite and that of a high-purity one are shown in Figure 5.8a and b, respectively. The higher dielectric losses of the commercial one was due to a very glassy phase among the grains, as seen in Figure 5.8a. On the other hand, synthesized forsterite ceramics have a fine grain boundary, which leads to low dielectric losses. In the texture of the grain boundaries, different configurations of grains are observed. The grains of a commercial one have many facets of crystal surface accompanied by a veryglassy phase in grain boundaries. The grains with facets, called euhedral (idiomorphic) in crystallography, appeared as the result of crystal

Table 5.3 *Dielectric, resistivity and thermal properties of commercial forsterite ceramics and high-purity forsterite ceramics sintered at 1360 °C for 2 hours*

Properties	Commercial	High purity
ε_r (23 GHz)	6.5 ~ 6.6	6.8
$\tan\delta$ (23 GHz)	$8.4 \sim 17 \times 10^{-4}$	0.96×10^{-4}
Volume resistivity (Ωm)		
100 °C	5.0×10^{11}	8.5×10^{12}
300 °C	7.0×10^{9}	1.8×10^{10}
500 °C	1.0×10^{9}	4.4×10^{8}
Coefficient of thermal expansion (ppm/°C)	25 ~ 700 °C 11.2	25 ~ 700 °C 9.4
Thermal conductivity (w/m °C) at room temperature	3.2	9.1

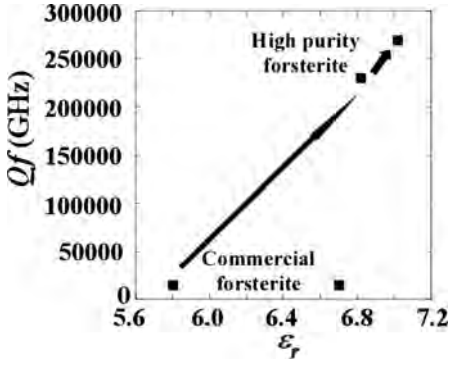

Figure 5.7 *Qf of high purity forsterite ceramics and commercial forsterite ceramics against ε_r. Dielectric losses of commercial forsterite ceramics and high Q forsterite ceramics against dielectric constants. Source: Adapted from Ohsato 2007 [35].*

growth in the liquid phase, which is introduced by impurity. The liquid phase remains as a glassy phase, as shown in Figure 5.8a. On the other hand, the high-purity forsterite ceramics have grains without facets, called anhedral (allotriomorphic), which may be due to direct contact of grains. In Table 5.3, the volume resistivity of commercial forsterite ceramics is lower than that of the high-purity one and found to depend on the glassy phase. Thermal conductivity of the high-purity one is about three times that of the commercial grade.

5.4.1.2 Adjust the Temperature Coefficient of Resonant Frequency on Forsterite

The large negative τ_f (−65 ppm/°C) of forsterite can be adjusted to near zero ppm/°C by adding rutile, which has a large positive τ_f (450 ppm/°C) [19, 20, 37]. Although pure forsterite ceramics are sintered at 1360 °C (see Table 5.3), 30 wt% rutile added to forsterite

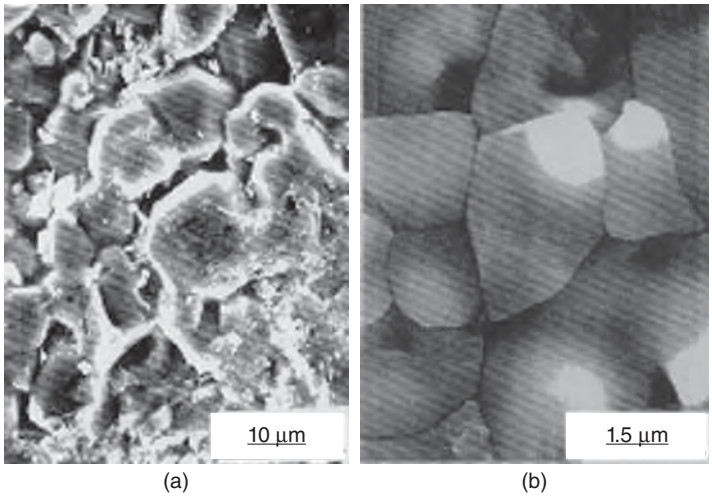

Figure 5.8 *SEM photographs of (a) commercial forsterite ceramics and (b) high purity forsterite ceramics sintered at 1360 °C. Source: Adapted from Ohsato 2007 [35].*

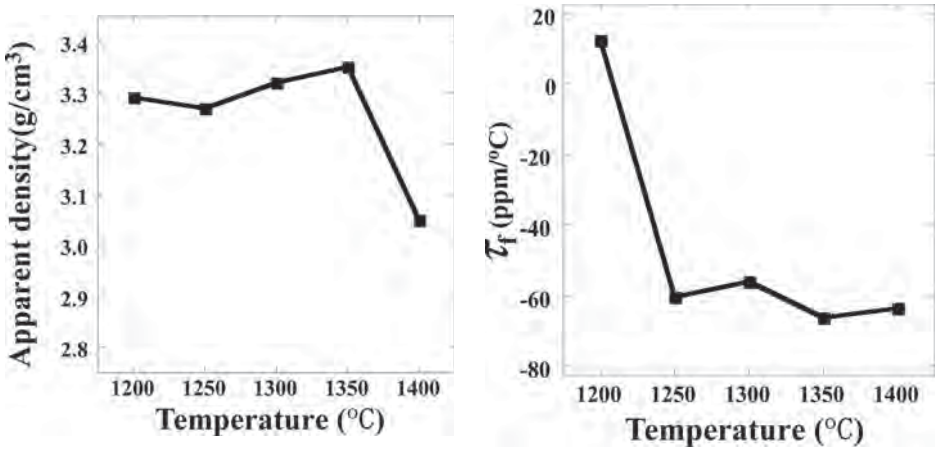

Figure 5.9 *(a) Apparent density and (b) temperature coefficient of resonant frequency of the forsterite ceramics with added 30 wt% rutile as a function of the sintering temperature. Source: Adapted from Tsunooka et al. 2004 [20].*

ceramics could be sintered at 1200 °C with high apparent density of 3.3 g/cm^3, as shown in Figure 5.9a. The added rutile acts as a sintering aid for improving the sinterability of forsterite. The τ_f of the sample sintered at 1200 °C is 12.7 ppm/°C, but the value is degraded to –60 ppm/°C suddenly on increasing the sintering temperature (Figure 5.9b). This is due to the disappearance of rutile based on the following reaction [20]:

$$Mg_2SiO_4 + 2TiO_2 \rightarrow MgTi_2O_5 + MgSiO_3 \tag{5.4}$$

As the compositions of forsterite added rutile locate in the compositional triangle Mg_2SiO_4—$MgTi_2O_5$—$MgSiO_3$ in the ternary phase diagram [39], as shown in Figure 5.10, rutile reacts with forsterite to make $MgTi_2O_5$ and enstatite as in chemical reaction (5.4).

Figure 5.11a shows τ_f and ε_r of the samples sintered at 1200 °C for 2 hours as a function of rutile content [20, 38]. The τ_f of forsterite ceramics added rutile increased linearly with the amount of rutile addition, as shown in Figure 5.11a. The τ_f changed from negative to positive values between 20 and 25 wt% addition of rutile. The τ_f showed 3.95 ppm/°C in the case of 25 wt% addition of rutile. Although ε_r values shift to a high value of 11.5 with increasing amounts of rutile (Figure 5.11b), the *Qf* values also keep a relatively high value of 80 000 HGz (Figure 5.11a). The increase of apparent density is attributed to the addition of rutile, which has a higher density (4.24 g/cm^3) than forsterite (3.22 g/cm^3). The fosterite composite with 24 wt% rutile has $\tau_f = 0$ ppm/°C, $\varepsilon_r = 11$, and $Qf = 82\,000$ GHz when sintered at 1200 °C for 2 hours. Figure 5.11c shows a backscattered SEM photograph of the forsterite with 25 wt% rutile ceramic composite sintered at 1200 °C for 2 hours. The microstructure was composed by grains of forsterite (light gray grains) and rutile crystals (white grains) and densified in the state of pore and glassy-phase free at grain boundaries. This appears to be due to the enhanced sinterability by excess rutile addition.

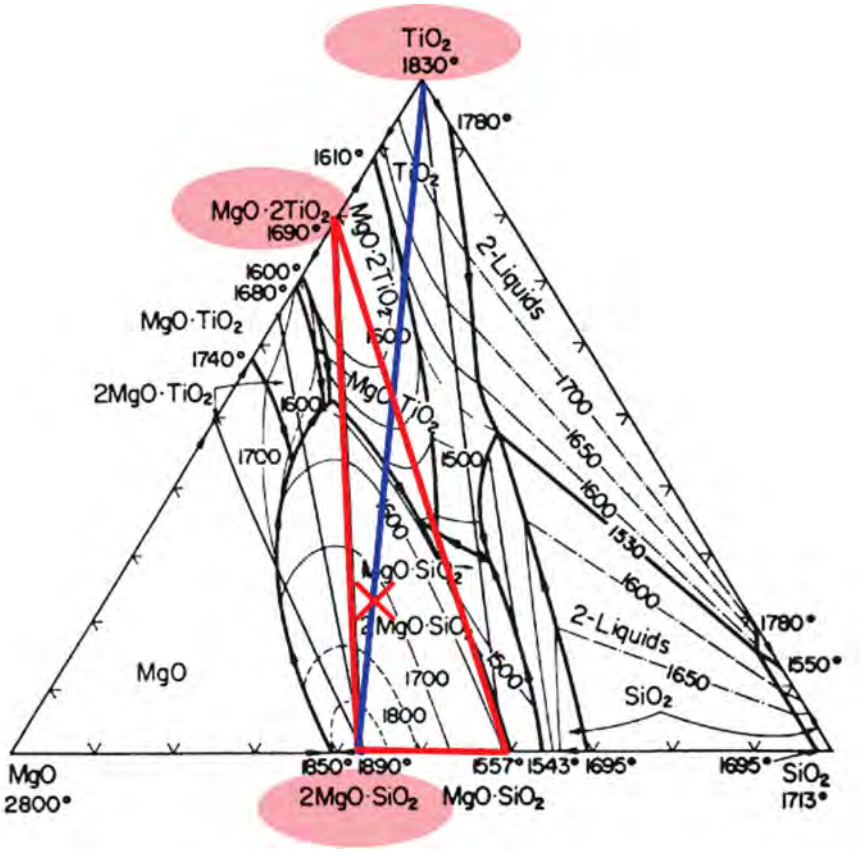

Figure 5.10 *Rutile added to forsterite located in the $2MgO{\cdot}SiO_2$—$MgO{\cdot}2TiO_2{\cdot}MgO{\cdot}SiO_2$ compositional triangle. Source: Adapted from Tsunooka et al. 2013 [38].*

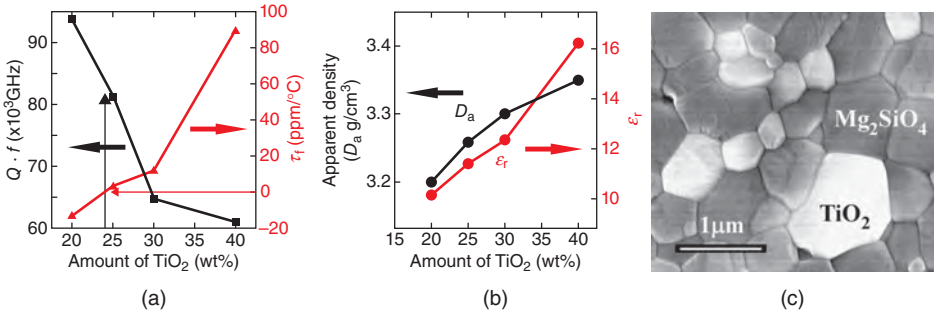

Figure 5.11 *Qf and τ_f (a) and Da and ε_r (b) of rutile added forsterite as a function of amount of TiO_2. (c) A backscattered SEM photograph of the forsterite ceramics composite with 25 wt% rutile sintered at 1,200 °C for 2 hours. Source: Adapted from Tsunooka et al. [20, 38].*

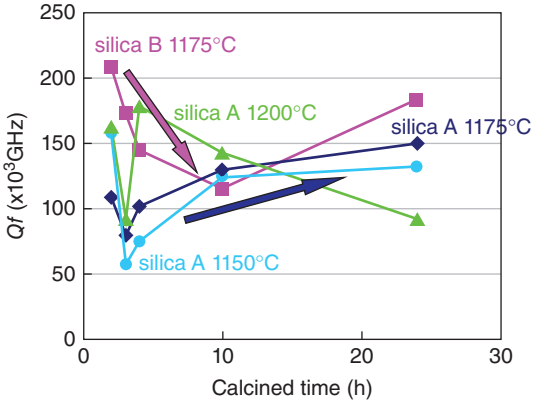

Figure 5.12 *Qf values of sintered at 1400 °C for 2 hours as a function of calcined hours. Source: Ando et al. [21, 22].*

5.4.1.3 Diffusion of Si and Mg Ions on the Formation of Forsterite

Generally, synthesis of silicates is very difficult and needs good knowledge of the raw materials with phase, shape and size, calcination and sintering conditions, pressing conditions, etc. The effects of diffusion of different elements on the formation of forsterite and the properties have been verified [21, 22]. Figure 5.12 shows the variation of *Qf* of forsterite sintered at 1400 °C for 2 hours as a function of calcination time (2–24 hours). The specimens are calcined at 1150, 1175, and 1200 °C for silica A with a crystalline form and large grain size of 0.82 μm for SiO_2 raw material and 1175 °C for silica B with an amorphous form and small size of 0.25 μm. In the case of silica A, the *Qf* values initially decrease for 2 to 4 hours calcined samples and then increase for calcination for 4 to 24 hours. Figure 5.13a and b shows XRPD patterns of specimens: silica A and silica B, respectively, which reveal two kinds of diffraction patterns for calcined and sintered specimens with different calcination duration. The XRPD patterns for calcined powder are indicated by "cal *n*h, for $n = 2, 3, 4, 10, 24$." Sintered ceramic using calcined powder "cal *n*h" is denoted by "sin *n*h." All ceramics are sintered at 1400 °C for 2 hours. All the crystalline XRPD patterns are mainly composed of forsterite. An enstatite ($MgSiO_3$) observed for silica A specimens and its content decreased with calcination duration and almost disappeared after 24 hours of calcination, resulting in a single phase forsterite, as shown in Figure 5.13a. The calcined samples show unreacted raw materials: periclase (MgO) and quartz (SiO_2). The enstatite phase was also detected in sintered specimen silica B, as shown in Figure 5.13b. However, the amount of enstatite in sintered specimens did not decrease but increased with calcination duration up to 10 hours and suddenly almost disappeared at 24 hours of calcination. The calcined samples of silica B contained only unreacted raw material of MgO as revealed by XRPD and resulted in a single phase of forsterite when the calcination duration was 24 hours. The silica may remain with MgO as an amorphous particle for up to 10 hours of calcination and cannot be detected by XRPD due to the amorphous nature. However, the amount of unreacted raw materials was reduced by means of using the amorphous silica with a spherical shape.

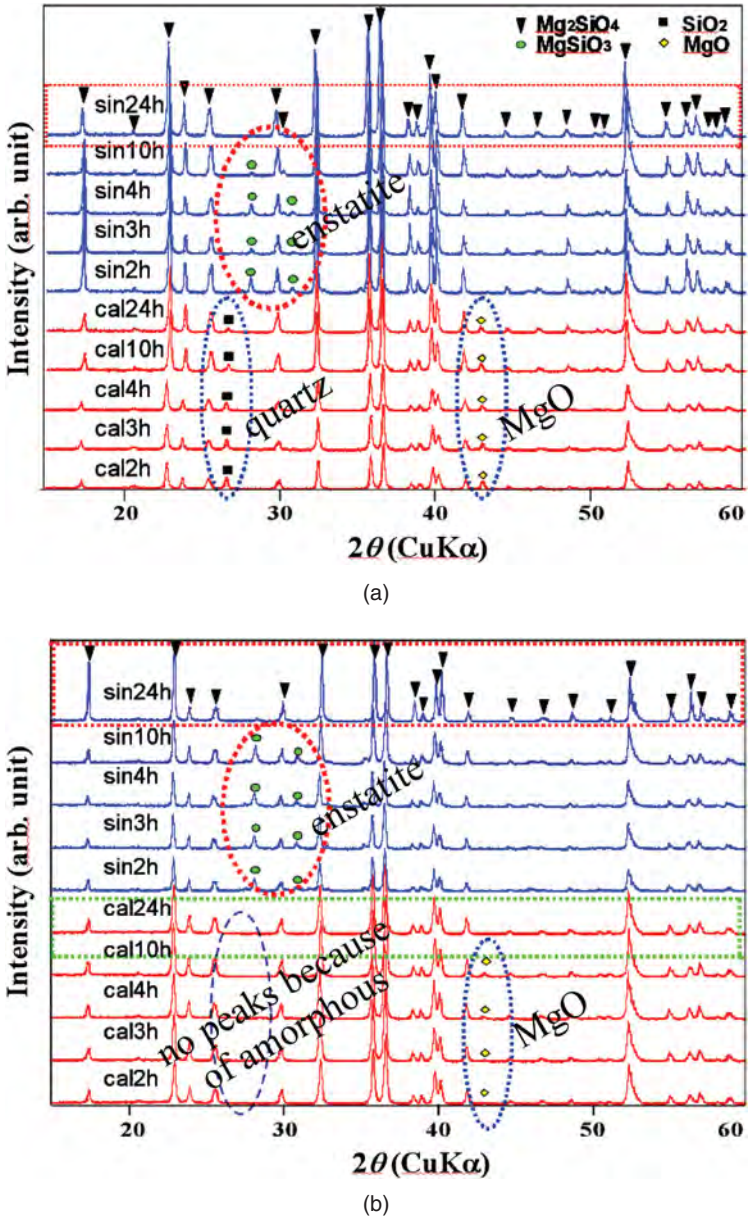

Figure 5.13 *XRPD patterns of powders applied: (a) silica A and (b) silica B. XRPD patterns as shown below half way in (a) and (b) represent the difference in calcined powder at 1175 °C for 2, 3, 4, 10, and 24 hours and are indicated as "cal nh". Above halfway in (a) and (b), 1175 °C, samples, which are sintered at 1400 °C for 2 hours after, are denoted as "sin nh." Source: Ando et al. [21, 22].*

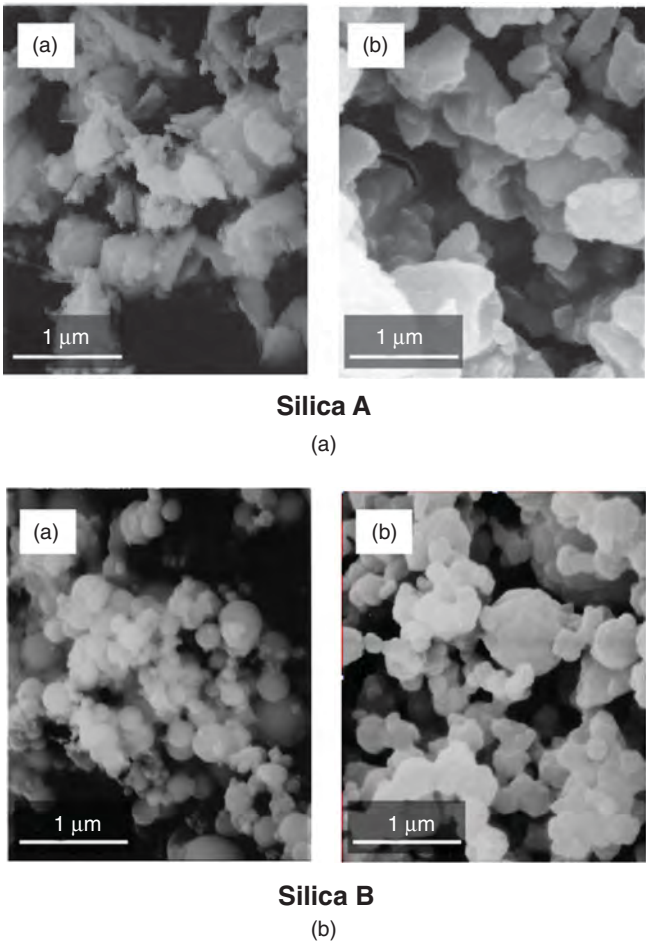

Figure 5.14 *SEM image of silica A and silica B: (a) raw materials and (b) calcined powder. Source: Ando et al. [21, 22].*

Figure 5.14 shows the SEM images of raw SiO_2 (a) and the calcined powder (b) and silica A and B. The shapes of calcined forsterite are the same as the configuration of SiO_2 raw materials, and the size becomes large. This phenomenon is considered as follows: diffusion of Mg ion is more than that of Si ion. This is because Si ion forms SiO_4 tetrahedron due to a half covalent bonding and a half ionic bonding, but Mg ion forms a single ion due to ionic bonding.

To determine the reason for the change in *Qf* as a function of calcination time, the powder calcined at 1175 °C for 2 hours is examined. SEM images in Figure 5.15a and b show the cross-section of the powder grains calcined using silica A and silica B, respectively. Both figures show that the raw silica materials maintain their shape. The shape of the calcined powder using silica A is irregular and that using silica B is spherical. EPMA line analysis is done on Si and Mg of the cross-section of the grains (3.2 μm for silica A and 1.3 μm

for silica B). The concentrations of Si and Mg showed peaks at the core and shell of the grains, respectively. This suggests that forsterite (Mg_2SiO_4) is formed at the shell part of the grains and silica (SiO_2) remains at the core part of the grains. Figure 5.15c shows a small grain (0.86 μm) prepared using silica A calcined at 1175 °C for 2 hours. In this case, the concentrations of Mg and Si are almost the same all over the grains. In the final stage of calcination, forsterite should be completely formed. Figure 5.16 shows the average grain size of the samples sintered at 1400 °C for 2 hours using silica A and silica B as a function of calcination time. Both of the samples synthesized showed maximum grain sizes at calcination times of 4 and 10 hours, respectively. The calcination time at maximum grain sizes just fits those at the lowest *Qf*. The origin of low *Qf* might be concerned with these grain sizes. As shown in scanning electron microscopy (SEM) images in Figure 5.17, the grain size of the sample with the lowest *Qf* is fairly large and the surface morphology shows

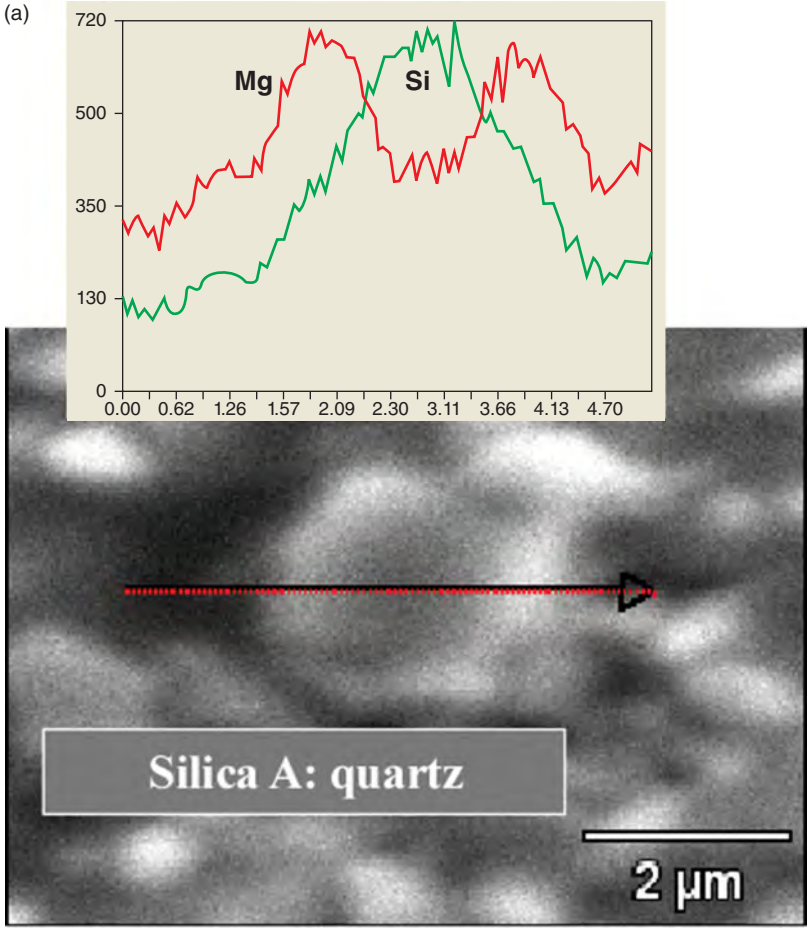

Figure 5.15 *SEM images of the section of grains calcined at 1175 °C for 2 h with EPMA line analysis of Si and Mg: (a) silica A, (b) silica B, and (c) small grains of silica A. Source: Ando et al. [21, 22].*

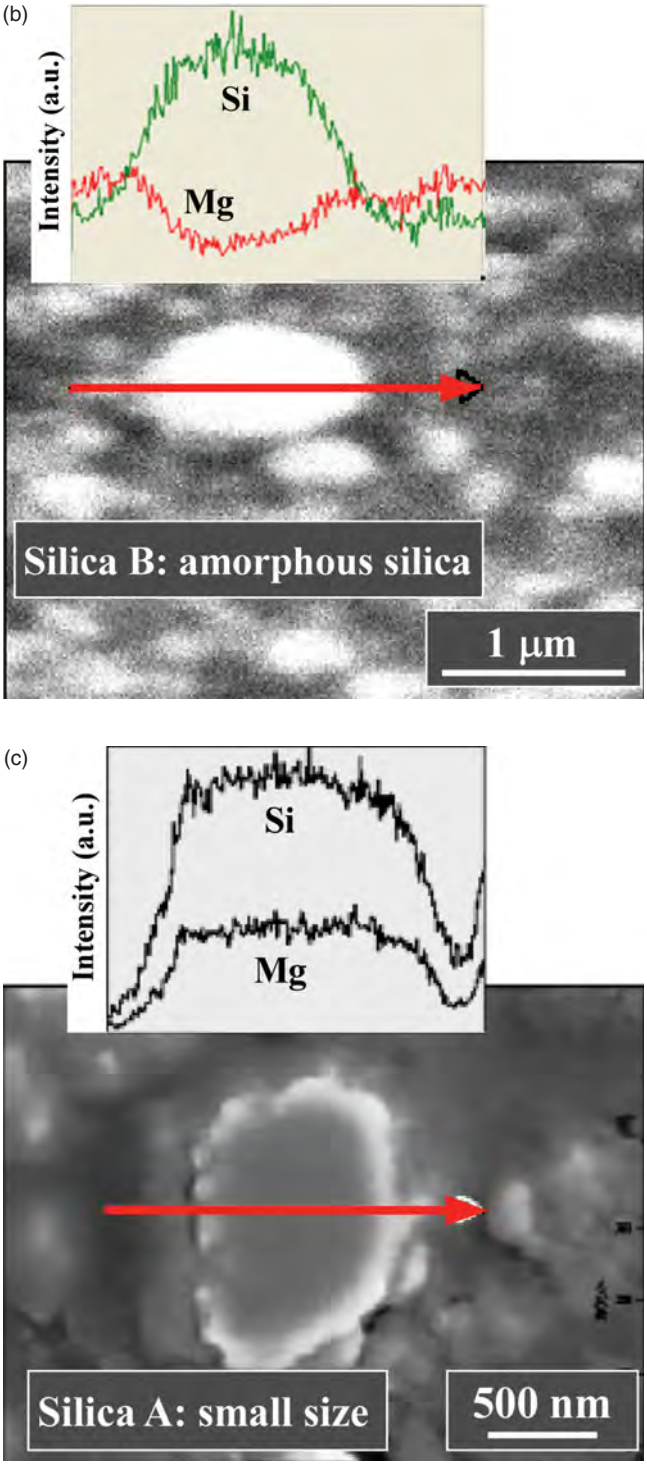

Figure 5.15 *(Continued)*

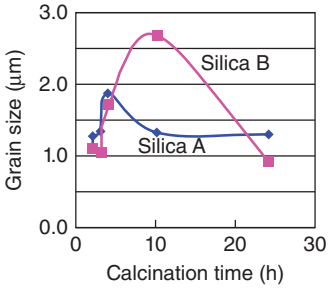

Figure 5.16 *The average grain size of the samples sintered at 1400 °C for 2 hours using silica A and silica B as a function of calcination time. Source: Ando et al. [21, 22].*

a glassy phase. The origin of the glassy phase is residual silica in the core part of the calcined grains. In the SiO_2-rich part in the binary phase diagram of MgO–SiO_2, the eutectic point is about 1546 °C, as shown in Figure 5.18 [40]. Because the sintering temperature is 1400 °C near the eutectic point, the glassy phase must arise from the silica-rich core of the grains including magnesia, as shown in Figure 5.17c and d on silica A and B, respectively. In the early stage of calcination, because the diffusion of Mg is weak, the core part of the grains is occupied mainly by pure silica with a melting point of 1728 °C, which makes the glassy-phase formation difficult. Also, in the final stage of calcination at 24 hours, because all the silica phase reacts with MgO to form forsterite, no glassy phase appears. Thus, the sintered samples on both end-sides of the calcination time show small grains, as shown in Figure 5.17a and e on both silica A and B, and high *Qf* values.

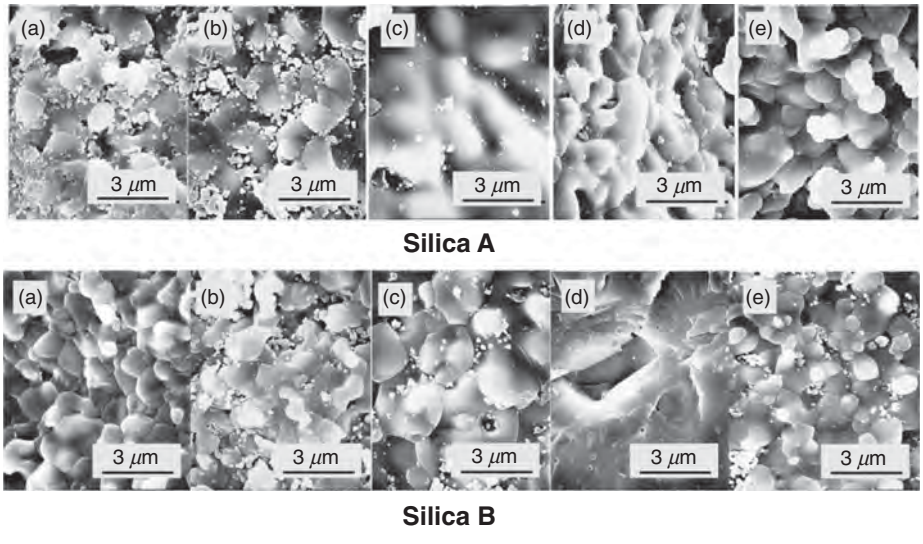

Figure 5.17 *Surface SEM images of specimens prepared by using silica A and silica B sintered at 1400 °C for 2 hours as a function of calcination time and at 1175 °C for (a) 2, (b) 3, (c) 4, (d) 10, and (e) 24 hours. Source: Ando et al. [21, 22].*

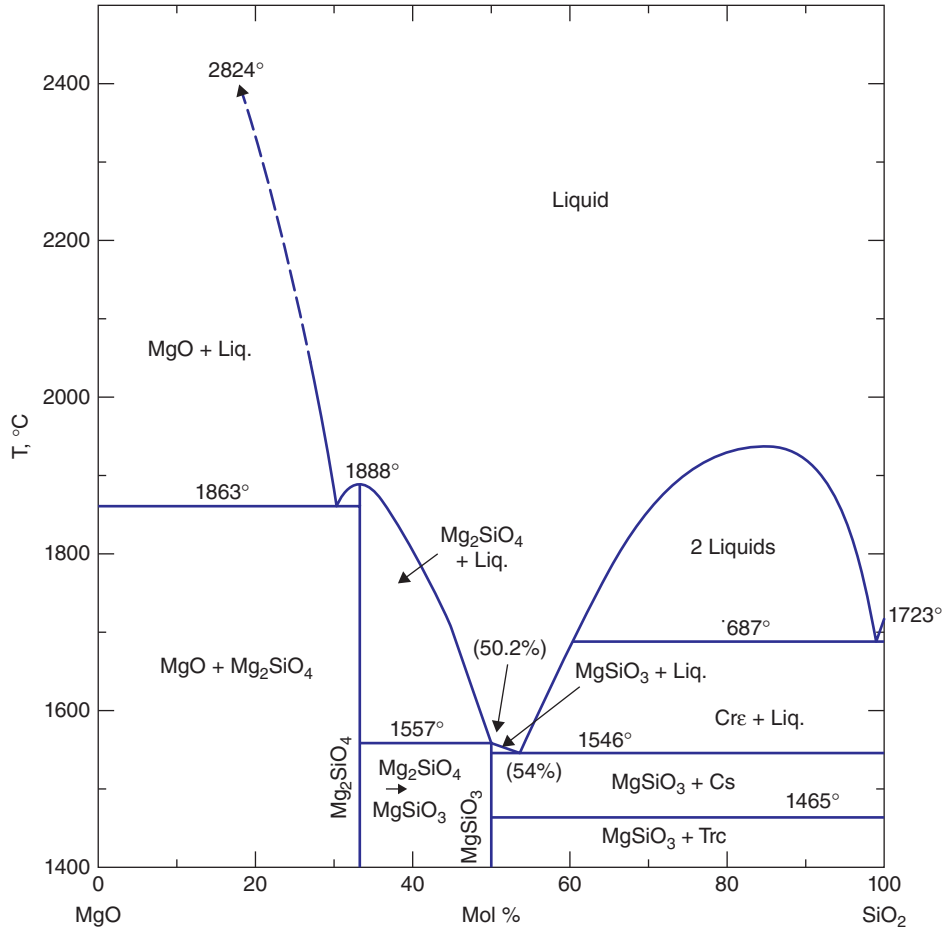

Figure 5.18 *Phase diagram of the MgO—SiO_2 binary system. Source: Adapted from Wu et al. 1993 [40].*

5.4.2 Willemite

5.4.2.1 Synthesis of Willemite with High Q

Guo *et al*. reported willemite (Zn_2SiO_4) ceramics with ultra-high *Qf* of 219 000 GHz [23]. It has a low ε_r of 6.6, which is lower than forsterite. Glass-free willemite ceramics have been sintered at 1340 °C using high-purity ZnO raw materials, as shown in Figure 5.19. The sintering temperature is lower than that of forsterite and is 1400 °C. Ultra-high *Q* of this compound comes from high-purity raw materials and is same as for forsterite described earlier in Section 5.4.1. The ceramics are well sintered with 96 to 98% of theoretical density. Commercial ceramics usually contain a glassy phase. Inclusions and impurities from the glass phase form dipoles with anions (Figure 5.5b) and the *Qf* is degraded by the dipoles turning over under the alternating electromagnetic wave, as shown in Figure 5.4a and b.

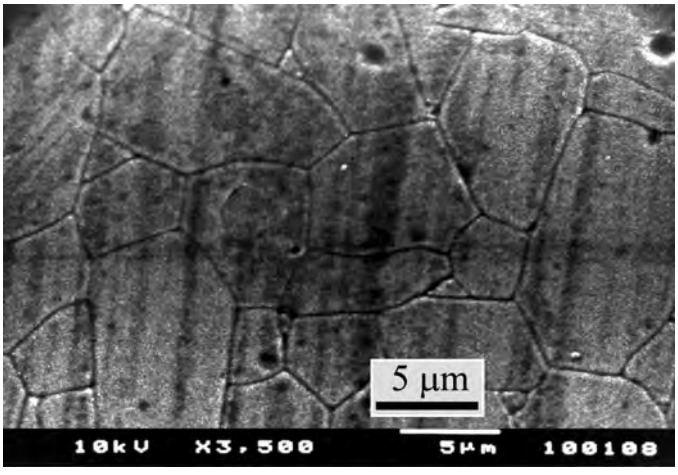

Figure 5.19 *SEM micrograph of willemite ceramic sintered at 1340 °C for 2 h. Source: Adapted from Guo et al. 2006 [23].*

5.4.2.2 *Adjustment of the Temperature Coefficient of Resonant Frequency τ_f of Willemite*

The variation of τ_f of TiO_2-added willemite as a function of TiO_2 (wt%) content is shown in Figure 5.20b. The τ_f changes linearly with TiO_2 content in the range of ±30 ppm/°C, which is the usable region. With 11 wt% of TiO_2, a τ_f value of 1.0 ppm/°C, ε_r value of 9.3, and a *Qf* value of 113 000 GHz are obtained on sintering at 1250 °C. Dong *et al*. [41] also reported willemite ceramics containing 11 wt% of TiO_2 sintered at 1200 °C prepared by the sol–gel process. They also reported excellent microwave dielectric properties: a τ_f value of –1.0 ppm/°C, ε_r value of 9.1, and *Qf* value of 150 000 GHz, and is similar as Guo's data. More exciting, chemical reactions between willemite and rutile could not be

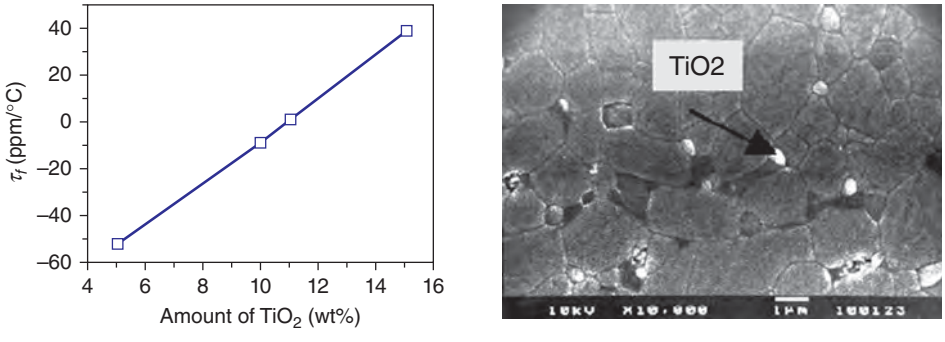

Figure 5.20 *(a) The τ_f of rutile added willemite as a function of amount of TiO_2. (b) SEM photograph of rutile added willemite. These samples were sintered at 1250 °C for 2 h. After Guo et al. [23].*

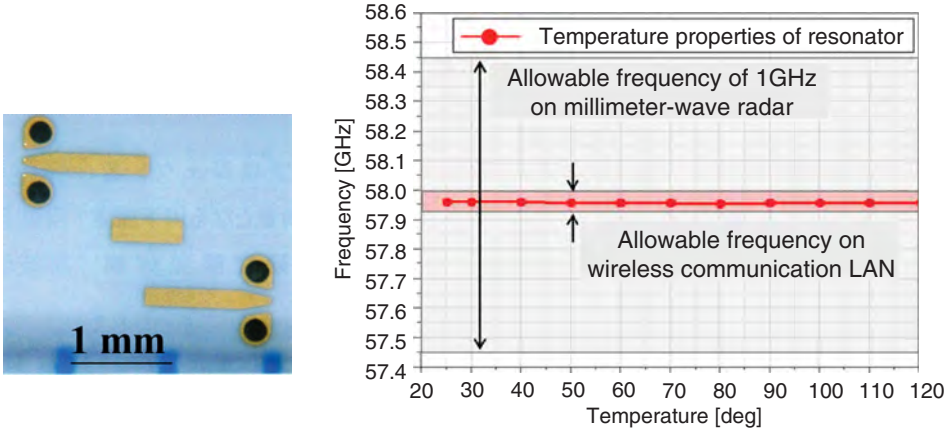

Figure 5.21 *(a) Millimeter-wave dielectric strip resonator with 3 μm thickness electrode on the substrate with 0.2 mm thickness for trial manufacture. (b) Resonant frequency depending on temperature. Source: Adapted from Nakazawa and Shimakata 2011 [8].*

observed at the sintering temperature of 1250 °C. In the case of forsterite, it reacts with TiO_2, producing $MgTi_2O_5$, since the compositions of TiO_2 added to forsterite locate in the $MgTi_2O_5$—Mg_2SiO_4—$MgSiO_3$ subcompositional triangle, as shown in Figure 5.10 [38]. Therefore the τ_f of forsterite is degraded, as shown in Figure 5.9b. On the other hand, in the case of willemite, the τ_f is very stable in a wide sintering temperature range [23]. In a SEM photograph (Figure 5.20b), the rutile particles with white color and submicrometer size are located among grains of willemite. Rutile-added pure willemite substrates for a millimeter-wave resonator with superior τ_f, as shown in Figure 5.20a, are researched and developed in The Supporting Industry Project of Japan by the Ministry of Economy, Trade and Industry of Japan (METI) [7]. On the substrate with 0.2 mm thickness for trial manufacture, a millimeter-wave dielectric strip resonator was fabricated by electrodes with 3 μm thickness, as shown in 5.21a [8]. The $\tau_f = -0.69$ ppm/°C between 20 to 120 °C, as shown in Figure 5.21b, which was under $\Delta f = 0.009$ GHz (difference of frequency) and far lower than allowable frequency of 1 GHz on the millimeter-wave radar for a vehicle. The properties of the substrates are satisfactory as compared to standard substrates for millimeter-wave picture transmission. The substrates show low thermal expansion of 2 to 3 ppm/°C, which is suitable for a millimeter-wave circuit board.

5.4.2.3 Willemite LTCC Substrate

Some examples of LTCC materials appeared in the database by Sebastian *et al.* [42]. Kim *et al*. reported willemite ceramics for LTCC by adding B_2O_3 and V_2O_5 [43, 44]. They added 25.0 mol% B_2O_3 to $Zn_{2-x}SiO_{4-x}$ ceramics (x = 0.2–0.3), resulting with Qf = 70 000 GHz, ε_r = 6.0, and $\tau_f = -21.9$ ppm/°C. Addition of 12 mol% V_2O_5 and sintered

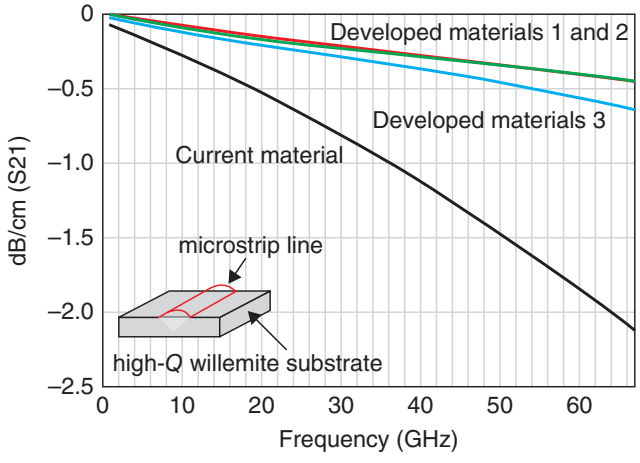

Figure 5.22 *Transmission loss in the microstrip line using high-Q willemite substrate. The loss is 1/9 that in the current substrates [7].*

at 875 °C showed $Qf = 17\,500$ GHz, $\varepsilon_r = 7.3$, and $\tau_f = -28$ ppm/°C. Dou *et al*. reported $0.95Zn_2SiO_4$–$0.05CaTiO_3$ ceramics for LTCC by adding 4 wt% Li_2CO_3–H_3BO_3 sintered at 950 °C, which showed $Qf = 26\,300$ GHz, $\varepsilon_r = 7.1$, and $\tau_f = -4.5$ ppm/°C [45].

The Supporting Industry Project by the METI in Japan has researched on willemite LTCC by using CaB_2O_4 and Li_2O–B_2O_3 low-temperature sintering agents [7]. The project leader Fujimoto [6] compared the transmission loss in the microstrip line fabricated on the willemite substrate with a current material, as shown in Figure 5.22. The transmission loss is 0.5 dB/cm (Ag) at 67 GHz, which is champion data in the world 1/9 losses against current substrate. These data are presented in the following web pages such as: http://www.chubu.meti.go.jp/kikai/sapoin/seika/23fy/23-13.pdf. The products report (outline version: March 2014) "Development for high integration LTCC substrates with high Q and low dielectric constant" by the Japan Fine Ceramics Center (JFCC) was based on the support industries of Japan (2013) by METI, Japan [7].

Low-temperature sintering agents such as Ca–borate (CaB_2O_4), B_2O_3–LiO_2, and $LiBO_2$ for LTCC substrates formed superior low-loss LTCC materials. These agents can sinter the LTCC materials without glass phases. Suvorov *et al.* reported that addition of 10 wt% Ca–borate lowered sintering to 880 °C for 5 hours [46]. In the Supporting Industry Project, 5 wt % Ca–borate was added to willemite for developing LTCC substrates, which showed a low ε_r of 6.7 and high Qf of 25 000 GHz (measurement frequency of 17 GHz). This high Q of 1470 at 17 GHz is superior to $\tan\delta$ of 0.00068 at 1 GHz. In the case of B_2O_3–Li_2O, a low sintering agent, willemite LTCC materials also achieved ε_r lower than 7 and a high Qf around of 35 000 GHz on sintering at 850 to 880 °C. Moreover, the $LiBO_2$ sintering agent with added LTCC substrate was used for fabricating millimeter-wave LTCC slot array antenna on an experimental basis employing gold electrode instead of silver, which has the problem of migration. Ando *et al.* reported silica-boric acid-added willemite LTCC substrates [47].

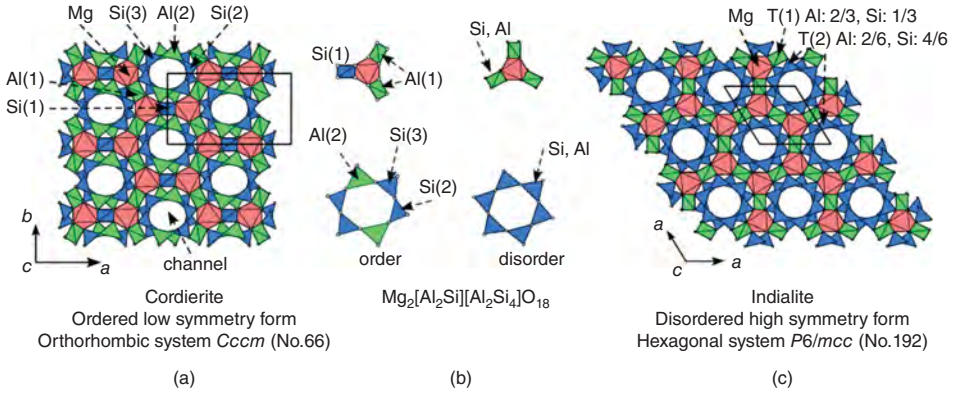

Figure 5.23 *Crystal structure of (a) cordierite and (c) indialite, and (b) ordering/disordering of AlO_4/SiO_4. Source: Adapted from Ohsato et al. 2013 [25].*

5.4.3 Indialite/Cordierite Glass Ceramics

5.4.3.1 Indialite/Cordierite Glass Ceramics with High Q Improved by Ni-Doping

Cordierite ($Mg_2Al_4Si_5O_{18}$) has two polymorphs: cordierite and indialite, as shown in Figure 5.23a and c, respectively. Cordierite is of low symmetry form: an orthorhombic crystal system *Cccm* (No. 66), which has $Si_4Al_2O_{18}$ six-membered tetrahedron rings with ordered SiO_4 and AlO_4 tetrahedra, as shown in Figure 5.23a. On the other hand, indialite is of high symmetry form: hexagonal crystal system *P6/mcc* (No. 192), which has disordered $Si_4Al_2O_{18}$ equilateral hexagonal rings, as shown in Figure 5.23c [48, 49]. Usually in compounds with an order–disorder phase transition, the disordered form is the high-temperature form and the ordered form is the low-temperature form. However, in cordierite, the order–disorder transition point is not clear, because the transition temperature is located near the incongruent melting temperature to mullite and the liquid phase. On the other hand, indialite precipitates as an intermediate phase during the crystallization process from glass to cordierite, which is metastable phase transforming to cordierite at a higher temperature under heating.

Cordierite is characterized by a lower ε_r of 6.19 depending on the silicates, and by near-zero τ_f of –24 ppm/°C [50] as compared to other silicates. Based on these properties, Terada *et al*. carried out extensive research on these microwave dielectrics [51]. They reported a good *Qf* by doping Ni, as shown in Figure 5.24a. The *Qf* was improved from 39 900 to 99 110 GHz by doping Ni of $x = 0.1$ in $(Mg_{1-x}Ni_x)_2Al_4Si_5O_{18}$. The Ni substitution did not change the ε_r value considerably but τ_f was degraded from –24 to –30 ppm/°C. For $x > 0.1$, the properties were affected by the formation of the secondary phase of $NiAl_2O_4$. Terada *et al*. also analyzed the crystal structure of Ni-substituted cordierite by the Rietveld method [52] in order to clarify the origin of the improved *Qf* value. The crystal structure analysis was performed by the Rietveld method using the synchrotron radiation XRPD pattern obtained using the multidetector system (MDS) [53] in the "Photon Factory" of the National Laboratory for High Energy Physics in Tsukuba, Japan. Figure 5.25 shows the crystal structures of Ni-substituted cordierite $(Mg_{1-x}Ni_x)_2Al_4Si_5O_{18}$ with $x = 0$, 0.05, and

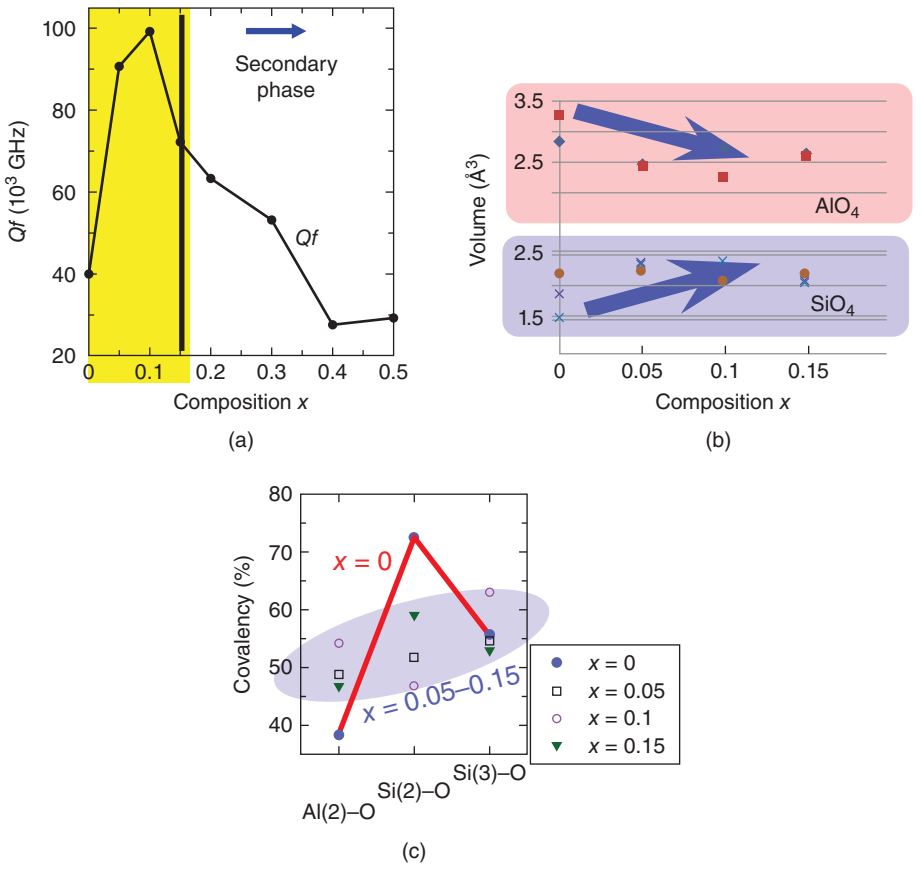

Figure 5.24 *(a) Qf as a function of Ni-doped cordierite, (b) volume of AlO_4 and SiO_4 as a function of Ni-doped cordierite, and (c) covalencies of Si—O and Al—O as a function of composition x. Source: Adapted from Ohsato et al. 2013 [25].*

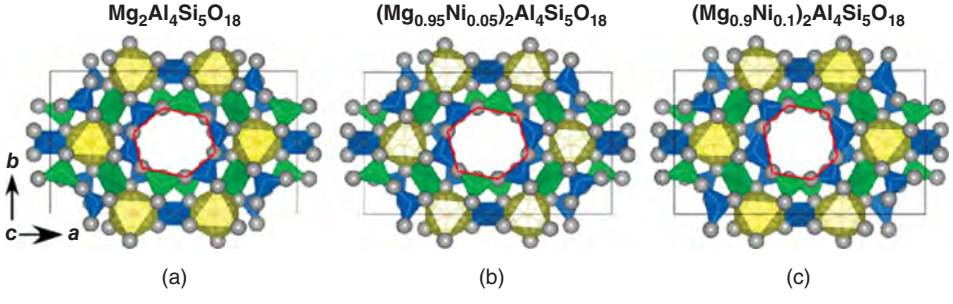

Figure 5.25 *Crystal structure of Ni-doped cordierite $(Mg_{1-x}Ni_x)_2Al_4Si_5O_{18}$, (a) x = 0, (b) 0.05, and (c) 0.1. Source: Adapted from Ohsato et al. 2010 [28].*

0.1. The crystal structure showed a tendency to deform to indialite with high symmetry on the hexagonal ring composed of corner-sharing (Si,Al)O_4 tetrahedra in the *a–b* plane. Ni-substituted cordierite $(Mg_{1-x}Ni_x)_2Al_4Si_5O_{18}$ with composition $x = 0.1$ (see Figure 5.25c) was obviously close to equilateral hexagonal rings compared to $(Mg_{0.95}Ni_{0.05})_2Al_4Si_5O_{18}$ (Figure 5.25b) and $Mg_2Al_4Si_5O_{18}$ (Figure 5.25a). The ratio of disordering between SiO_4 and AlO_4 tetrahedra is shown by volumes and covalencies of SiO_4 and AlO_4 tetrahedra, indicating transformation from cordierite to indialite [28]. The covalency (*fc*) of the cation–oxygen bond was estimated from the following equation [54]:

$$fc = as^M \tag{5.5}$$

where *a* and *M* are empirical constants, which depend on the number of inner-shell electrons of ions reported by Brawn and Wu [55]. Here, $a = 0.54$ v.u. and $M = 1.64$ for the inner-shell electrons number 10. The bond strength *s* is obtained from the following equation:

$$s = (R/R1)^{-N} \tag{5.6}$$

Here, *R* is defined as the bond length. *R*1 and *N* are the empirical parameters that depend on the cation site and the each cation–anion pair, respectively.

Figure 5.24b and c show the calculated volumes and covalency of SiO_4 and AlO_4 octahedra, respectively. On the cordierite $Mg_2Al_4Si_5O_{18}$, as shown in Figure 5.23a, SiO_4 and AlO_4 tetrahedra are located on the hexagonal rings and among the rings by ordering as shown in Figure 5.23b; the volumes of these tetrahedra show different values, as shown in Figure 5.24b. With increasing amounts of Ni substitution in cordierite, those values (Figure 5.24b) become similar and the rings have a tendency to become equilaterally hexagonal, as shown in Figure 5.25c. The covalencies of Si and Al in the (Si, Al)O_4 tetrahedra also become similar, as shown in Figure 5.24 (c). These phenomena mean the orthorhombic crystal system of cordierite (Figure 5.23a) changes to the hexagonal one of indialite (Figure 5.23c). The improvement of *Qf* should be based on the high symmetry instead of ordering by order–disorder transition, as reported in previous papers concerning complex perovskite [32].

5.4.3.2 Indialite Glass Ceramics with High Q

The *Qf* value of indialite derived by Ni-doped cordierite was improved three times from cordierite, as described before in Section 5.4.3.1. Ohsato *et al*. had an idea about synthesis of indialite for high *Q* [25]. Pure indialite could not be synthesized by a solid-state reaction because the order–disorder phase transition is hindered by the incongruent melting to form mullite and liquid. It is well known that indialite is an intermediate phase during the crystallization process from glass with cordierite composition to cordierite. Therefore, fabrication of indialite glass ceramics has been attempted: the glass with cordierite composition was melted at 1550 °C and then kept at 1600 °C for 1 hour. The melted glass was cast into a rod with diameter $\phi = 10$, $l = 30$ mm in a graphite mold. The cast glass rods were annealed at 760 °C under the glass transition point of 778 °C in order to avoid fracture by internal strain, as shown in Figure 5.26a and b. The glass rod with 10 mm diameter was cut to form a resonator with a height of 6 mm (Figure 5.26c).

The glass pellets were then crystallized at temperatures in the range of 1200 to 1470 °C for 10 and 20 hours. The crystallized pellets have two problems: deformation (Figure 5.27a)

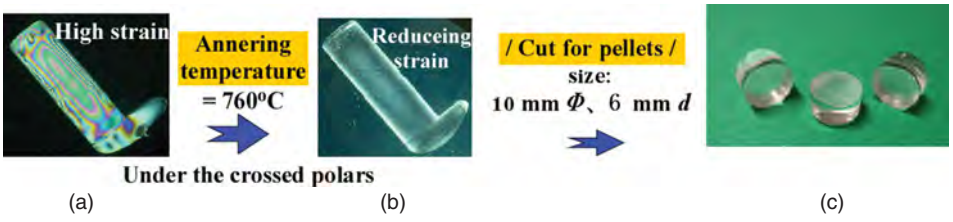

Figure 5.26 *(a) Just-casted glass rod with internal strain under the crossed polars, (b) annealed glass without strain free, and (c) glass pellets cut for resonator. Source: Adapted from Ohsato et al. 2013 [25].*

by formation of a glass phase and cracking (Figure 5.27a) by crystal growth from the surface (Figure 5.27b) [25]. Figure 27b shows photographs by a polarizing microscope of the thin section of crystallized samples. The needle-like crystals grown from the surface have an orientation with *c*-axis elongation. As the thermal expansions of *c*-direction and perpendicular to the *c*-axis are of opposite signs, as shown in Figure 5.27c, the cracking has appeared as shown in Figure 5.27a. The microwave dielectric properties of the sample with cracking had a wide scattering range of the data [25].

Microwave dielectric properties of indialite/cordierite glass ceramics showed extremely high *Qf* values of more than 200 000 GHz, as shown in Figure 5.28b [24], which is much

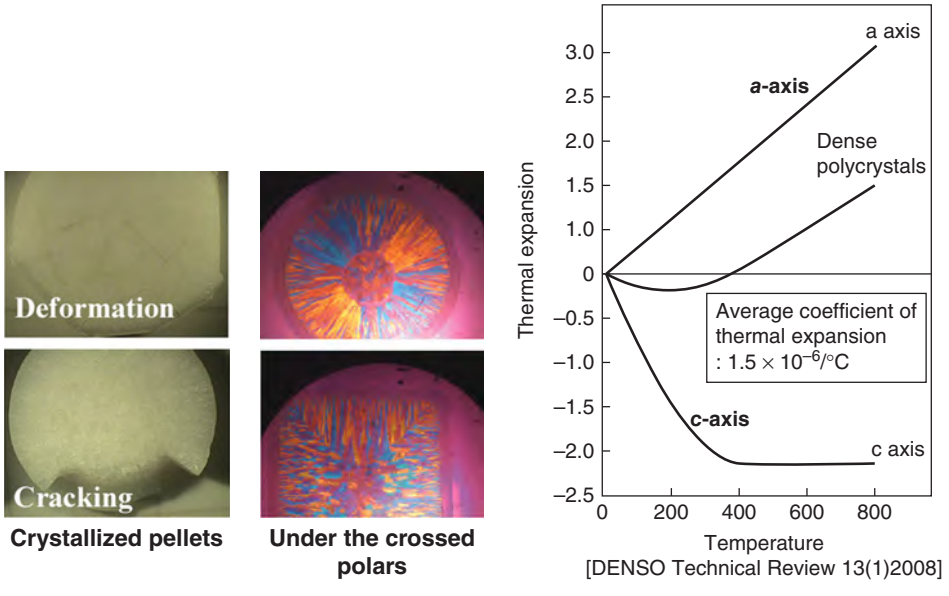

Figure 5.27 *(a) Deformation and cracking of crystallized pellets, (b) anisotropic crystal growth of the pellets crystallized from the surface of the glass pellets under the crossed polars, and (c) thermal expansion of crystallographic axes on cordierite. Source: Adapted from Ohsato et al. 2013 [25].*

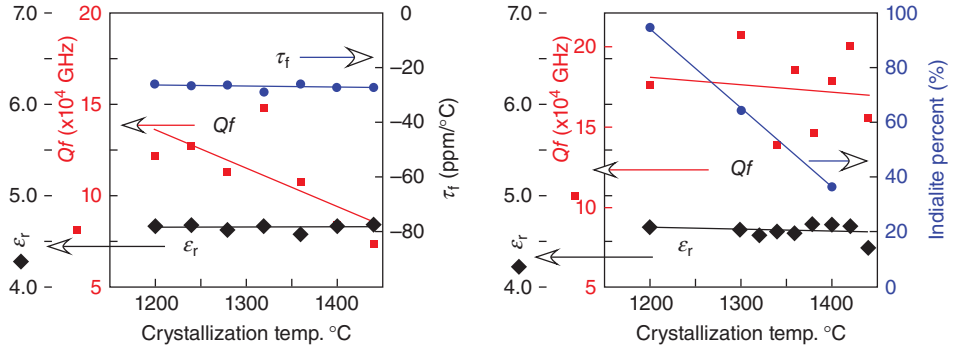

Figure 5.28 *Microwave dielectric properties of indialite/cordierite glass ceramics crystallized for (a) 10 and (b) 20 hours, and indialite percentage (b) as a function of the crystallization temperature. Source: Adapted from Ohsato et al. 2013 [25].*

better than the highest *Qf* value of 90 000 GHz obtained by doping Ni using the conventional solid-state reaction as described before (Figure 5.24a), which is a suitable level for millimeter-wave dielectrics. However, the measured *Qf* values in these samples showed a wide scattering range, as described above. The *Qf* values decrease as a function of crystallization temperature. From the relationship between the *Qf* and the phase proportions, as shown in Figure 5.28, it is clear that the indialite glass ceramics exhibit a higher quality factor than the cordierite ones. The dielectric constant ε_r is lowest at 4.7 among the silicates and the τ_f was –27 ppm/°C, as shown in Figure 5.28a. The amount of indialite/cordierite was analyzed by the Rietveld method, which is calculated using two phases such as indialite and cordierite. Here, the amount of residual % corresponds to that of cordierite. At 1200 °C, about 95% of the precipitated phase is indialite and the amount of indialite decreases and that of cordierite increases along with increasing temperature. Therefore, from these figures, indialite shows a higher *Qf* than cordierite. This τ_f value of –27 ppm/°C is better than that of other substrates having a low dielectric constant of approximately –60 ppm/°C as shown in Table 5.2 [24].

The amount of indialite could be estimated from ordering of Al/SiO_4 tetrahedra, which show a difference of volume and covalency from AlO_4 and SiO_4 tetrahedra as described before in the case of Ni-doped cordierite [28]. The volume and covalency can be calculated based on the atomic coordinates obtained using indialite and cordierite mixed models by the Rietveld method. Figure 5.29a and b show the volume and covalency of Si/AlO_4 tetrahedra for indialite and cordierite phases, respectively, formed at 1200, 1300, and 1400 °C [25]. There are two sites of tetrahedra in indialite: one is *T*(1) located among the rings and another is *T*(2) in the hexagonal ring, as shown in Figure 5.23c. There are also five sites of tetrahedra in cordierite: Al(1) and Si(1) locate among the hexagonal rings, while Al(2), Si(2), and Si(3) locate inside the ring, as shown in Figure 5.23b. All the volumes of the tetrahedra at 1200 °C converged to a range of 2.2–2.5Å^3, as shown in Figure 5.29a, which indicates disordering of Si and Al ions. *T*(1), Al(1), and Al(2) increase to around 2.6 Å^3 at 1400 °C. On the other hand, *T*(2), Si(1), Si(2), and Si(3) decrease to around 2.2 Å^3. Here, ionic radii of Al^{3+} and Si^{4+} with coordination number (CN) 4 are 0.39 and 0.26 Å, respectively. Therefore, the changes in the tetrahedral volumes depend on the ratio Al and Si in these sites. In the case

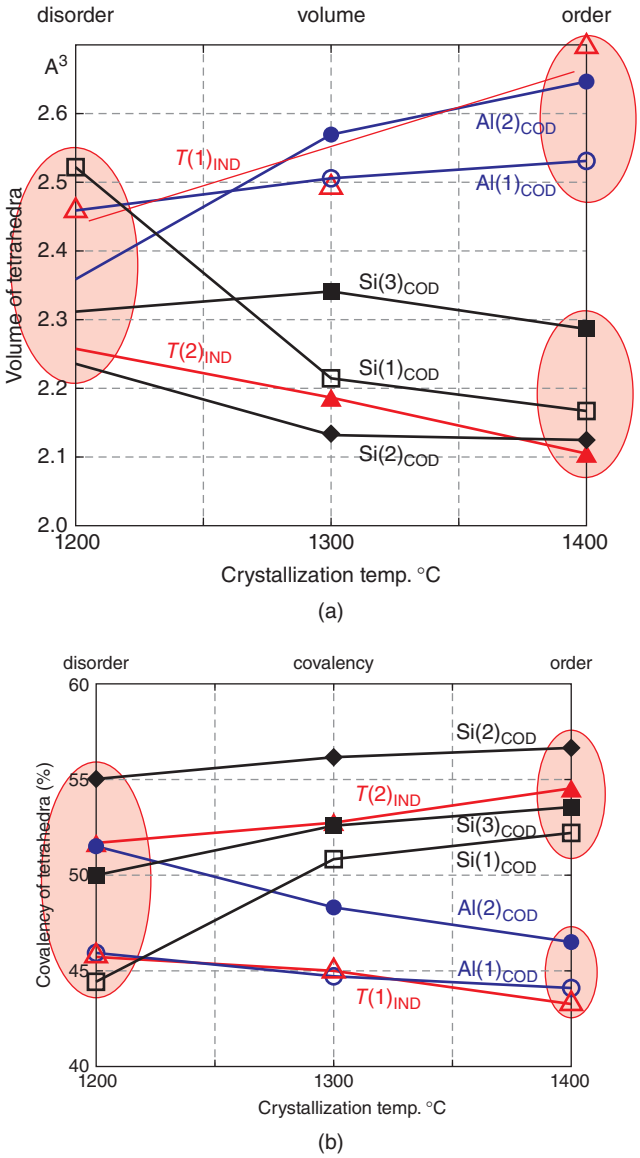

Figure 5.29 *Estimating the ordering ratios of Si and Al in tetrahedra by (a) volumes and (b) covalencies of Si/AlO_4 tetrahedra. Source: Adapted from Ohsato et al. 2013 [25].*

of covalencies, *T*(2), Si(1), Si(2), and Si(3) increase, while *T*(1), Al(1), and Al(2) decrease as a function of crystallization temperature. Usually covalency of the SiO_4 is larger than that of the AlO_4 tetrahedron. Hence, the increase of covalencies of *T*(2), Si(1), Si(2), and Si(3) sites at 1400 °C indicate that Si ions dominantly occupy these sites. On the other hand, the decrease of the covalencies of *T*(1), Al(1), and Al(2) should indicate that Al ions occupy these sites.

(a)

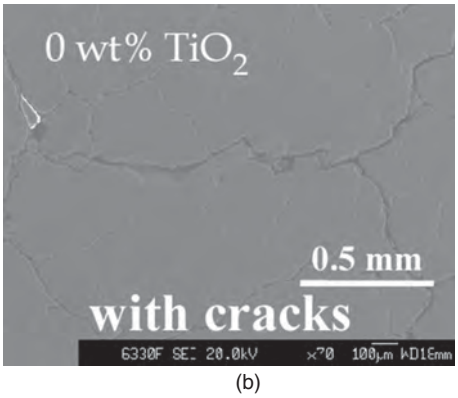

(b)

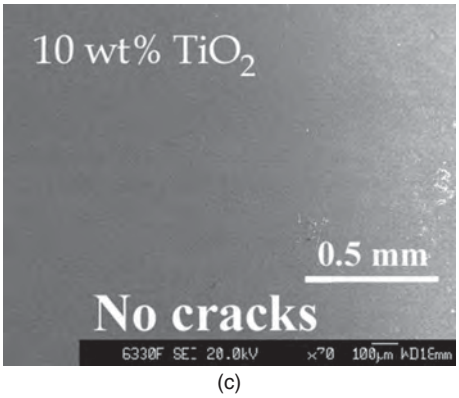

(c)

Figure 5.30 *(a) Optical and (b) and (c) SEM photographs of indialite/cordierite glass ceramics crystallized at 1200 °C for 10 hours; (a) and (c) with 10 wt% TiO_2 show no cracks and no deformations, but (b) without TiO_2 shows cracks. Source: Adapted from Kagomiya and Ohsato 2014 [56].*

5.4.3.3 Control of Deformation, Cracking, and τ_f by Adding Rutile

In order to avoid the deformation and cracking of indialite/cordierite glass ceramics stated above, volume crystallization was performed by adding a nucleating agent such as rutile [56]. Figure 5.30a shows photographs of 10 wt% rutile added to glass ceramics crystallized at 1200 °C for 10 hours, indicating the absence of deformation and cracks. The SEM figure of the glass ceramics also did not show cracking (Figure 5.30b). Figure 5.31 shows microwave dielectric properties of the glass ceramics with rutile of 0, 10, and 20 wt% crystallized at 1200 °C for 10 hours. The τ_f was adjusted to 0 ppm/°C by adding 12 wt% of rutile, which has a high τ_f of 450 ppm/°C. The Qf value was found to decrease to 100 000 GHz and ε_r increased to 5.8 by rutile addition.

5.4.4 Other Silicates

5.4.4.1 Wollastonite

Pseudowollastonite (α-$CaSiO_3$) of high temperature form is also characterized by a lower ε_r of 7.0 and by a near-zero τ_f of –21 ppm/°C, which are good properties for

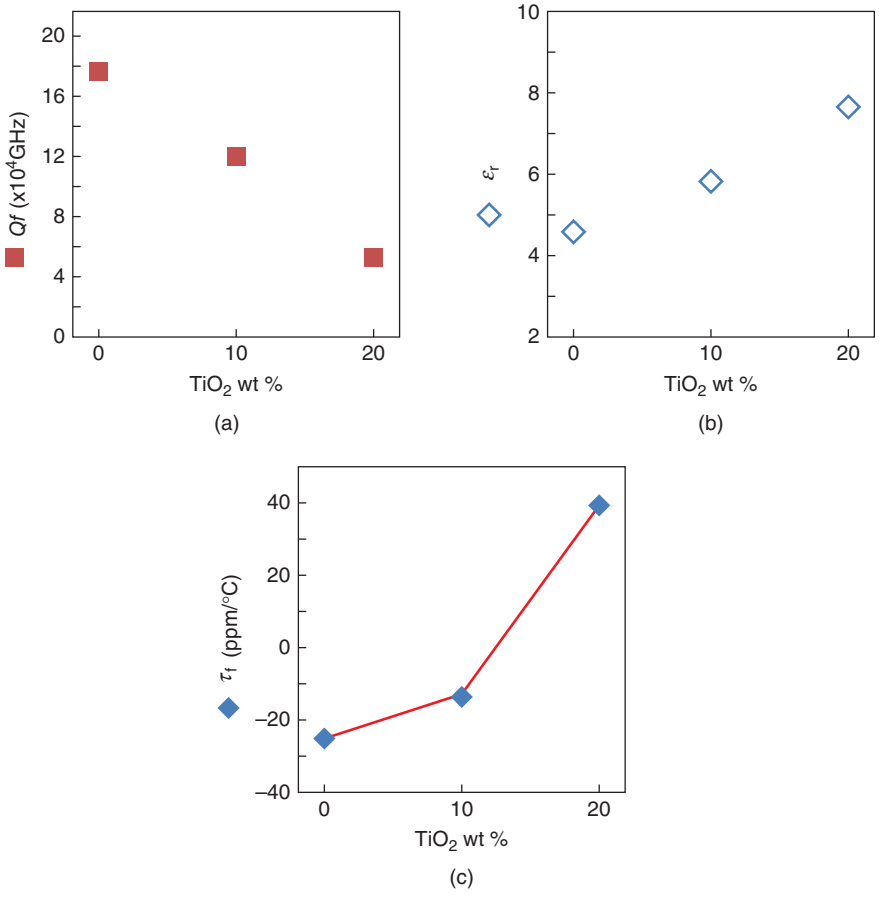

Figure 5.31 *Microwave dielectric properties of indialite/cordierite glass ceramics with rutile 0, 10, 20 wt% crystallized at 1200 °C for 10 hours. Source: Adapted from Kagomiya and Ohsato 2014 [56].*

millimeter-wave dielectrics. The *Qf* value of 36 000 GHz was improved to 67 000 GHz at $x = 0.8$ on the $Ca_{1-x}Sr_xSiO_3$ substituted Sr for Ca [26].

Wollastonite $CaSiO_3$ possesses two polymorphs: one is a low-temperature form composed of a chain structure of SiO_4 tetrahedra and the second one is a high-temperature form (pseudowollastonite α-$CaSiO_3$) with three-membered ternary rings of SiO_4 tetrahedra, as shown in Figure 5.32. Among the silicates, cordierite composed of six-membered SiO_4 hexagonal rings shows τ_f close to zero, suggesting that the SiO_4 ring framework contributes to a lower absolute value of τ_f. As silicates with a ring framework are expected to be a near-zero τ_f, detailed investigation was done on the microwave dielectric properties of α-$CaSiO_3$. In addition, $SrSiO_3$ substituted Sr for Ca was focused, which is composed of a three-membered ternary ring of SiO_4 tetrahedra. Both α-$CaSiO_3$ and $SrSiO_3$ belong to the same monoclinic space group $C2/c$. However, the detailed structures are different: the former is composed of a four-layered structure (Figure 5.32a) [57] and the latter a six-layered structure (Figure 5.32b) [58]. α-$CaSiO_3$ and $SrSiO_3$ are end-members of a eutectic binary

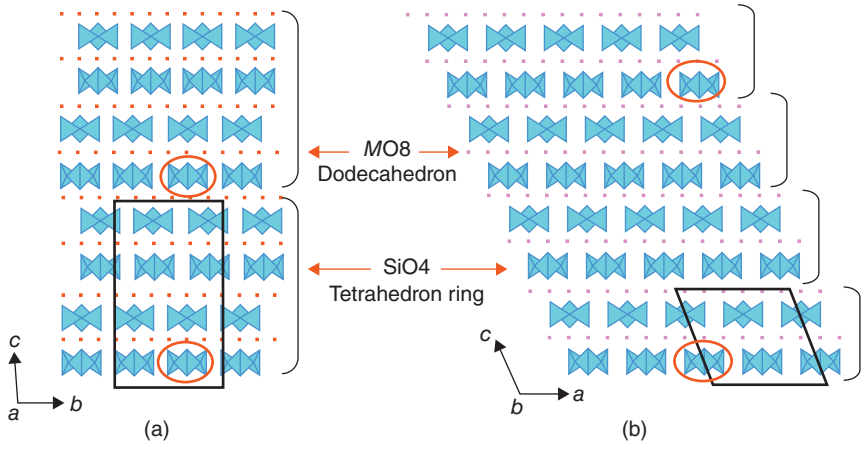

Figure 5.32 *Crystal structure of (a) α-$CaSiO_3$ and (b) $SrSiO_3$ solid solutions. Source: Adapted from Kagomiya et al. 2009 [26].*

phase diagram (ACerS-NIST Phase Equilibria Diagrams No. 6680) [59]. The end-members form a wide range of solid solutions called $CaSiO_3$ solid solutions (s.s.) and $SrSiO_3$ s.s. from $x = 0$ to 0.4 and 0.6 to 1.0, respectively.

The dielectric properties of $(Ca_{1-x}Sr_x)SiO_3$ are shown in Figure 5.33 [26]. Although the *Qf* value of α-$CaSiO_3$ solid solutions was decreased with composition x, that of $SrSiO_3$ solid solutions was increased to 66 700 GHz at $x = 0.8$ on the $(Ca_{1-x}Sr_x)SiO_3$, as described above. Although the relative density increased to 95%, ε_r shows the lowest value at $x = 0.8$. The reason for the lowest ε_r and highest *Qf* is based on the covalence of the SiO_4 tetrahedra. The average covalencies of Si(1)–O and Si(2)–O at $x = 0.8$ are 55.3 and 53.1, respectively. On the other hand, those at $x = 1.0$ are 54.9 and 52.1. As the covalencies of SiO_4 tetrahedra at $x = 0.8$ are larger than those at $x = 1.0$, the ε_r values are low. The *Qf* values are high based on the crystal structure stabilized by the high covalencies of the SiO_4 tetrahedra.

5.4.4.2 *Diopside*

The ε_r of diopside ($CaMgSi_2O_6$) is low at 7.6, which is suitable for millimeter-wave dielectric applications. By controlled synthesis the *Qf* of diopside can be improved from 59 700 to 121 380 GHz, which will be described later [27]. Figure 5.34 shows microwave dielectric properties of diopside ceramics as a function of calcination temperature. When the calcination temperature is 1200 °C, the best *Qf* value of 121 380 GHz was obtained. This composition has the best sintering condition with the highest relative density, as shown in Figure 5.35c. The dielectric constants ε_r were increased from 6.9 to 7.6 with an increase in calcination temperatures up to 1200 °C and then decreased to 7.4 at 1250 °C. These ε_r values are synchronized with *Qf* values and also relative densities. Although ε_r are usually synchronized with relative density, it is very interesting for ε_r to be accompanied by *Qf*. The reason for this phenomenon is expected to be clarified in the future. The temperature coefficient of the resonant frequency τ_f was about –60 ppm/°C, which is similar to the negative large values for most of the resonators with a low ε_r, such as forsterite, willemite, alumina, etc.

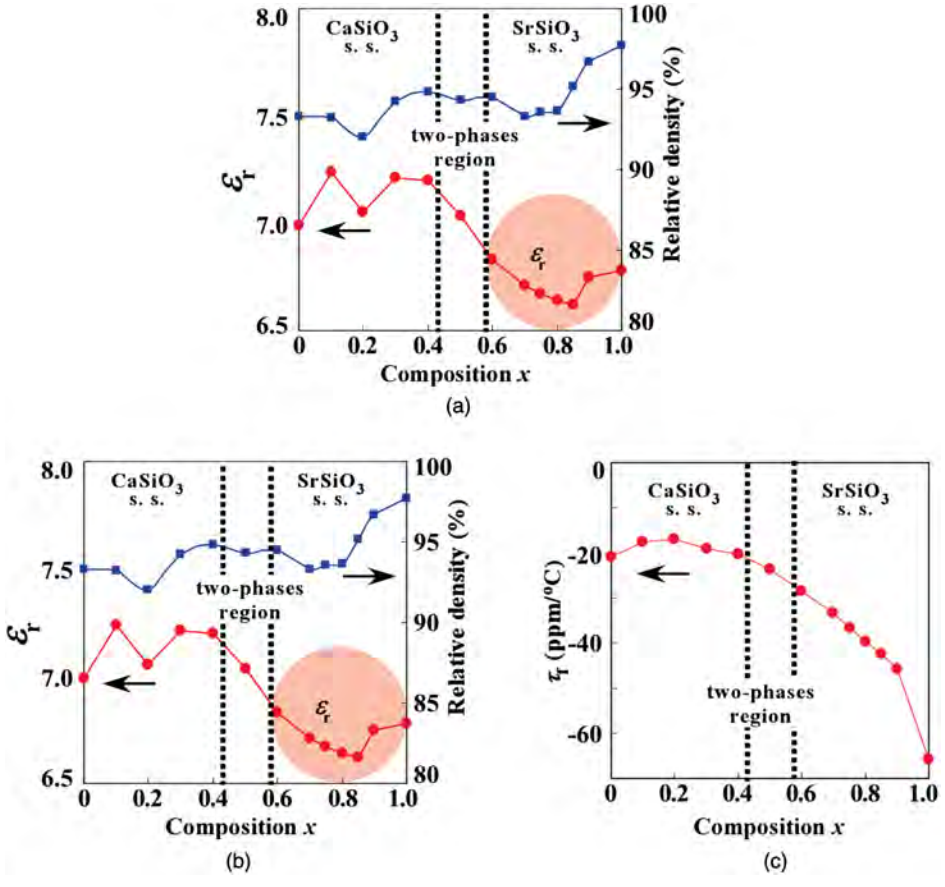

Figure 5.33 *Relative density and microwave dielectric properties, ε_r, Qf, and τ_f, of $(Ca_{1-x}Sr_x)SiO_3$ solid solutions as functions of composition x. Source: Adapted from Kagomiya et al. 2009 [26].*

The *Qf* values are affected by the fine calcined isolated grain powders without necking. The powder was prepared by calcining at 1200 °C for 2 hours, by which time the highest *Qf* diopside ceramics with a high relative density of 96.7% were formed on sintering at 1300 °C for 2 hours, as shown in Figure 5.35c. The high density was brought about by a high bulk green density of 1.8 g/cm^3 (Figure 5.35b) using fine calcined isolated grain powder sintered without necking at 1200 °C, as shown in Figure 5.36c. The necking resulting from sintering at 1250 °C was observed in the marked circle shown in Figure 5.36d, which might be formed by the eutectic melts (1357 °C) in the diopside–akermanite–mullite subcompositional triangle. The starting composition of diopside should be shifted to a composition with less SiO_2 in the subcompositional triangle owing to the formation of a core–shell structure on the quartz grain, as described earlier in Section 5.4.1.3 and now shown in Figure 5.37 [21, 22].

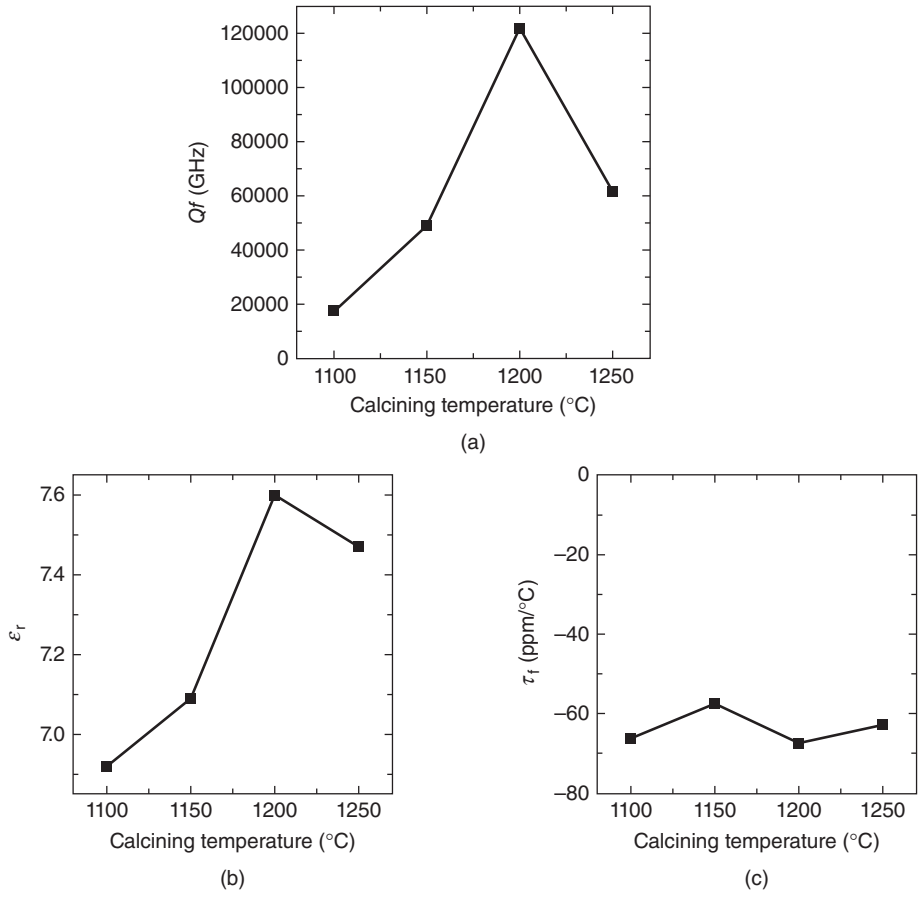

Figure 5.34 *(a) Qf, (b) ε_r and (c) τ_f of $CaMgSi_2O_6$ ceramics sintered at 1300 °C, as a function of calcining temperature. Source: Adapted from Ohsato et al. 2012 [27].*

5.4.5 Substituted Ge for Si

5.4.5.1 Ionicity and Covalency

The feature of the SiO_4 tetrahedron is that it brings low ε_r for important properties of millimeter-wave dielectrics, as described in Section 5.2.2. In this section, it is presented that the GeO_4 tetrahedron substituted for Si also brings low ε_r. Ionicity and covalence of the SiO_4 tetrahedron are 44% and 56%, respectively, which are derived based on the electronegativity difference between Si and O as following procedure and are discussed in a paper by Pauling [60]. Figure 5.38b shows the amount of ionic character as a function of the difference of electronegativity $|x_A - x_B|$ between the A–B bond presented based on the following equation by Pauling [61]:

$$\text{Amount of ionic character } p = 1 - e^{-c(x_A - x_B)} \tag{5.7}$$

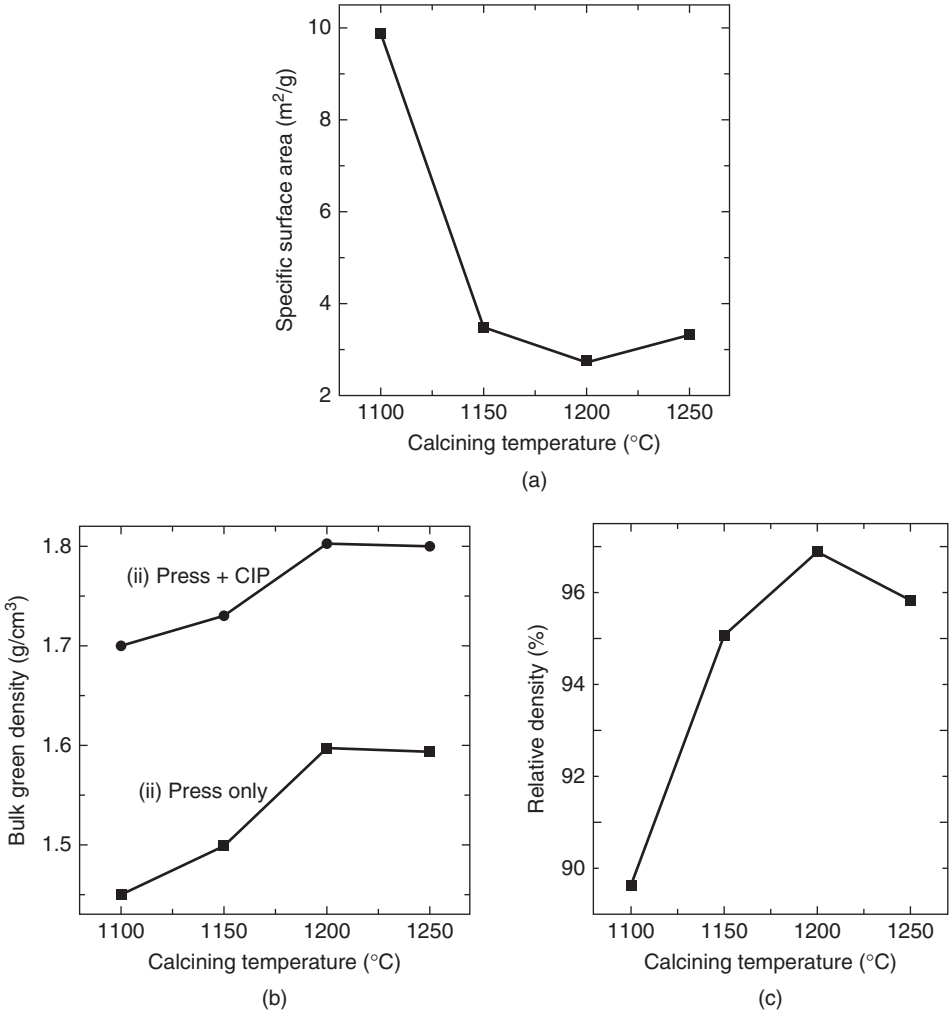

Figure 5.35 *(a) Specific surface area, (b) bulk green density, and (c) relative density of sintering temperature at 1300 °C for 2 h. Source: Adapted from Ohsato et al. 2012 [27].*

in which c has the value 1/4. According to this curve [62], the bonds in the case of Si—O with $|x_A - x_B| = 1.7$ have a 50% ionic character and a 50% covalent character. Equation (5.7) was modified based on the dipole moment of HF measured by Hannay and Smith [63] as follows:

$$p = 16|x_A - x_B| + 3.5|x_A - x_B|^2 \tag{5.8}$$

According to this equation, p of Si—O with $|x_A - x_B| = 1.7$ was 37.3% smaller than the value of Poling, and $p = 50\%$ was obtained by $|x_A - x_B| = 2.1$. An electronegativity difference of about 2.1 corresponds to a bond that is 50% ionic. Bonds with a larger

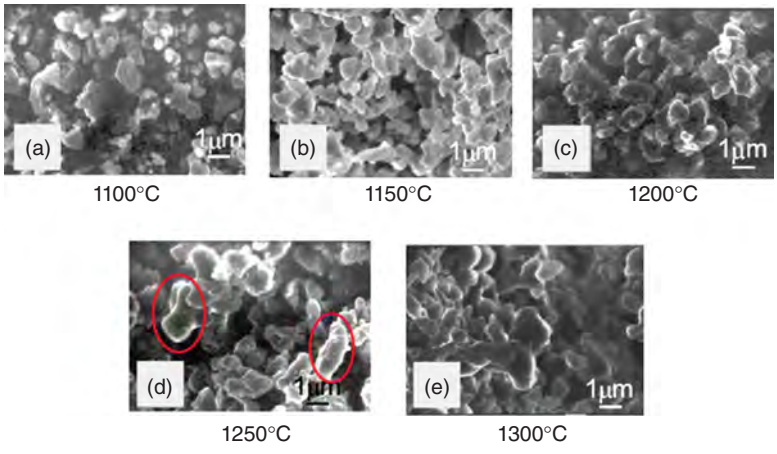

Figure 5.36 *SEM figures of diopside powders calcined at 1100–1300 °C for 2 h. Source: Ohsato et al. 2012 [27].*

electronegativity difference are therefore primarily ionic; those with a smaller difference are primarily covalent.

If atomic coordinates are obtained by crystal structure analysis, covalency f_c can be calculated more quantitatively using bond strength s, which is presented in Section 5.4.3.2). In the case of cordierite presented in Section 5.4.4, covalency values of Si—O bonds are located around 50.3 to 80.6% averaged to 63.22% and those of Al—O around 34.5 to 47.5% averaged to 39.3%. When Ni 0.1 mol% was doped to cordierite, covalency values of Si—O bonds were located around 37.13 to 83.9% averaged to 54.8%,

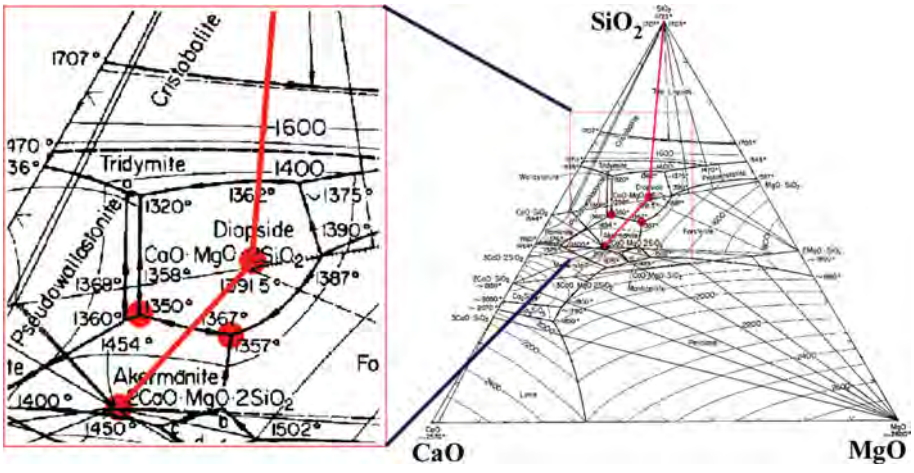

Figure 5.37 *Phase diagram of CaO—MgO—SiO_2 ternary system. A part around the diopside and akermanite is magnified including triple points at 1350 and 1357 °C. Source: Adapted from Ohsato et al. 2012 [27].*

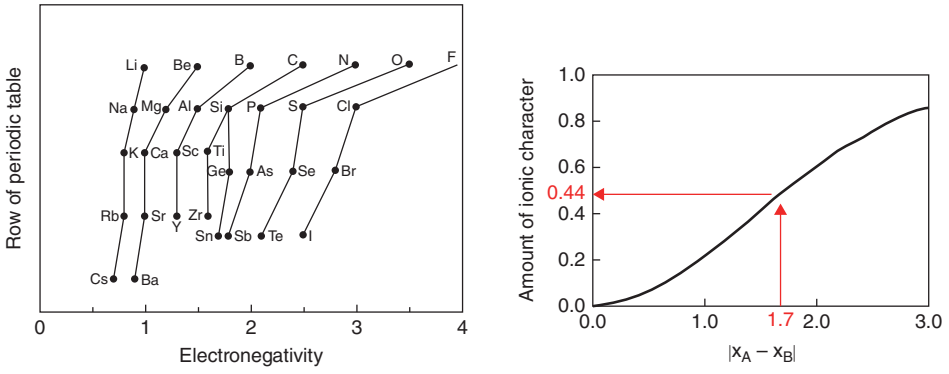

Figure 5.38 *(a) The electronegativity scale of the elements, showing the relation to the periodic table. The electronegativities are plotted against the horizontal scale, and different columns of the periodic table are separated vertically. (b) Curve relating an amount of ionic character of a bond A—B to the difference in electronegativity $x_A - x_B$ of the atoms [61, 62].*

and those of Al—O around 36.5 to 50.4% averaged to 49.2% [28, 64]. Based on these data, it was revealed that by reducing the differences between Si—O and Al—O covalency values, disordering of Si/AlO_4 tetrahedra by phase transition from cordierite to indialite had been clarified. In the case of a phase change by the crystallization temperature, as stated in Section 5.4.3.2, the covalency values also clarified the change [25]. In another case of Sr–wollastonite $SrSiO_3$ and $(Ca_{0.2}Sr_{0.8})SiO_3$ presented in Section 5.4.4.1, covalency values of Si—O bonds around 46.75 to 69.27% average to 53.5% and around 47.18 to 69.45% average to 54.2% were obtained, respectively [26]. The reason for high *Qf* on the $(Ca_{0.2}Sr_{0.8})SiO_3$ were discussed.

5.4.5.2 Ge–Forsterite and Ge–Willemite

Some examples with GeO_4 tetrahedra for LTCC materials appeared in the database by Sebastian [42] and are Zn_2GeO_4 (Ge–willemite) ceramics [65] with the same structure of willemite (Zn_2SiO_4) and with the same space group of trigonal $R\bar{3}$(No. 148). The properties are ε_r of 6.87 similar to 6.6 of willemite depending of same electronegativity value of 1.8, *Qf* of 102 700 GHz, and τ_f of –32.4 ppm/°C. The B_2O_3-added Mg_2GeO_4 (Ge–forsterite) [66] has the same structure with forsterite as the space group of orthorhombic *Pnma* (No.62), with ε_r of 6.8 similar to forsterite, *Qf* of 95 000 GHz, and τ_f of –28.7 ppm/°C.

5.4.5.3 Feldspar

The feldspars have a general formula MT_4O_8. Here T = Si and Al, located in the tetrahedron site, and $M = Na^+$, K^+, Rb^+, Ca^{2+}, Sr^{2+}, or Ba^{2+}. Also, T sites could be occupied by Ge^{4+} and Ga^{3+} instead of Si^{4+} and Al^{3+}, respectively. Most natural feldspars lie in the $KAlSi_3O_8$ (Orthoclase: Or)–$NaAlSi_3O_8$ (Albite: Ab)–$CaAl_2Si_2O_8$–(Anorthite: An), triangle, as shown in Figure 5.39 [67]. TO_2 makes the framework similar to various SiO_2 crystal structures, and substitution of Al^{3+} for Si^{4+} introduces large cations Na^+ (or K^+ or Ca^{2+})

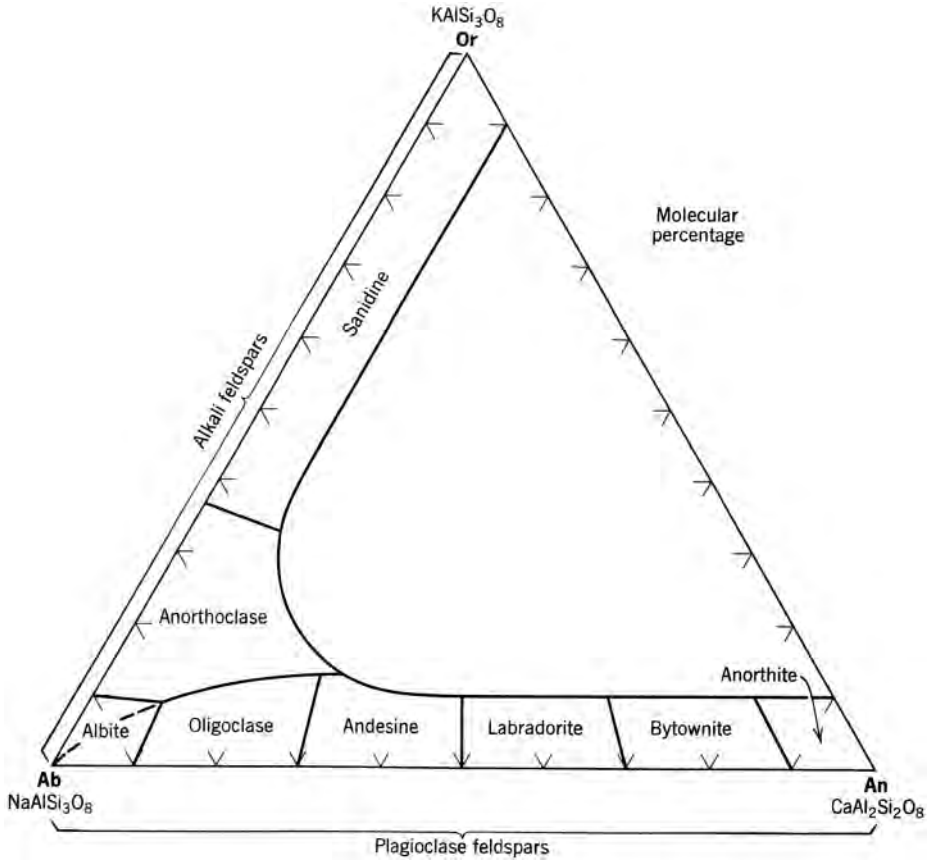

Figure 5.39 *The solid solutions in alkali and plagioclase feldspars at high temperature. Source: Adapted from Hurlbut 1971 [67].*

to maintain electrostatic charge valances. Anorthite feldspar was presented for a new glass of LTCC (LFC) at the International Society for Hybrid Microelectronics (ISHM) 1985 [68] and 1986 [69] by Nishigaki *et al*., who got the Best Paper Awards in 1985 and 1986 at the Conferences. The anorthite feldspar has good properties such as a low dielectric constant of 7.0, low thermal expansion (CTE) of 4.5×10^{-6}/ °C and high temperature resistance at 1300 °C. The composition of the LFC (low temperature fireable ceramics) is the G1 point, adding the Al_2O_3 filler as shown in Figure 5.40 [70], which meets the eutectic point of 1170 °C due to dissolution of Al_2O_3 and melts under 900 °C by the effect of adding B_2O_3 at 10 wt%. This LFC technology was handed to Bosch and bone fruit to μ-Hybrid (LTCC-ECU) in 1995 [70]. Recently, Krzmanc *et al*. [71] presented microwave dielectric characterization of plagioclase feldspars $Na_xCa_{1-x}Al_{2-x}Si_{2+x}O_8$ s.s., which were prepared under subsolidus conditions; they revealed some advantages of sodium-rich $Na_xCa_{1-x}Al_{2-x}Si_{2+x}O_8$ s.s. ($0.8 \leq x \leq 1$) over anorthite ($x = 0$). The sintering temperature decreased with increases in x from 1300 °C for anorthite to 1000 °C for albite ($x = 1$), which were affected by

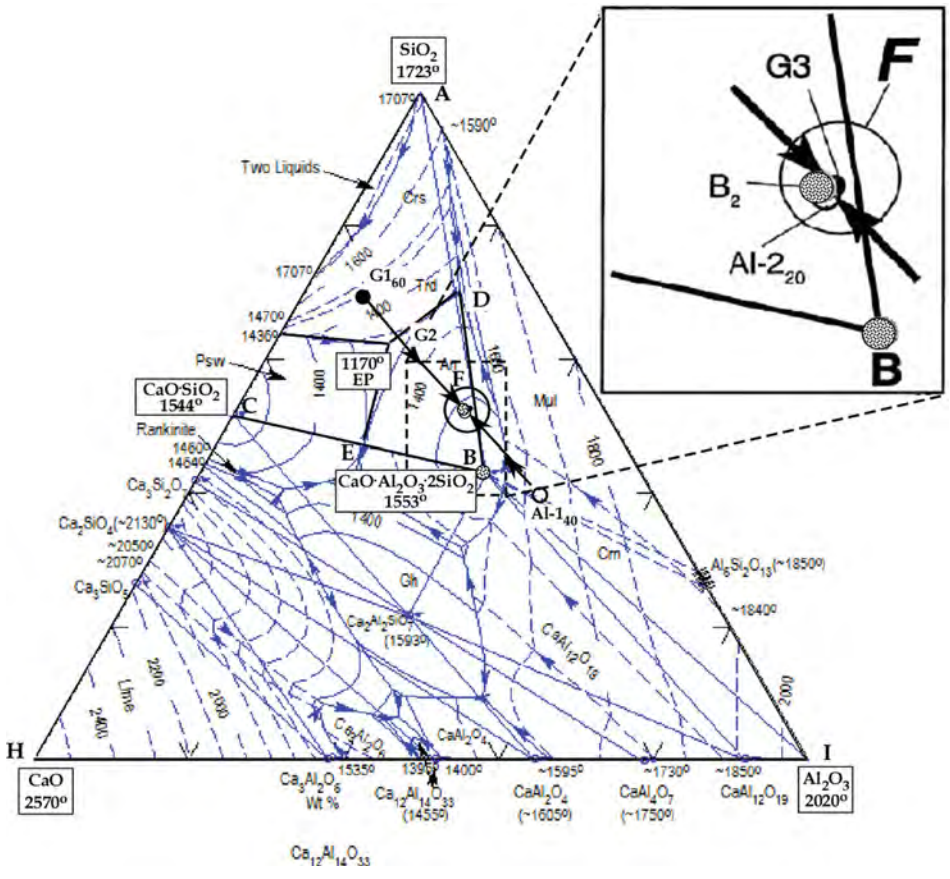

Figure 5.40 *Sintering process of LFC containing anorthite as the main composition; start composition: •60% Gl_{60} + ○40% Al_2O_3 + 10 wt% B_2O_3, final composition: anorthite (•B_2) + 20%Al_2O_3(○Al-2_{20}) + glass (•G3:B_2O_3•SiO_2) [70]. Source: Reproduced with permission from Nishigaki 2005.*

eutectic points located between albite–nepheline and albite–SiO_2. The dielectric properties are shown in Figure 5.41. The τ_f of anorthite ($x = 0$) was –140 ppm/°C, and the values approached near to zero ppm/°C with increasing x. The dielectric constants ε_r were decreased gradually because of the higher dielectric polarizability of Ca^{2+} compared with Na^+. These values were obtained from the samples (solid circles as shown in the figure) and cooled quickly, which means uncontrolled cooling in an oven by natural convection, conduction, and radiation to room temperature. The dielectric constants of slow cooled samples are also shown in the figure by squares, which are almost the same values. The *Qf* values of the samples are shown in Figure 5.41b as solid circles for uncontrolled cooling and squares for cooling with a rate of 0.5 °C/min. The slow-cooling samples showed nearly two times higher *Qf* values than that of first-cooling samples in the sodium-rich $Na_xCa_{1-x}Al_{2-x}Si_{2+x}O_8$ s.s. ($0.8 \leq x \leq 1$). The improvement might be due to short-range ordering (SRO) of Al/Si,

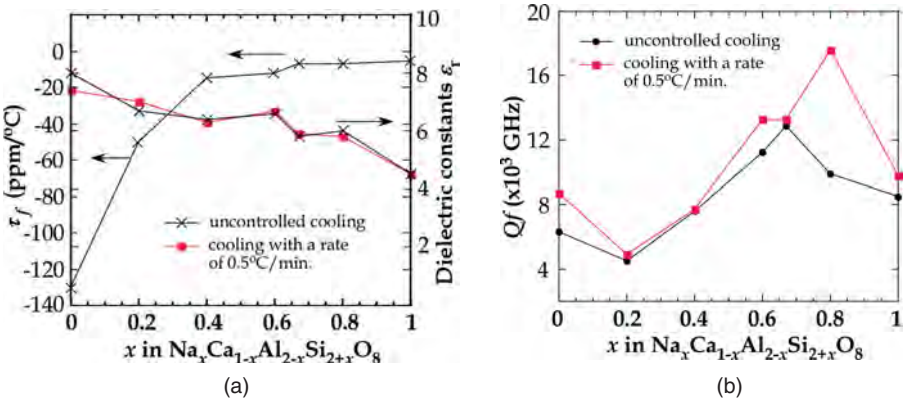

Figure 5.41 *Dielectric properties of plagioclase feldspars $Na_xCa_{1-x}Al_{2-x}Si_{2+x}O_8$ s.s: (a) τ_f and ε_r, (b) Qf as a function of x. Source: Adapted from Krzmanc 2005 [71].*

but there is no evidence from the XRPD data for any increase in the long-range ordering (LRO).

On the other hand, in this section, effects of substitution of Ge for Si are considered on the point of view of covalencies affecting the dielectric constant and quality factor. Additional effects of the substitution of Ge for Si on the feldspars are now presented. One effect is on the point of view of LTCC technology because of their sintering temperature and the tetrahedral ordering that strongly influences the dielectric losses in the microwave frequency range. Krzmanc also presented Ge-plagioclase feldspars $K_xBa_{1-x}Ga_{2-x}Ge_{2+x}O_8$ s.s. concerning Ge and Ga instead of Si and Al on the theme of this section [72]. The Ge–feldspars were also synthesized under subsolidus conditions using a solid-state reaction technology. In this series, there are two types of crystal structure, *C*2/*m* (No. 12) and $P2_1/a$ (No. 14). The first one is stable up to the melting point, which is disordered Ga and Ge ions in the 8*j* Wyckoff notation positions. The second one is obtained by annealing in the temperature range 800–900 °C for $x = 1$, 0.9, and 0.67, and observed up to near the melting point at $x = 0.4$ and 0, which is probably more ordered than the *C*2/*m* structure but the ordering could not be determined by the Rietveld method. The $P2_1/a$ (No. 14) modification on $x = 0.67$ exhibited a three-times-higher *Qf* value and a lower ε_r than the *C*2/*m* (No. 12) modification. At the same time, there is no significant change of τ_f. $P2_1/a$ (No. 14) Ge–feldspars exhibiting ε_r of 5.9–7.0, *Qf* values of 95 000–106 000 GHz, and a τ_f of –25 ppm/°C are promising candidates for microwave applications and LTCC technology.

5.4.6 Corundum

5.4.6.1 Alumina

Alumina is a good candidate for millimeter-wave dielectrics because of the high *Qf* of 680 000 GHz and low ε_r of 10.05 [18]. The *Qf* of a single crystal was reported to be 1 000 000 GHz [73, 74]. Huang *et al.* [75] reported Al_2O_3 ceramics with a high *Qf* of 634 000 GHz using high purity nano $(\alpha + \theta)$–Al_2O_3 powders and Alford *et al.* [74] 500 ppm doped Al_2O_3 with a high *Qf* of 500 000 GHz.

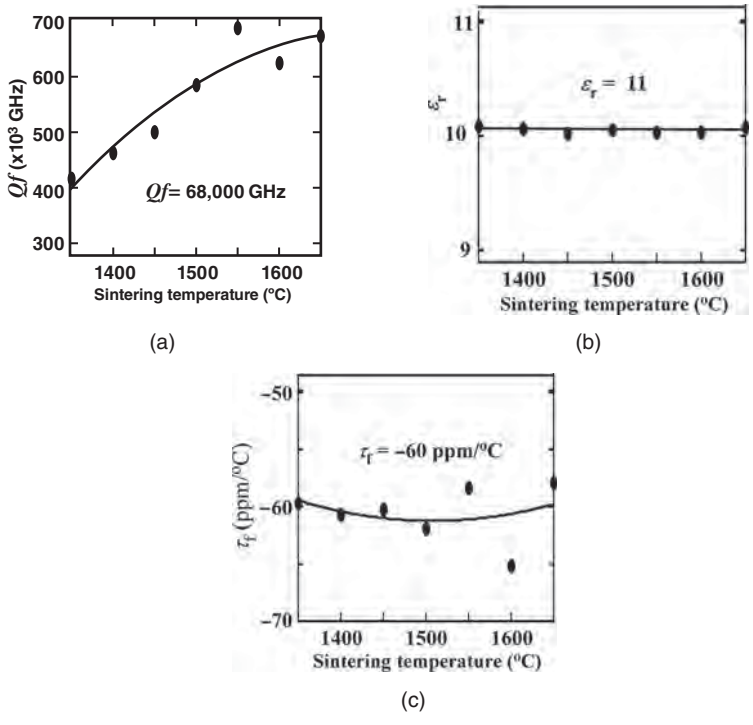

Figure 5.42 *Microwave dielectric properties of alumina ceramics: (a) Qf, (b) ε_r, and (c) τ_f as a function of the sintering temperature. Source: Adapted from Ohsato et al. 2003 [18].*

Figure 5.42 shows the microwave dielectric properties of alumina ceramics as a function of sintering temperature [18, 30]. The *Qf* value increases with an increase in sintering temperature. In the temperature range higher than 1500 °C, the *Qf* values are improved to more than 600 000 GHz and the highest *Qf* value of 680 000 GHz was obtained when sintered in the temperature range of 1550 to 1650 °C. This value is the highest *Qf* in the world as far as we know for single-phase alumina ceramics with the exception of a single crystal. These samples were well sintered with a high relative density, more than 99.5%, as shown in Figure 5.43a. The mean grain size measured using SEM figures were also increased with the sintering temperature, as shown in Figure 5.43b. The relationship between *Qf* and grain size is shown in Figure 5.43c. The *Qf* values increased almost linearly to 600 000 GHz up to 3 μm grain size, and showed the highest value of 680 000 GHz at a mean grain size of 5 μm. The *Qf* value of 370 000 GHz presented by Alford *et al.* [76] is fitted on the curve of a 1 to 2 μm grain size, which was measured from the SEM figure presented in their papers.

5.4.6.2 Improvement of τ_f of Alumina

The τ_f of alumina is expected to decrease to near zero ppm/°C by adding rutile with τ_f = +450 ppm/°C. Although the formation of Al_2TiO_4 prevents near-zero τ_f, annealing brings

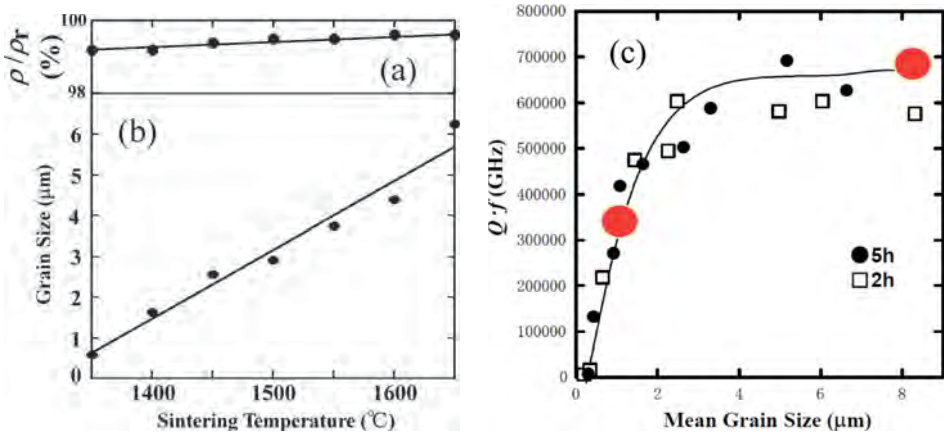

Figure 5.43 *(a) Density and (b) mean grain size of alumina ceramics as a function of sintering temperature, and (c) Qf values as a function of mean grain size of alumina ceramics. Source: Adapted from Miyauchi 2008 [30].*

the decomposition of Al_2TiO_4 and achieved near-zero τ_f [18, 77]. Figure 5.44 is a phase diagram for TiO_2–Al_2O_3 [78], which shows Al_2TiO_5 as a stable phase above 1200 °C. Addition of 10 mol% TiO_2 to alumina (10 mol% TiO_2–90 mol% Al_2O_3) adjusted τ_f to near zero when sintered at 1350 °C for 5 hours. Figure 5.45a and b show τ_f and ε_r as a function of sintering temperature. The τ_f values of a sintered sample (solid circle) decrease at above 1300 °C due to the formation of Al_2TiO_5. Therefore, Miyauchi *et al.* [77] annealed the samples at a lower temperature of 1100 °C to decompose Al_2TiO_5. The τ_f improved from –40 to near zero ppm/°C on annealing at 1350 °C, as shown in Figure 5.45a. The *Qf* and ε_r also changed from 142 000 to 114 000 GHz and 11.6 to 12.4, respectively.

5.4.6.3 New-Type Corundum with Ordered Structure

A new corundum-type $Mg_4Nb_2O_9$ (MN) compound shows a high *Qf* of 194 000 GHz with a low ε_r of 12.4 and is a candidate for millimeter-wave dielectrics [79]. Ogawa *et al.* found

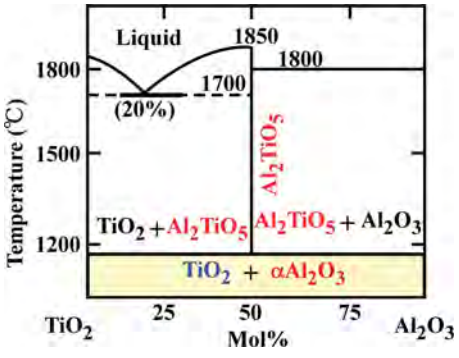

Figure 5.44 *TiO_2—Al_2O_3 phase diagram. Source: Adapted from Levin 1975 [78].*

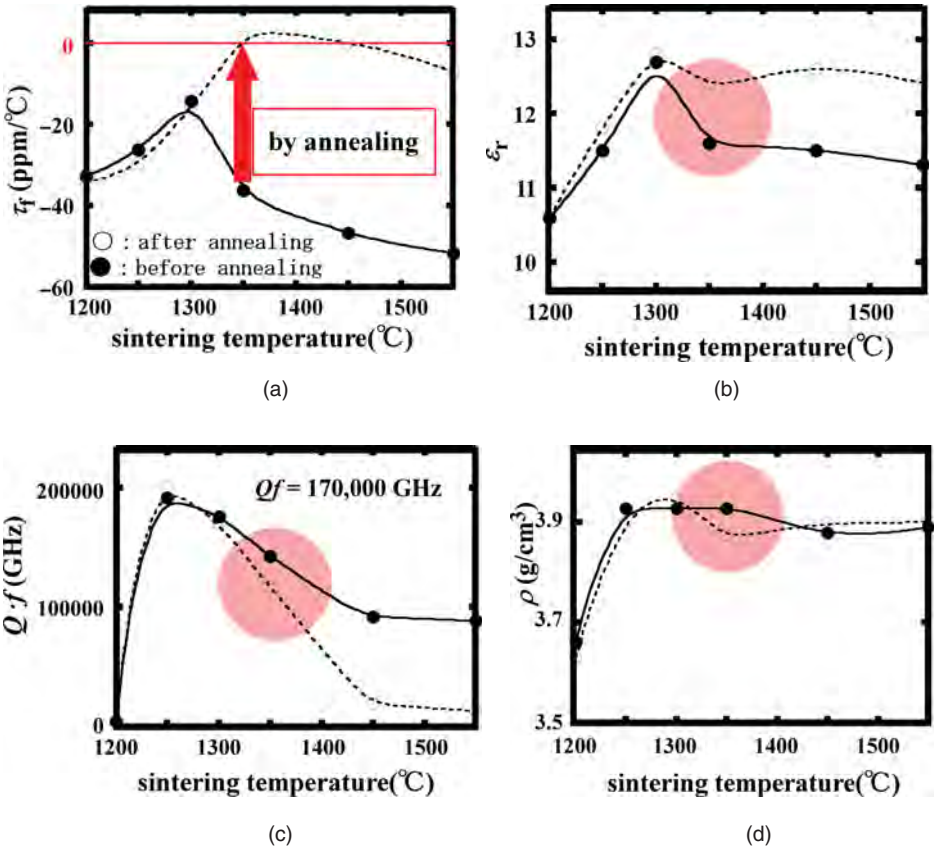

Figure 5.45 *(a) τ_f, (b) ε_r, (c) Qf, and (d) ρ of TiO_2-added alumina as a function of sintering temperature. Solid and open circles show data before and after annealing, respectively. Source: Adapted from Miyauchi et al. 2006 [77].*

this compound with a high *Qf* for the substrate of a high-temperature superconductor film. It was found that $Mg_4(Nb_{2-x}Ta_x)O_9$ (MNT s.s., $0 \le x \le 2$) and $Mg_4(Nb_{2-x}Sb_x)O_9$ (MNS s.s., $0 \le x \le 1$) solid solutions have the highest *Qf* of 350 000 GHz at $x = 2$ and 280 000 GHz at $x = 1$, respectively [80, 81].

Figure 5.46 shows the crystal structure of alumina and the new-type corundum [82]. Crystal data of corundum are as follows: crystal system: trigonal, space group: *R*3*c* (No. 167), lattice parameter: $a = 4.758$, $c = 13.991$ Å. This crystal structure is composed of octahedrals stacked along the *c*-axis in a threefold manner, and two-thirds of the face-shared octahedrals are occupied by Al ions. The crystal data of the new-type corundum are as follows: crystal system: trigonal, space group: $P\bar{3}c1$(No. 165), lattice parameter: $a = 5.1612(7)$, $c = 14.028(1)$ Å. This crystal structure is the ordered corundum structure, in which cations are ordered at two-thirds of octahedral sites in the hexagonal closest packed oxygen array along the *c*-axis. The cation stacking along the *c*-axis is the manner of –Mg(1)–(Mg(2), Nd)–Vacancy–(Mg(2), Nd)–Mg(1)–, with the $Mg(1)O_6$ octahedron being

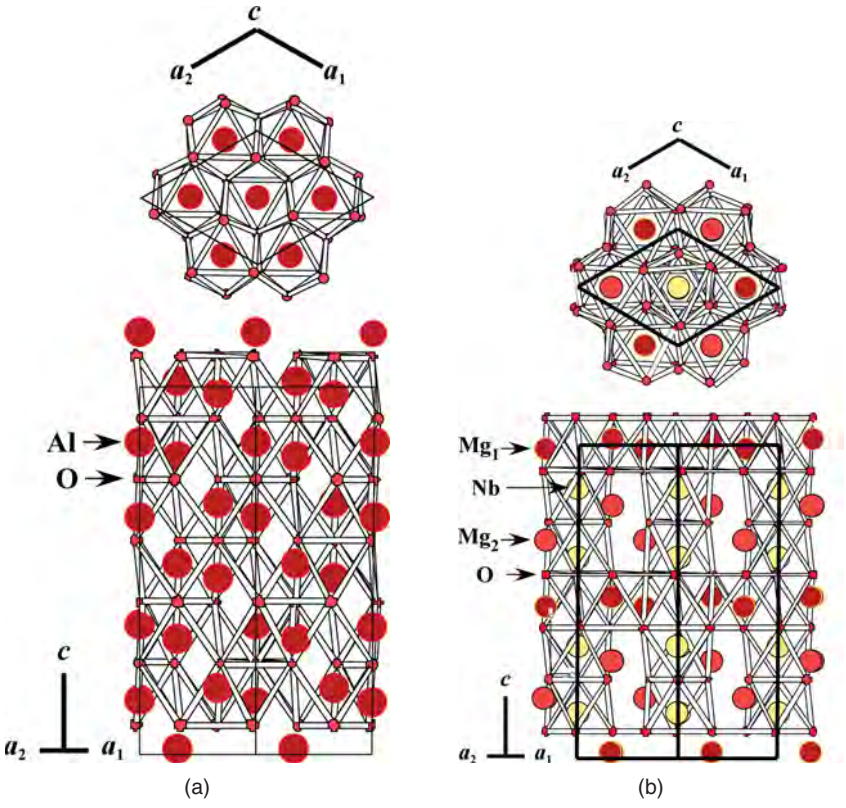

Figure 5.46 *Crystal structure of (a) alumina and (b) new-type corundum.*

face-shared with the $Mg(2)O_6$ octahedron and edge-shared with the $Mg(1)O_6$ octahedron, while the NbO_6 octahedron is face-shared with the NbO_6 octahedron and edge-shared with the $Mg(2)O_6$ octahedron.

Origins of high Q and low ε_r of the new-type corundum ceramics are presented using bond strengths derived on the bases of the bond valence theorem [54, 55] and the discrete variable X_a(DV–X_a) method [83,84]. In this section, the two solid solution series described above are reviewed based on the researches of Ogawa's group. In the case of MNT solid solutions [80], these solid solutions are made in the whole range of $x = 0$–2 because they have the same ionic radius of 0.64 Å. The total density of states (DOS) and the energy level diagrams of MN ($x = 0$) and MT ($x = 2$) are calculated using the cluster model of $(Mg_4M_2O_{62})^{-26}$ (M = Nb and Ta) by the discrete variable X_a(DV–X_a) method, as shown in Figure 5.47. In the energy-level diagrams, the solid and dotted lines indicate the occupied and unoccupied molecular orbitals, respectively. The highest occupied molecular orbital (HOMO) levels lie on the top of the O–2p valence band; the occupied bands located from –7 to 0 eV and from –20 to –15 eV are mainly composed of O–2p and O–2s orbitals, respectively. The unoccupied orbitals located above 5 eV of MN and MT are made up of Mg–3s, Nb–4d, and Ta–5d orbitals, as shown in Figure 5.47. Significant amounts of Nb–4d

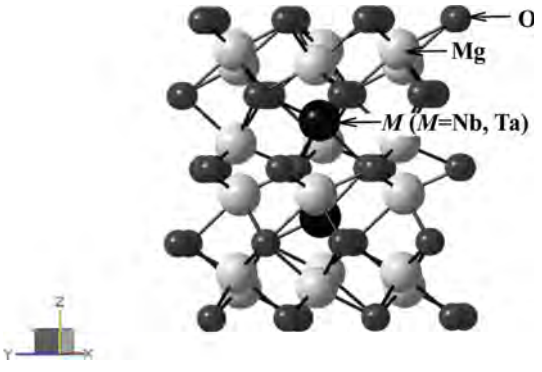

(a)

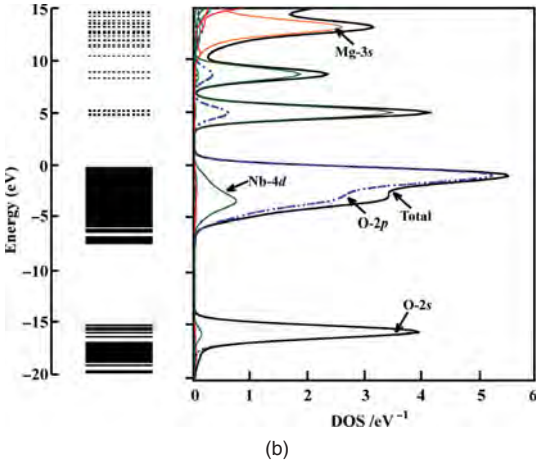

(b)

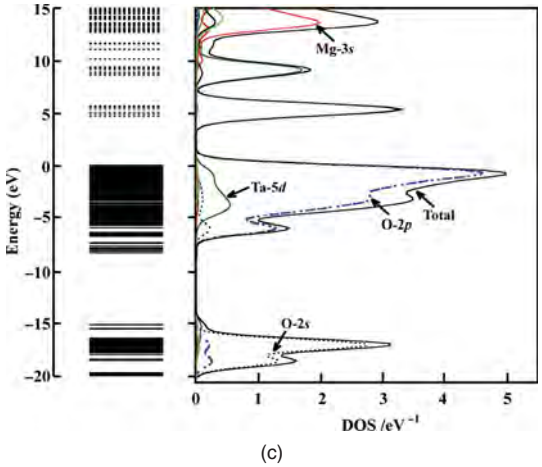

(c)

Figure 5.47 *(a) Cluster model used in the calculation: $(Mg_4M_2O_{22})^{-26}$ (M = Nb and Ta). Energy level diagrams and total and partial density state of (b) MN and (c) MT by $(Mg_{18}M_2O_{60})^{-74}$. Source: Adapted from Ogawa et al. 2003 [80].*

and Ta–5d states in the O–2p band are found, suggesting that the Nb—O and Ta—O bonds are covalent. The net charges, which define the ionicity of atoms, for the Nb and Mg ions at MN were 2.55 and 1.81, respectively, and those of the Ta and Mg ions at MT were 2.55 and 1.82, respectively. Thus, the covalent interactions of the Nb—O and Ta—O bonds are considered to be strong and the Mg—O bond at MN and MT may be an ionic interaction. From these results, it is considered that the Ta substitution for Nb in the MNT s.s. exerts an influence on the average bond strength of the Nb—O and Ta—O bonds in the NbO_6 and TaO_6 octahedra. The bond order, which represents the strength of covalent Nb—O and Ta—O bonding in NbO_6 and TaO_6 octahedra, were determined in order to discuss the covalent interactions in more detail. The bond order of Ta—O bonds (0.180) is larger than that of the Nb—O bonds (0.133), whereas those of the Mg—O bonds in $Mg(1)O_6$ and $Mg(2)O_6$ did not change with Ta substitution for Nb. From these results it is evident that the Ta—O bond became more covalent than that of the Nb—O bond. The ε_r of MT is found to be lower than that of MN, as shown in Figure 5.48a. The variation of the ε_r values with x is similar to that of ionic polarizability (α_{obs}), as shown in Figure 5.48b, which are estimated by the Clausius–Mossotti equation as follows:

$$\alpha_{obs} = 1/b[V_m(\varepsilon - 1)/(\varepsilon + 2)] \tag{5.9}$$

where ε and V_m represent the measured dielectric constants and molecular volumes, and the constant value b is $4\pi/3$. The Qf values of MNT increase drastically from 194 000 to

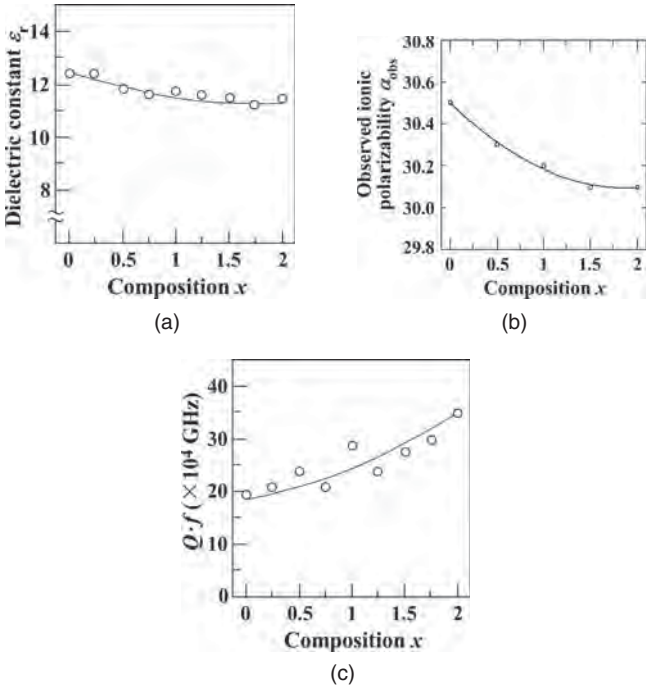

Figure 5.48 *(a) ε_r, (b) α_{obs}, and (c) Qf of MNT s.s. as a function of composition x. Source: Adapted from Ogawa et al. 2003 [80].*

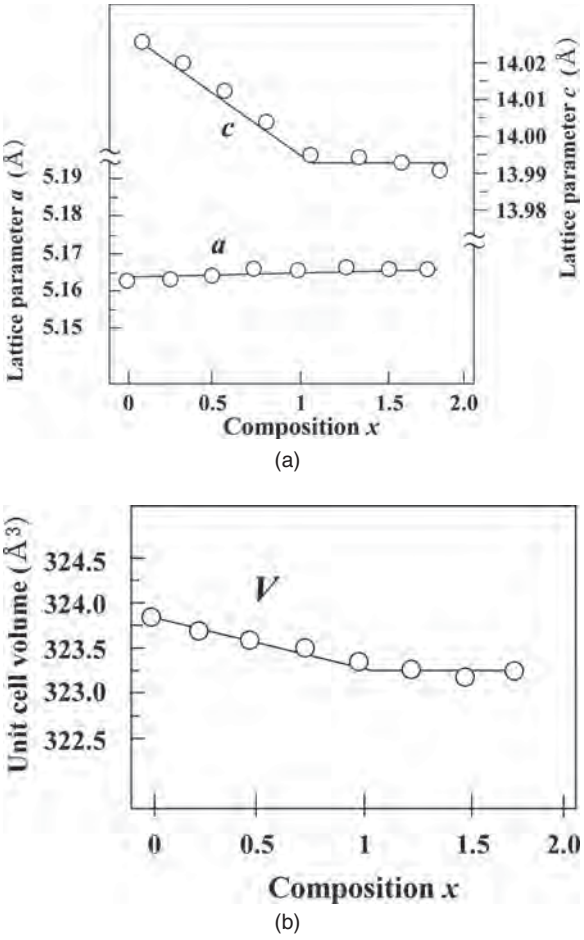

Figure 5.49 *(a) Lattice parameters and (b) volumes of MNS s.s. as a function of composition x. Source: Adapted from Ogawa et al. 2005 [81].*

347 000 GHz with increasing composition x, as shown in Figure 5.48c. The *Qf* also might be increased by decreasing the dielectric losses based on reducing the rattling due to the covalency of MT stated above.

In the case of $Mg_4(Nb_{2-x}Sb_x)O_9$ (MNS) system [81], the MNS compound makes s.s. in the composition range x from 0 to 1. It is revealed by Vegard's rule that the applied lattice parameter changes as shown in Figure 5.49. The normalized covalency of the Sb–O bond is higher than that of Nb—O bond, although normalized covalency of the Mg—O bond was not observed and differences in the composition range $x = 0$ to 1 are as shown in Figure 5.50. The covalencies are calculated using Equation (5.5) of bond strength theory stated in Section 5.4.3. The total and partial DOS of the Nb- and Sb-centered cluster models with $(AMg_{12}O_{45})^{-61}$ (A = Nb and Sb) clusters are shown in Figure 5.51, which are calculated in the same way as MNT s.s. stated above. The mixture of Nb–4d and Sb–5p states in the

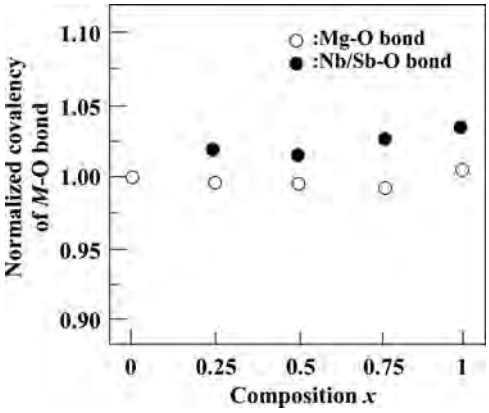

Figure 5.50 *Normalized covalency of Mg—O and (Nb/Sb)–O bonds as a function of composition x. Source: Adapted from Ogawa et al. 2005 [81].*

O–2p band suggests the strong covalent interaction between pentavalent cations (Nb and Sb) and oxygen. The ionicities of MN and MS are almost the same, which were determined from the net charge. The covalency of the Sb–O bond is larger than that of the Nb—O bond based on the bond order: that of Sb–O is 0.180 and that of Nb—O is 0.133. As a result, the Sb substitution for Nb in MNS strengthens the covalency as evaluated based on the normalized covalency of Nb/Sb–O bond (Figure 5.50).

Figure 5.52 shows the microwave dielectric properties of MNS s.s. as a function of composition x [81]. The ε_r values are decreased from 13 to 10 with x, which are expected to increase by the increase in the ionic polarizability: 3.97 A^3 for Nb^{5+} ion and 4.27 A^3 for Sb^{5+} ion. The decrease in the ε_r may relate to the variations in the covalency of Nb/Sb–O in $(NbSb)O_6$ octahedra calculated by the bond valence theorem and the discrete variable $X_a(DV\text{–}X_a)$ described earlier. The Qf values of MNS s.s. are increased from 193 000 to 283 000 GHz in the single-phase region with composition x from 0 to 1 as shown in Figure 5.52a. The improvement in the Qf value of MNS s.s. exhibited a similar tendency to those of MNT s.s., which is exerted by the enhancement of covalency of the Sb/Nb—O bonds. The τ_f of MNT locates approximately at –70 ppm/°C in the single-phase region, which is not influenced by the substitution of Sb for Nb.

5.4.7 Spinel

Aluminate spinel (AAl_2O_4) and gallium spinel (AGa_2O_4) (A = Mg, Zn) are reported for millimeter-wave dielectrics with high Qf and low ε_r. Mg– and Zn–aluminate spinel ceramics show high Qf of 105 000 and 56 000 GHz, low ε_r of 8.5 and 8.5, and τ_f of –63 and –79 ppm/°C, respectively [33,85]. Moreover, Mg– and Zn–gallium spinel ceramics show a high Qf of 117 000 and 94 600 GHz, low ε_r of 9.5 and 10.4, and τ_f of –4 and –27 ppm/°C, respectively [86,87]. More recently, Mg– and Zn–gallium spinel ceramics sintered at 1475 and 1550 °C showed a high Qf of 298 000 and 220 000 GHz and low ε_r of 9.2 and 9.8, respectively [88]. Figure 5.53 shows the crystal structure of the AB_2O_4 spinel [89] viewed from perpendicular to the [111] direction (this figure is also in the Plate Section). The red

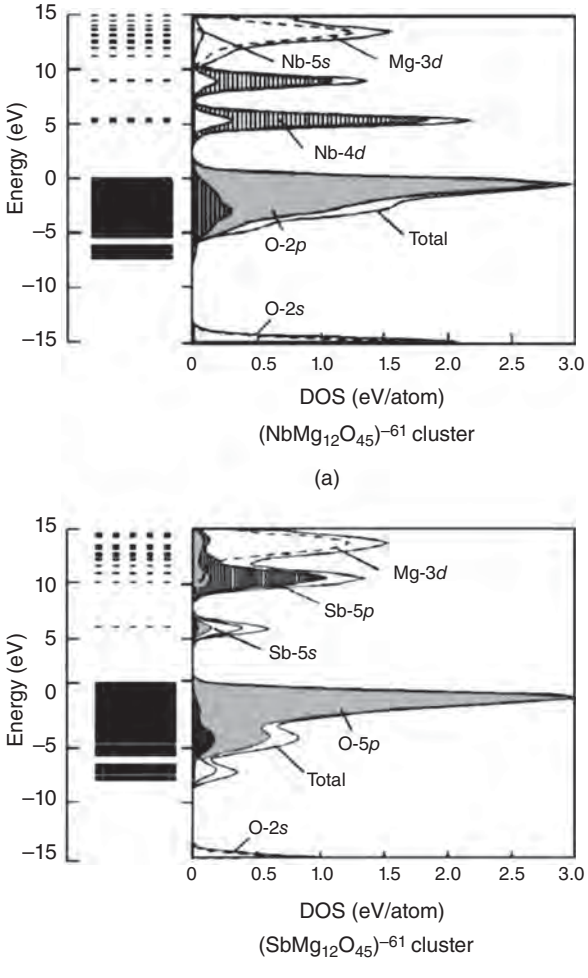

Figure 5.51 *Energy-level diagrams and total and partial density of states of (a) $Mg_4Nb_2O_9$ and (b) $Mg_4Sb_2O_9$ by $(AMg_{12}O_{45})^{-61}$ (A = Nb and Sb) cluster. Source: Adapted from Ogawa et al. 2005 [81].*

balls are oxygen ions, which form the closest packing layers, the green ones are *B* ions located in octahedra (*O*), and the yellow ones are *A* ions located in tetrahedra (*T*). Among the oxygen closest packing layers, AO_4 *T*-sites and BO_6 *O*-sites are located, whose positions are 8*a* and 16*d* in the Wyckoff notation in the $Fd\bar{3}m$ (No. 227) space group [90], respectively. There are two different layers: one is occupied by only the BO_6 octahedron and another is occupied by the BO_6 octahedron and AO_4 tetrehedon. The crystal structure of $A[B_2]O_4$ stated here is named as the "normal spinel" and that of $B[AB]O_4$ is named as the "inverse spinel." In the crystal structure of the inverse spinel, half of *B* ions occupy the *T*-sites and the residual half of *B* ions and *A* ions occupy the Osites. Moreover, there is an "intermediate spinel" $AB[AB]O_4$ between the normal and inverse spinels [92].

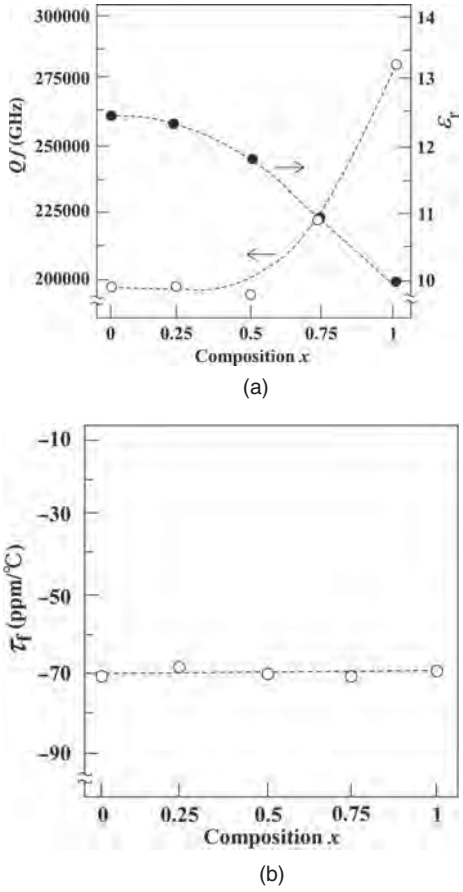

Figure 5.52 *(a) The Qf and ε_r values and (b) τ_f of MNS s.s. as a function of composition x. Source: Adapted from Ogawa et al. 2005 [81].*

Kan *et al*. [91] studied cation distributions and microwave dielectric properties of the $MgGa_2O_4$ intermediate spinel. Figure 5.54 shows the microwave dielectric properties of $MgGa_2O_4$ as a function of firing temperature from 1500 to 1600 °C. The *Qf* values considerably increased from 92 000 to 298000 GHz with an increasing firing temperature. Well-sintered samples at temperatures above 1540 °C with 96% relative densities showed excellent *Qf* in the range 250 000 to 300 000 GHz and low dielectric constants of 9.0–9.3. Figure 5.55a shows the lattice parameters and degree of inversion *x*, Figure 5.55b the volume values of *T* and *O* sites, and Figure 5.55c the covalencies of *T* and *O* sites as a function of the firing temperature from 1500 to 1600 °C. The degree of inversion *x* in the $Mg_{1-x}Ga_x[Mg_xGa_{2-x}]O_4$ intermediate spinel estimated from the site occupancies of *T* and *O* sites obtained by Rietveld crystal structure analysis are slightly decreased from 0.88 to 0.84 with firing temperature (Figure 5.55a). The obtained structural formulas of the intermediate $MgGa_2O_4$ spinel are $Mg_{0.12}Ga_{0.88}[Mg_{0.88}Ga_{1.12}]O_4$ and $Mg_{0.16}Ga_{0.84}[Mg_{0.84}Ga_{1.16}]O_4$, at 1500 and 1600 °C, respectively. The amount of the Mg^{2+} cations increases in *T* sites and

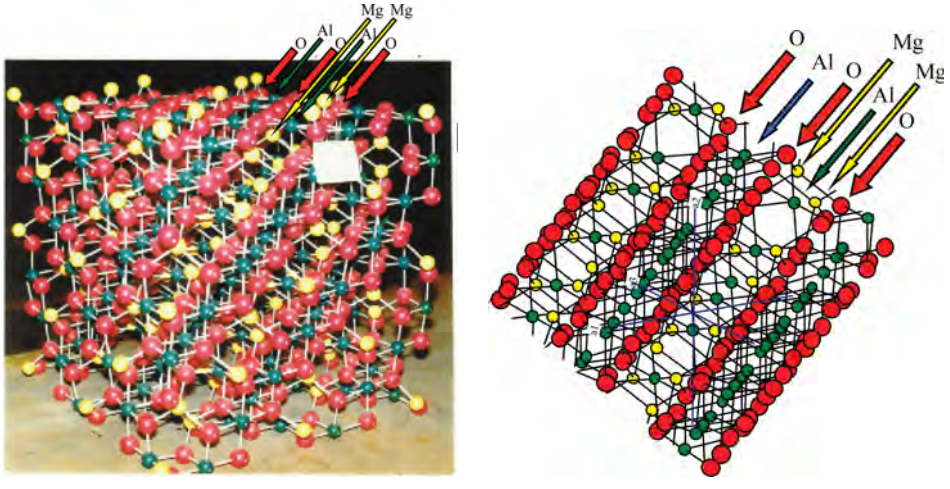

(a) (b)

Figure 5.53 *(a) Model of crystal structure of spinel, which is exhibited in KEK Tsukuba, made by Dr Y. Kudoh and students of Professor Y. Takeuchi's group at the University of Tokyo. (b) Illustrated spinel structure from perpendicular to [111] direction with the same angle as (a). This figure is also in the Plate Section.*

that of the Ga^{3+} cations increases in *O* sites with firing temperature. Covalency values of a *T*-site increase and those of an *O*-site decrease with the firing temperature (Figure 5.55c), which are calculated using Equation (5.5) in Section 5.4.3.1. The covalence value of the *T* site increasing at 1600 °C might affect the *Qf* values as in the case of indialite (Figure 5.29) and Sr–wollastonite discussed in Sections 5.4.3.1 and 5.4.4.1, respectively. The increase in the lattice parameters as shown in Figure 5.55a could not be explained by using the radius of the ion in the polyhedron, but it could be explained by increasing the volume of the *O* site, which depends on decreasing covalencies, as shown in Figure 5.55b and c.

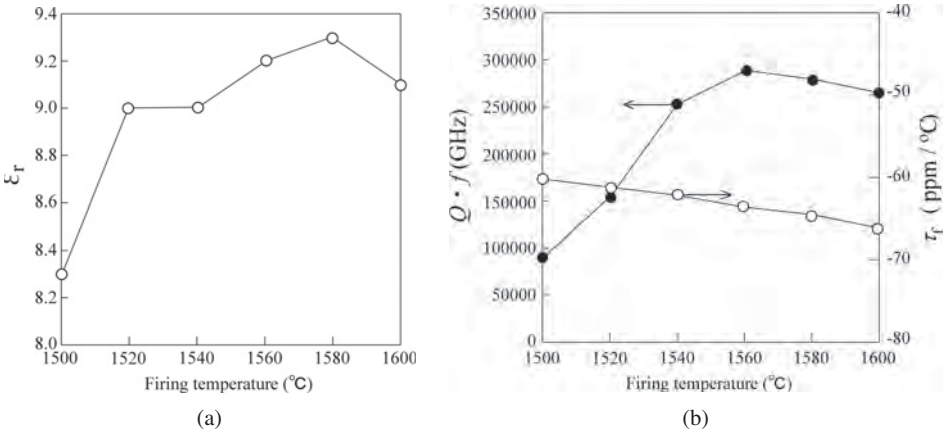

(a) (b)

Figure 5.54 *Microwave dielectric properties of $MgGa_2O_4$. Source: Kan et al. 2013 [91].*

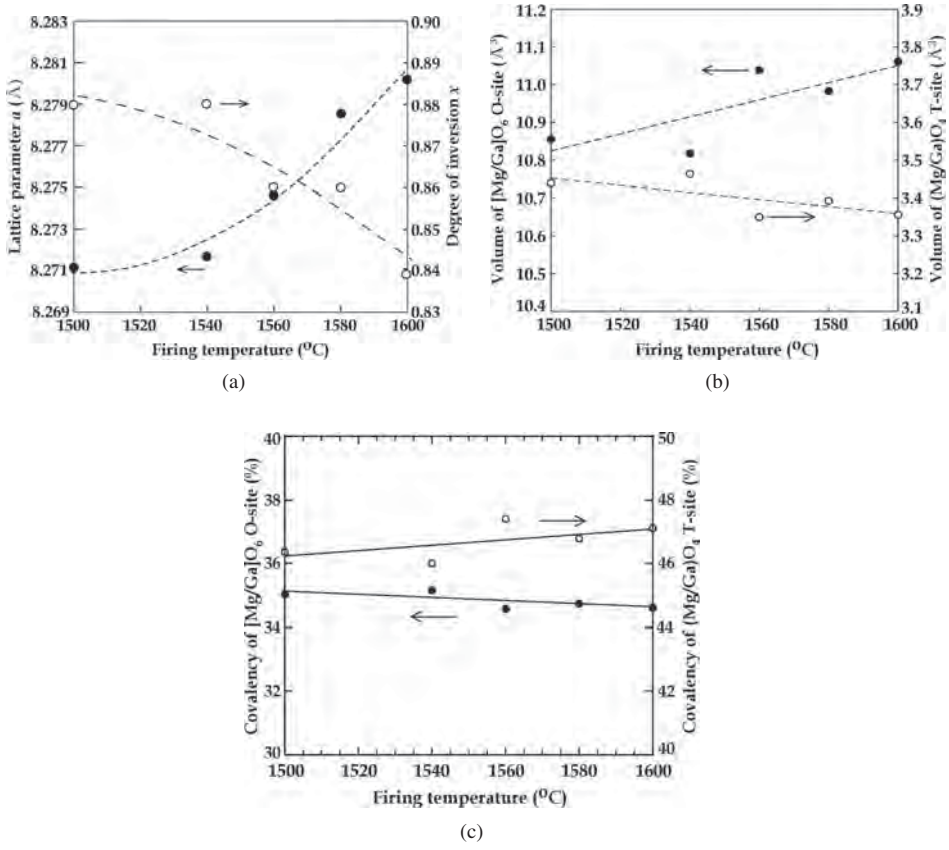

Figure 5.55 *(a) Lattice parameter of $MgGa_2O_4$ and degree of inversion x of $Mg_{1-x}Ga_x[Mg_xGa_{2-x}]O_4$, (b) volume values and (c) covalency of T- and O-sites of $MgGa_2O_4$. Source: Kan et al. 2013 [91].*

Kan *et al*. [88] also studied crystal structures and microwave dielectric properties of spinel-structured $(Mg_{1-x}Zn_x)Ga_2O_4$ s.s. One of the end members, $MgGa_2O_4$ ceramics sintered at 1500 °C, is an intermediate spinel with a degree of inversion of 0.88, as described earlier, and $ZnGa_2O_4$ ceramics are normal spinels with a degree of inversion of 1.0 [86, 87]. These compounds reveal whole s.s. by the linearly increased lattice parameter due to Vegard's law, as shown in Figure 5.56a. Figure 5.56b and c show volumes and covalencies of *O* and *T*, respectively, which are estimated from the refined atomic coordinates and lattice parameters stated earlier. The change of covalency with composition *x* are also confirmed by volume changes of *O* and *T* with composition *x*. In the tetrahedron, the covalency of the cation–oxygen bond slightly decreased depending on the Zn ions occupied preferentially. As the electronegativity of the Zn ion (1.6) is larger than that of Mg (1.2), ionicity of the Zn–O bond showing opposite character is becoming large. This is consistant with the change of covalency. Figure 5.57a, b, and c show the relative density, dielectric constant, and quality factor *Qf* values, respectively, as a function of the firing temperature. The variations of ε_r values are similar to those of relative density.

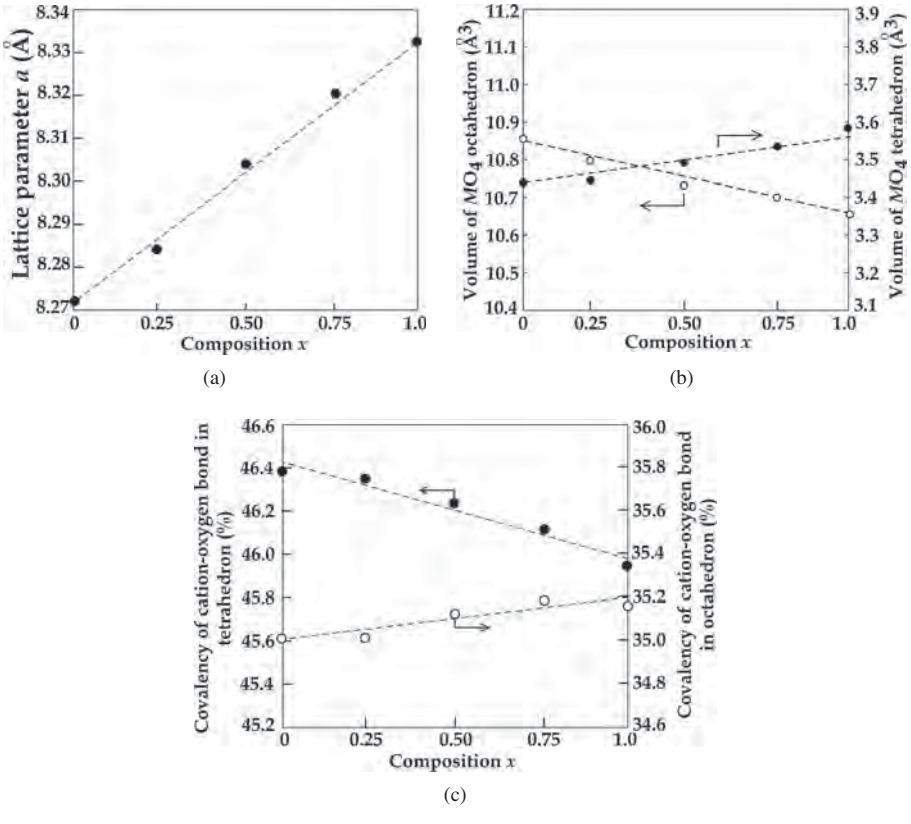

Figure 5.56 *(a) Lattice parameter, (b) volume of MO_4 tetrahedron and MO_6 octahedron, and (c) covalency of the M–O bond in MO_4 tetrahedron and MO_6 (M = Mg, Zn, Ga) octahedron as a function of composition x of $(1 - x)MgGa_2O_4$–$xZnGa_2O_4$ ceramics fired at 1500 °C for 2 h in air. Source: Kan et al. 2014 [88].*

Above 1475 °C, the relative densities in the composition range of 0.25 to 1.0 are saturated and the *Qf* value of $ZnGa_2O_4$ of $x = 1.0$ showed an excellent 240 000 GHz and those of $0.25 \leq x \leq 0.75$ approximately 180 000 GHz. In the case of $MgGa_2O_4$, the relative density and *Qf* values of random variations with the firing temperature are shown in Figure 5.57c, and the *Qf* value at 1550 °C shows a very high value of 298 000 GHz. These *Qf* values of $(Mg_{1-x}Zn_x)Ga_2O_4$ s.s. are much higher than those of $ZnAl_2O_4$ [93] and $MgAl_2O_4$ [85] spinel ceramics. The dielectric constants ε_r of $(Mg_{1-x}Zn_x)Ga_2O_4$ s.s. are approximately 9.8, being suitable for millimeter-wave dielectrics, but the τ_f values show around –64 ppm/°C. Further research is needed to improve τ_f for commercial applications.

5.4.8 Borate, Phosphate, and Vanadate

5.4.8.1 Borate

There are several borate materials such as $A_3B_2O_6$ (A = Mg, Zn), AB_2O_4 (A = Ca, Sr, Ba), RBO_3 (R = La, Nd, Sm, Dy, Ho, Y) with high *Qf* and low ε_r useful for millimeter dielectric

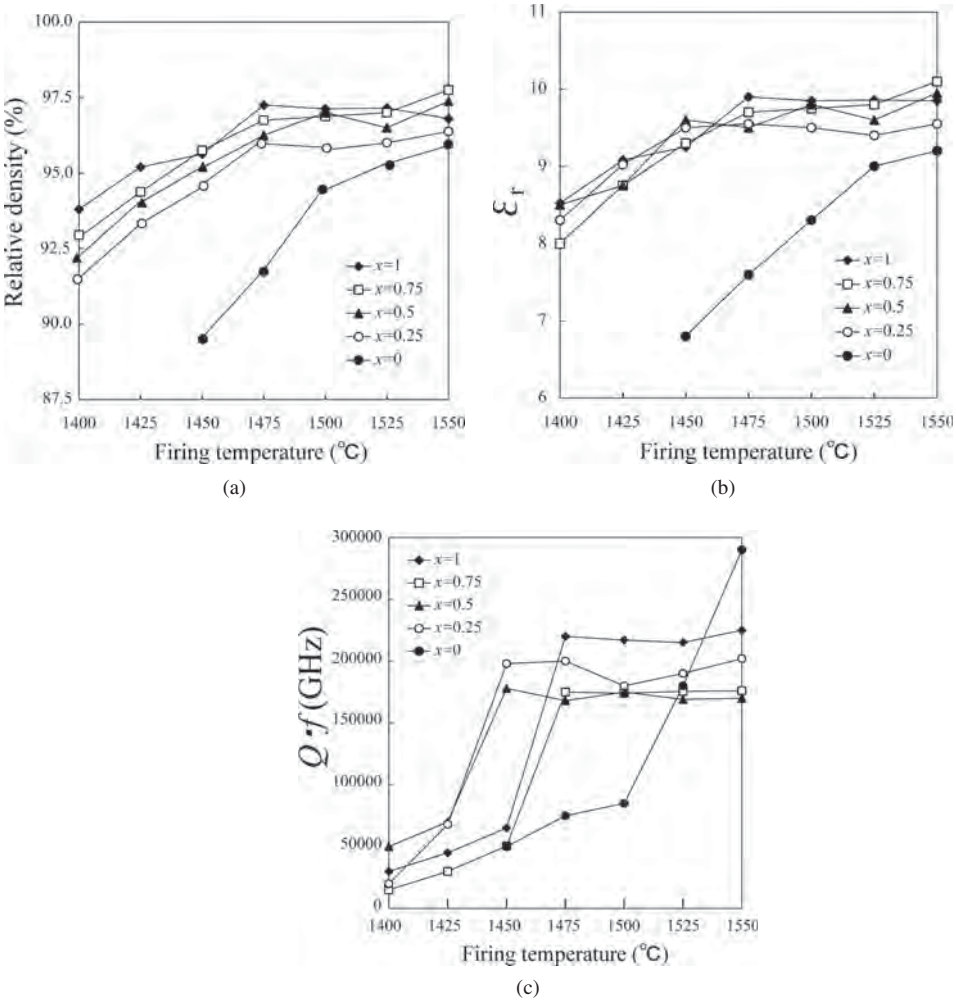

Figure 5.57 *(a) Relative density, (b) the ε_r values, and (c) Qf of $(Mg_{1-x}Zn_x)Ga_2O_4$ s.s. as a function of the firing temperature. Source: Kan et al. 2014 [88].*

applications. Magnesium borate $Mg_3B_2O_6$ (Kotoite) was originally found during research on new glass-ceramics for LTCC by Mori *et al*. (2006) [94]. $Mg_3B_2O_6$ has good microwave dielectric properties with Qf = 150 400 GHz, ε_r = 7.2. Nishizuka *et al.* [95] synthesized $Mg_3B_2O_6$ from the nominal composition of MgO–25 mol% B_2O_3 by sintering at 1320 °C. It has the best Qf value of 310 000 GHz, ε_r = 7.2, and τ_f = –60.6 ppm/°C. The $Mg_3B_2O_6$ compound also precipitated with MgO at 1330 °C for 2 hours from the nominal composition of MgO–33 mol% B_2O_3 ($Mg_2B_2O_5$) with properties of Qf = 260 100 GHz, ε_r = 7.4, and τ_f = –60.0 ppm/°C [95]. The $Mg_3B_2O_6$ ceramics obtained from $Mg_3B_2O_6$–5 wt% $Mg_2B_2O_5$ composition showed 10 times larger grains and showed a high Qf of 240 000 GHz

and $\varepsilon_r = 7$ [96]. Doslar *et al*. [97] also reported similar properties on the $Mg_3B_2O_6$ ceramics synthesized by a solid-state reaction. $Zn_3B_2O_6$ ceramics, with Zn substituted for Mg, is also a promising candidate for LTCC substrate application, which shows the properties of *Qf* value of 58 535 GHz, $\varepsilon_r = 6.8$, and $\tau_f = -58$ ppm/°C [98]. AB_2O_4 compounds are used as a low sintering agent, but there are no data on Sebastian's database. On the other hand, $LaBO_3$ ceramics in the RBO_3 (R = La, Nd, Sm, Dy, Ho, Y) series [99, 100] show a high *Qf* of 76 900 GHz, $\varepsilon_r = 11.8$, $\tau_f = -52$ ppm/°C.

5.4.8.2 Phosphate

Phosphate also exhibits a low dielectric constant because the crystal structure is composed by a PO_4 tetrahedron similar to an SiO_4 tetrahedron [101]. The amount of P–O ionic character (p) is 30% calculated by Equation (5.8) in Section 5.4.5. The dielectric constant varies in the range 6 to 12, which is larger than that of silicates. Hence, the phosphates are also candidates for millimeter-wave dielectrics. The phosphates join with PO_4 tetrahedra to form similar structures of silicates. Aluminum phosphate $AlPO_4$ (berlinite) is a similar structure to quartz SiO_2 and is composed of a three-dimensional framework of tetrahedra, with a low *Qf* as compared with quartz with a high *Qf* [102]. The $LiMgPO_4$ compound also has a similar structure with forsterite, which is called as olivine-type compound. The $LiMgPO_4$ compound substituted Zn for Mg exhibits a high *Qf* of 99 700 GHz with a low $\varepsilon_r = 6.7$ and $\tau_f = -62$ ppm/°C [103]. The τ_f was improved to –5 ppm/°C by adding a 0.12 volume fraction of TiO_2 with dielectric properties $\varepsilon_r = 10.1$ and $Qf = 52\,900$ GHz [103].

Complex pyrophosphate compounds AMP_2O_7 (A = Ca, Sr; M = Zn, Cu) [104] could be densified below 950 °C without any glass addition and exhibit a low $\varepsilon_r < 8$, a high *Qf* value and negative τ_f. The $SrCuP_2O_7$ ceramics sintered at 925 °C for 2 hours exhibited the highest *Qf* value of 101100 GHz in this compound series, $\varepsilon_r = 7.04$, and $\tau_f = -64$ ppm/°C. However, this compound seriously reacts with silver at 700 °C, although $SrZnP_2O_7$ could be co-fired with copper in a reduced atmosphere and exhibits $\varepsilon_r = 7.06$, $Qf = 52\,781$ GHz, and $\tau_f = -70$ ppm/°C. Various rare-earth orthophosphates (RPO_4) [105], such as monazite (R = La, Ce, Pr, Nd, Sm, Eu) and xenotime (R = Tb, Dy, Ho, Er, Tm, Yb, Y), exhibited low permittivity, high *Qf*, and negative τ_f values. The higher ε_r and more negative τ_f value of monazite than those of xenotime are attributed to a decrease in *R*–O bond strength. However, the *Qf* value was not affected by the crystal structure and both monazite and xenotime had a similar *Qf* value of approximately 60 000 GHz.

5.4.8.3 Vanadate

The magnesium orthovanadate $Mg_3(VO_4)_2$ ceramics [106] could be sintered at 750 to 1050 °C without any glass addition; the maximum *Qf* value of 65 440 GHz was obtained at 1050 °C accompanied with grain growth of approximately 10 μm. The $(Mg_{3-x}Co_x)(VO_4)_2$ compound with $x = 2$ sintered at 900 °C showed an improvement in *Qf* (78 900 GHz) with a low ε_r of 9.5 and negative τ_f of –94.5 ppm/°C [106]. Figure 5.58a, b, c, and d show, respectively. the bulk density, ε_r, *Qf*, and τ_f as a function of the sintering temperature. The effects of the substitution are exhibited clearly at 850 for $x = 3$, 900 for $x = 2$, and 1000 °C

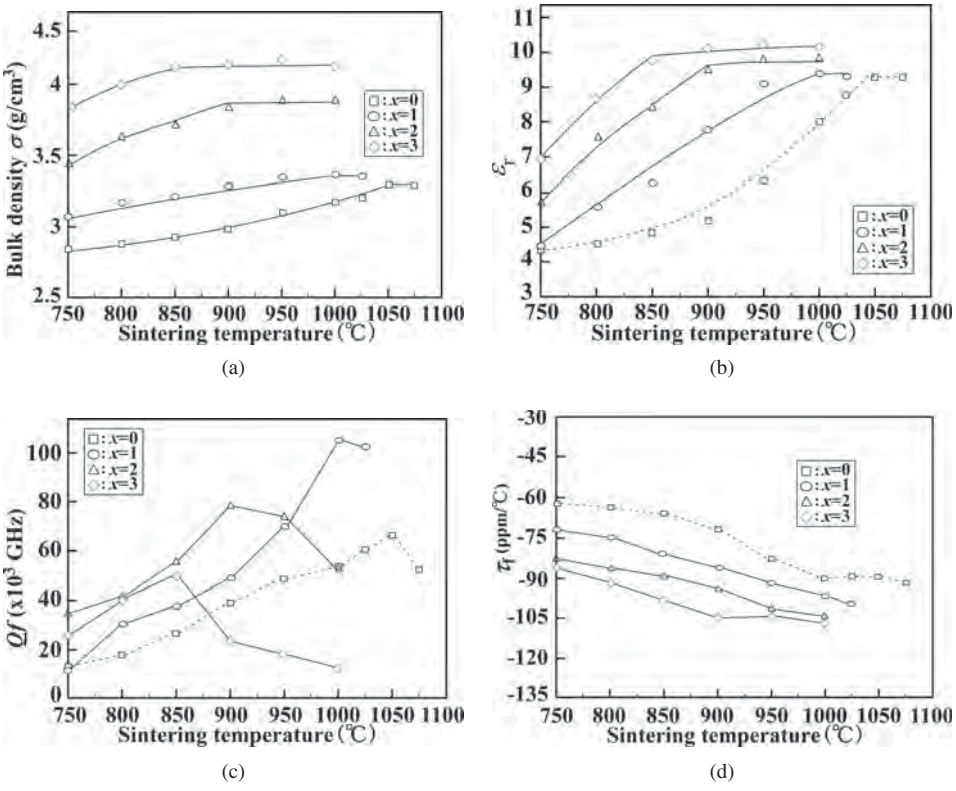

Figure 5.58 *The effects of Co substitution for Mg on (a) the bulk density, (b) ε_r, (c) Qf, and (d) τ_f of $(Mg_{3-x}Co_x)(VO_4)_2$ ceramics sintered for 5 h in air. Source: Umemura et al. 2005 [106].*

for $x = 1$ in the three figures. They depend on the amount of $Co_3(VO_3)_2$ ceramics, which form the liquid phase at approximately 850 °C. The ceramics with $x = 1$ exhibited the highest *Qf* value of > 100 000 GHz, lowest ε_r of 9.0, and $\tau_f = -90$ ppm/°C [106]. These solid solutions are excellent materials for LTCC because the composition of the ceramics could be selected depending of the sintering temperature.

Ogawa *et al*. [107] also reported $Mg_3(VO_4)_2$–$xBa_3(VO_4)_2$ ceramics with high *Qf* values, with near-zero τ_f by adding Li_2CO_3 as the sintering agent. Figure 5.59a, b, c, and d show, respectively, the density, ε_r, *Qf*, and τ_f as a function of composition x. The highest *Qf* value was obtained at $x = 0.2$, and is higher than 100 000 GHz, as shown in Figure 5.59c. The ε_r and τ_f values are 11.0, –58 ppm/°C, respectively. The near-zero τ_f value is obtained at $x = 0.5$. The variation of these values depend on the existence of the intermediate compound $BaMg_2(VO_4)_2$ and the high decompositional temperature of 1610 °C of $Ba_3(VO_4)_2$. Moreover, in order to reduce the sintering temperature, the sintering conditions are improved by adding Li_2CO_3. The $x = 0.5$ ceramics with 0.0625 wt% Li_2CO_3 exhibit good properties of $Qf = 74\,437$ GHz, $\varepsilon_r = 12.6$, $\tau_f = -5.8$ ppm/°C, which ceramics sintered at 950 °C for 5 hours in air [107].

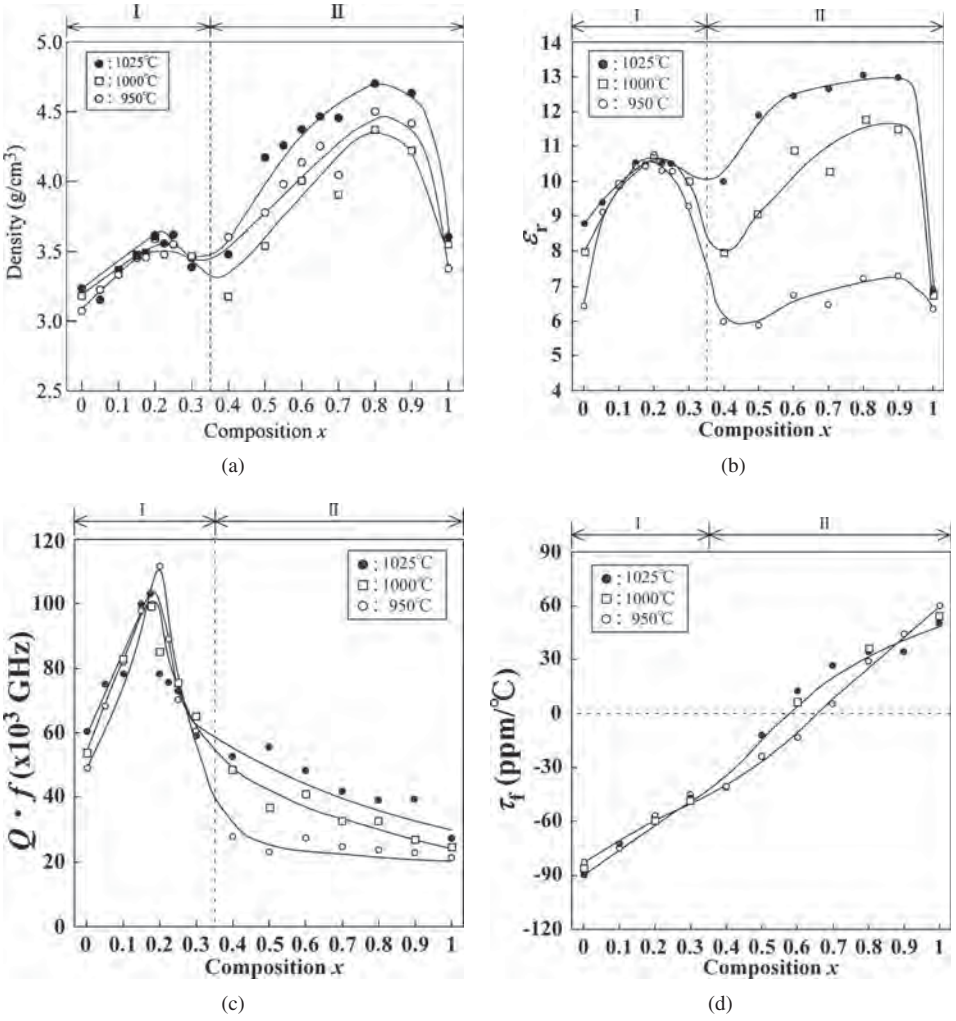

Figure 5.59 *(a) Bulk density, (b) ε_r, (c) Qf, and (d) τ_f of $Mg_3(VO_4)_2$–$xBa_3(VO_4)_2$ ceramics sintered at 950, 1000, and 1025 °C for 5 h in air. After Ogawa et al. [107]*

Acknowledgments

The author would like to thank Professors Hirotaka Ogawa and Akinori Kan at Meijyo University for preparing some data.

References

1. Editor (2013) Take off on WiGig! (in Japanese) *Nikkei Electronics* No. 1123 (December 9, 2013).

2. Ministry of Public Management, Home Affairs, Posts and Telecommunications in Japan. http://www.tele.soumu.go.jp/resource/search/myuse/use/ika.pdf, http://www.tele.soumu.go.jp/e/index.htm.
3. Editor (2008) What is a millimeter-wave? (in Japanese) *J-Net*. http://j-net21.smrj.go.jp/develop/digital/entry/001-20081119-06.html/ (accessed March 28, 2016).
4. Toyota News Release (in Japanese) (February 26, 2009).
5. Nikkei Electronics (2014) Millimeter wave forefront (in Japanese), Nikkei BP, ISBN: 978-4-8222-7694-2.
6. Fujimoto, M., Yasufuku, Y., Kan, A., *et al.* (2015) Low loss LTCC substrates for millimeter-wave application (in Japanese). Speech presented at the 150th Electronic Ceramic Process Meeting in Bannkokubashi Comvension Center, Yokohama, February 14, 2015.
7. Japan Fine Ceramics Center (2014) Development for high integration LTCC substrates with high Q and low dielectric constant (in Japanese). Report of Support Industrial Project 2014. METI, Japan, March 30, 2014.
8. Nakazawa, H. and Shimakata, Y. (2011) Forsterite- and willemite-based ceramic substrates with low thermal expansion coefficient and high thermal conductivity (IV) — The evaluation of MSL, BPF and the resonator for millimeter wave bands (in Japanese). Speech presented at IEICE Society Conference 2011, Hokkaido University, Sapporo, Japan, September 13–16, 2011.
9. Ohsato, H., Tsunooka, T., Kan, A., *et al*. (2004) Microwave-millimeterwave dielectric materials. *Key Engineering Materials*, **269**, 195–198.
10. Sebastian, M.T. (2008) *Dielectric Materials for Wireless Communication*, Elsevier Science Publishers, Amsterdam.
11. Kolar, D., Stadler, Z., Gaberscek, S., and Suvorov, D. (1978) Ceramic and dielectric properties of selected compositions in the $BaO–TiO_2–Nd_2O_3$ system. *Berichte der Deutschen Keramischen Gesellschaft*, **55**, 346–347.
12. Ohsato, H., Ohhashi, T., Nishigaki, S., *et al*. (1993) Formation of solid solutions of new tungsten bronze-type microwave dielectric compounds $Ba_{6-3x}R_{8+2x}Ti_{18}O_{54}$ (R = Nd and Sm, $0 < x < 1$). *Japanese Journal of Applied Physics*, **32** (9B), 4324–4326.
13. Ohsato, H., Ohhashi, T., Kato, H., *et al*. (1995) Microwave dielectric properties and structure of the $Ba_{6-3x}R_{8+2x}Ti_{18}O_{54}$ solid solutions. *Japanese Journal of Applied Physics*, **34**, 187–191.
14. Koga, E. and Moriwake, H. (2003) Effects of superlattice ordering and ceramics microstructure on the microwave Q factor of complex perovskite-type oxide $Ba(Zn_{1/3}Ta_{2/3})O_3$ (in Japanese). *Journal of Ceramic Society of Japan*, **111** (Suppl.), 767–775.
15. Ohsato, H., Koga, E., Kagomiya, I., and Kakimoto, K. (2010) Origin of high Q for microwave complex perovskite. *Key Engineering Materials*, **421-422**, 77–80.
16. Tohdo, Y., Kakimoto, K., Ohsato, H., *et al.* (2006) Microwave dielectric properties and crystal structure of homologous compounds $ALa_4Ti_4O_{15}$ (A = Ba, Sr and Ca) for base station applications. *Journal of the European Ceramic Society*, **26**, 2039–2043.
17. Ohsato, H. (2005) Microwave materials with high Q and low dielectric constant for wireless communications. *Proceedings of the Materials Research Society Symposium*, **833**, 55–62.
18. Ohsato, H., Tsunooka, T., Ohishi, Y., *et al*. (2003) Millimeter-wave dielectric ceramics of alumina and forsterite with high quality factor and low dielectric constant. *Journal of Korean Ceramic Society*, **40** (4), 350–353.
19. Tsunooka, T., Andou, M., Higashida, Y., *et al.* (2003) Effects of TiO_2 on sinterability and dielectric properties of high-Q forsterite ceramics. *Journal of the European Ceramic Society*, **23** (14), 2573–2578.
20. Tsunooka, T., Sugiyama, H., Kakimoto, K., *et al*. (2004) Zero temperature coefficient τ_f and sinterability of forsterite ceramics by rutile addition *Journal Ceramic Society of Japan*, **112** (Suppl.), S1637–S1640.
21. Ando, M., Himura, K., Tsunooka, T., *et al*. (2007) Synthesis of high-quality forsterite. *Japanese Journal of Applied Physics*, **46** (10B), 7112–7116.

22. Ando, M., Ohsato, H., Kagomiya, I., and Tsunooka, T. (2008) Quality factor of forsterite for ultrahigh frequency dielectrics depending on synthesis process. *Japanese Journal of Applied Physics*, **47** (9), 7729–7731.
23. Guo, Y., Ohsato, H., and Kakimoto, K. (2006) Characterization and dielectric behavior of willemite and TiO_2-doped willemite ceramics at millimeter-wave frequency. *Journal of the European Ceramic Society*, **26**, 1827–1830.
24. Ohsato, H., Kim, J.S., Kim, A.Y., *et al*. (2011) Millimeter-wave dielectric properties of cordierite/indialite glass ceramics. *Japanese Journal of Applied Physics*, **50** (9), 09NF01-1-5.
25. Ohsato, H., Kim, J.S., Cheon, C.I., and Kagomiya, I. (2013) Millimeter-wave dielectrics of indialite/cordierite glass ceramics: estimating Si/Al ordering by volume and covalency of Si/Al octahedron. *Journal Ceramic Society of Japan*, **121**, 649–654.
26. Kagomiya, I., Suzuki, I., and Ohsato, H. (2009) Microwave dielectric properties of $(Ca_{1-x}Sr_x)SiO_3$ ring silicate solid solutions. *Japanese Journal of Applied Physics*, **48**, 09KE02-1-4.
27. Ohsato, H., Terada, M., and Kawamura, K. (2012) Fabrication conditions of diopside for millimeterwave dielectrics. *Japanese Journal of Applied Physics*, **51** (9), 09LF02-1-4.
28. Ohsato, H., Kagomiya, I., Terada, M., and Kakimoto, K. (2010) Origin of improvement of Q based on high symmetry accompanying Si–Al disordering in cordierite millimeter-wave ceramics. *Journal of the European Ceramic Society*, **30**, 315–318.
29. Kajfez, D. and Guillon, P. (1998) *Dielectric Resonators*, 2nd edn, Noble Publishing Corporation, Atlanta, GA.
30. Miyauchi, T. (2008) Research for microwave–millimeter-wave alumina ceramics (in Japanese). Dr Thesis, Nagoya Institute of Technology, p. 29.
31. Ohsato, H. (2014) Design of microwave dielectrics based on crystallography, in *Advances in Multifunctional Materials and Systems II*, Ceramic Transaction 245 (eds J. Akedo, X.M. Chen, and T. Tseng), John Wiley & Sons, Inc., Hoboken, NJ, pp. 87–100.
32. Ohsato, H. (2016) Microwave dielectrics with perovskite-type structure, in *Perovskite Materials* (eds L. Pan and G. Zhu), INTEC, 2016, Croatia, Chapter 9. Open Access: http://cdn.intechopen.com/pdfs-wm/49723.pdf.
33. Surendran, K.P., Santha, N., Mohanan, P., and Sebastian, M. (2004) Temperature stable low loss ceramic dielectrics in $(1-x)\,ZnAl_2O_4$–$xTiO_2$ system for microwave substrate applications. *European Physical Journal, B*, **41**, 301–306.
34. Ohsato, H., Kato, K., Mizuta, M., *et al*. (1995) Microwave dielectric properties of the $Ba_{6-3x}(Sm_{1-y}, R_y)_{8+2x}Ti_{18}O_{54}$ (R = Nd and La) solid solutions with zero temperature coefficient of the resonant frequency. *Japanese Journal of Applied Physics*, **34** (9B), 5413–5417.
35. Ohsato, H., Ando, M., and Tsunooka, T. (2007) Synthesis of forsterite with high Q and near zero TCf for microwave/millimeterwave dielectrics. *Journal of Korean Ceramic Society*, **44** (11), 597–606.
36. Ohsato H. (2005) Research and development of microwave dielectric ceramics for wireless communications. *Journal of Ceramic Society of Japan*, **113**, 703–711.
37. Tsunooka, T., Sugiyama, T., Ohsato, H., *et al.* (2004) Development of forsterite with high Q and zero temperature coefficient τ_f for millimeterwave dielectric ceramics. *Key Engineering Materials*, **269**, 199–202.
38. Tsunooka, T., Ando, M., Suzuki, S., *et al*. (2013) Research and developments for millimeterwave dielectric forsterite with low dielectric constant, high Q, and zero temperature coefficient of resonant frequency. *Japanese Journal of Applied Physics*, **52** (9), 09KH02-1-4.
39. Massazza, F, and Sirchia, E. (1958) Phase diagrams for ceramics No.723, Dhim. Ind. (Milan), 40 466, 86.
40. Wu, P., Erikson, G., Pelton, A.D., and Blander, M. (1993) Prediction of the thermodynamic properties and phase diagrams of silicate systems – Evaluation of the FeO–MgO–SiO_2 system. *The Iron and Steel Institute of Japan International*, **33**, 26–35.
41. Dong, M., Yue, Z., Zhuang, H., *et al.* (2008) Microstructure and microwave dielectric properties of TiO_2 doped Zn_2SiO_4 ceramics synthesized through the sol–gel process. *Journal of American Ceramic Society*, **91**, 3981–3985.

42. Sebastian, M.T., Ubic, R., and Jantunen, H. (2015) Low-loss dielectric ceramic materials and their properties. *International Materials Review*, **60**, 395–415.
43. Kim, J.-S., Song, M.-E., Joung, M.-R., *et al.* (2010) Effect of B_2O_3 addition on the sintering temperature and microwave dielectric properties of Zn_2SiO_4 ceramics. *Journal of the European Ceramic Society*, **30**, 375–379.
44. Kim, J.-S., Song, M.-E., Joung, M.-R., *et al.* (2008) Low temperature sintering and microwave dielectric properties of V_2O_5 added Zn_2SiO_4 ceramics. *Journal of American Ceramic Society*, **91**, 4133–4136.
45. Dou, G., Zhou, D., and Gong, S. (2012) Low temperature sintered Zn_2SiO_4–$CaTiO_3$ ceramic with near zero temperature coefficient of resonant frequency. *Journal of Alloys and Compounds*, **513**, 466–473.
46. Suvorov, D. (2010) Contemporary materials for electronic applications, in *The 6th Microwave Materials and Their Applications*, Warsaw, Poland, September 1–4, 2010.
47. Ando, M., Ohsato, H., Igimi, D., *et al*. (2015) Low-temperature sintering of silica–boric acid-doped willemite and microwave dielectric properties. *Japanese Journal of Applied Physics*, **54**, 10NE03-1-6.
48. Miyashiro, A. (1957) Cordierite–indialite relations. *American Journal of Science*, **255**, 43–62.
49. Gibbs, G.V. (1966) Polymorphism of cordierite. I. Crystal structure of low cordierite. *American Mineralogist*, **51**, 1068–1087.
50. Wu, J.-M. and Huang, H.L. (2000) Effect of crystallization on microwave dielectric properties of stoichiometric cordierite glasses containing B_2O_3 and P_2O_5 glasses. *Journal of Materials Research*, **15**, 222–227.
51. Terada, M., Kawamura, K., Kagomiya, I., *et al*. (2007) Effect of Ni substitution on the microwave dielectric properties of cordierite. *Journal of the European Ceramic Society*, **27**, 3045–3148.
52. Izumi, F. and Ikeda, T. (2000) A Rietveld-analysis program RIETAN-98 and its applications to zeolites. *Materials Science Forum*, **321–324**, 198–203.
53. Toraya, H., Hibino, H., and Ohsumi, K. (1996) A new powder diffractometer for synchrotron radiation with multiple-detector system. *Journal of Synchrotron Radiation*, **3**, 75–83.
54. Brown, I.D. and Shannon, R.D. (1973) Empirical bond-strength–bond-length curves for oxides. *Acta Crystallographica*, **A29**, 266–282.
55. Brown, I.D. and Wu, K-K. (1976) Empirical parameters for calculating cation–oxygen bond valences. *Acta Crystallographica*, **B32**, 1957–1959.
56. Kagomiya, I. and Ohsato, H. (2014) Crystallized glass ceramic dielectrics for high frequency. Japanese Patent Application No. 2014-164285, filed August 12, 2014.
57. Yang, H. and Prewitt, C.T. (1999) On the crystal structure of pseudowollastonite ($CaSiO_3$). *American Mineralogist*, **84**, 929–932.
58. Nishi, F. (1997) Strontium metasilicate, $SrSiO_3$. *Acta Crystallographica*, **C53**, 534–536.
59. Moir, G.K. and Glasser, F.P. (1974) System $CaSiO_3$–$SrSiO_3$. *Transactions and Journal of the British Ceramic Society*, **73**, 199–206.
60. Pauling, L. (1980) The nature of silicon–oxygen bonds. *American Mineralogists*, **65**, 321–323.
61. Pauling, L. (1967) *The Chemical Bond*, Cornell University Press, New York, pp. 69–73.
62. Kittel, C. (1956) *Introduction to Solid State Physics*, 2nd edn, John Wiley & Sons, Inc., New York, p. 57.
63. Hannay, N.B. and Smith, C.P. (1946) The dipole moment of hydrogen fluoride and the ionic character of bonds. *Journal of American Chemistry Society*, **68** (2), 171–173. doi: 10.1021/ja01206a003.
64. Terada, M. (2007) Crystal structure and microwave dielectric properties of cordierite ceramics. Master Thesis, Nagoya Institute of Technology.
65. Wu, S. and Ma, Q. (2013) Synthesis characterization and microwave dielectric properties of Zn_2GeO_4. *Journal of Alloys and compounds*, **567**, 40–46.
66. Chen, C.X., Wu, S.P., and Li, J.H. (2013) Synthesis and microwave dielectric properties of B_2O_3 doped Mg_2GeO_4. *Journal of Alloys and Compounds*, **578**, 153–156.

67. Hurlbut, Jr, C.S., and Cornelis, K. (1971) *Manual of Mineralogy (after James D. Dana)*, 19th edn, John Wiley & Sons, Inc., New York, pp. 420–431.
68. Nishigaki, S., Yanao, S., Fukuta, J., *et al*. (1985) A new multilayered low temperature fireable ceramic substrate, in *Proceedings of International Symposium of Hybrid Microelectrics* (*ISHM*), Anaheim, CA, vol. 85, pp. 225–234.
69. Nishigaki, S., Fukuta, J., Yanao, S., Kawabe, H.K. Noda, and M. Fukaya (1986) A new low temperature fireable Ag multilayer ceramic substrate having post-fired Cu conductor, in *Proceedings of the International Symposium of Hybrid Microelectrics* (*ISHM*86), pp. 429–437.
70. Nishigaki, S. (2005) u-Hybrid as ECUs for next generation automotives using LTCC (LFC) material system (in Japanese). *Ceramics*, **40**, 137–123.
71. Krzmanc, M.M., Valant, M., Jancar, B., and Suvorov, D. (2005) Subsolidus synthesis and microwave dielectric characterisation of plagioclase feldspars. *Journal of American Ceramic Society*, **88**, 2472–2479.
72. Krzmanc, M.M., Meden, A., and Suvorov, D. (2007) The correlation between the structure and the dielectric properties of $K_xBa_{1-x}Ga_{2-x}Ge_{2+x}O_8$ ceramics. *Journal of the European Ceramic Society*, **27** (8–9), 2957–2961.
73. Krupka, J., Derzakowski, K., Tobar, M.E., *et al*. (1999) Complex permittivity of some ultralow loss dielectric crystals at cryogenic temperatures. *Measurement of Science and Technology*, **10**, 387.
74. Alford, N.Mc.N., Breeze, J., Wang, X., *et al*. (2001) Dielectric loss of oxide single crystals and polycrystalline analogues from 10 to 320 K. *Journal of the European Ceramic Society*, **21**, 2605–2611.
75. Huang, C.-L., Wang, J.-J., Yen, F.-S., and Huang, C.-Y. (2008) Microwave dielectric properties and sintering behavior of nano scaled $(\alpha + \theta)$–Al_2O_3 ceramics. *Material Research Bulletin*, **43**, 1463–1471.
76. Alford, N.McN,N. and Penn, S.J. (1996) Sintered alumina with low dielectric loss. *Journal of Applied Physics*, **80**, 5895–5898.
77. Miyauchi, Y., Ohishi, Y., Miyake, S., and Ohsato, H. (2006) Improvement of the dielectric properties of rutile-doped Al_2O_3 ceramics by annealing treatment. *Journal of the European Ceramic Society*, **26**, 2093–2096.
78. Levin, E.M. and McMurdie, H.F. (1975) Phase diagrams for ceramists. *American Ceramic Society*, **3**, 135.
79. Kan, A., Ogawa, H., and Ohsato, H. (2004) Relationship between bond strength and microwave dielectric properties of corundum type $(Mg_{4-x}Co_x)Nb_2O_9$ and $Mg_4(Nb_{2-y}Ta_y)O_9$ solid solutions. *Journal Ceramic Society of Japan*, **112** (Suppl. 1), S1622–S1626.
80. Ogawa, H., Kan, A., Ishihara, S., and Higashida, Y. (2003) Crystal structure of corundum type $Mg_4(Nb_{2-x}Ta_x)O_9$ microwave dielectric ceramics with low dielectric loss. *Journal of the European Ceramic Society*, **23**, 2485–2488.
81. Ogawa, H., Taketani, H., Kan, A., *et al*. (2005) Evaluation of electronic state of $Mg_4(Nb_{2-x}Sb_x)O_9$ microwave dielectric ceramics by first principal calculation method. *Journal of the European Ceramic Society*, **25**, 2859–2863.
82. Kumada, N., Taki, K., and Kinomura, N. (2000) Single crystal structure refinement of a magnesium niobium oxide: $Mg_4Nb_2O_9$. *Materials Research Bulletin*, **35**, 1017–1021.
83. Adachi, H., Shiokawa, S., Tsukada, M., *et al*. (1979) Discrete variational Xα cluster calculations. III. Application to transition metal complexes. *Journal of the Physical Society of Japan*, **47**, 1528–1537.
84. Adachi, H., Tsukada, M., and Satoko, C. (1978) Discrete variational Xα cluster calculations. I. Application to metal clusters, *Journal of the Physical Society of Japan*, **45**, 875–883.
85. Surendran, K.P., Bijumon, P.V., Mohanan, P., and Sebastian, M.T. (2005) $(1-x)MgAl_2O_{4-x}TiO_2$ dielectrics for microwave and millimeter wave applications. *Applied Physics*, **A81**, 823–826.

86. Wu, X., Xue, J., Wang, R., and Li, J. (2014) Synthesis, characterization and microwave dielectric properties of spinel $MgGa_2O_4$ ceramic material. *Journal of Alloys and Compounds*, **585**, 542–548.
87. Xue, J., Wu, S., and Li, J. (2013) Synthesis microstructure and microwave dielectric properties of spinel ZnGa2O4 ceramics. *Journal of American Ceramic Society*, **96**, 2481–2485.
88. Kan, A., Takahashi, S., Moriyama, T., and Ogawa, H. (2014) Influence of Zn substitution for Mg on microwave dielectric properties of spinel-structured $(Mg_{1-x}Zn_x)Ga_2O_4$ solid solutions. *Japanese Journal of Applied Physics*, **53**, 09PB03.
89. Putnis, A. (1992) *Introduction to Mineral Sciences*, Cambridge University Press, 134 pp.
90. Hahn, T. (ed.) (2002) *International Table for Crystallography*, vol. A, *Space-Group Symmetry*, 5th edn, Published for The International Union of Crystallography (IUCr) by Kluwer Academic Publishers, Dordrecht, pp.696–703.
91. Kan, A., Moriyama, T., Takahashi, S., and Ogawa, H. (2013) Cation distributions and microwave dielectric properties of spinel-structured $MgGa_2O_4$ ceramics. *Japanese Journal of Applied Physics*, **52**, 09KH01.
92. Hill, R.J., Craig, J.R., and Gibbs, G.V. (1979) Systematics of the spinel structure type. *Physics and Chemistry of Minerals*, **4**, 317–339.
93. Surendran, K.P., Sebastian, M.T., Manjusha, M.V., and Philip, J. (2005) A low loss, dielectric substrate in $ZnAl_2O_4$–TiO_2 system for microelectronic applications. *Journal of Applied Physics*, **98**, 44101.
94. Mori, N., Sugimoto, Y., Harada, J., and Higuchi. Y. (2006) Dielectric properties of new glass-ceramic for LTCC applied to microwave or millimeter-wave frequencies. *Journal of the European Ceramic Society*, **26**, 1925–1928.
95. Nishizuka, M., Ogawa, H., Kan, A., and Sugino, M. (2009) Synthesis and microwave dielectric properties of MgO–x mol% B_2O_3 (x = 33 and 25) ceramics in MgO–B_2O_3 system. *Ferroelectrics*, **388**, 101–108.
96. Dosler, U., Krzmanc, M.M., Jancar, B., and Suvorov, D. (2011) A high Q microwave dielectric materials based on $Mg_3B_2O_6$. *Journal of American Ceramic Society*, **93**, 3788–3792.
97. Dosler, U., Krzmanc, M.M., and Suvorov, D. (2010) The synthesis and microwave dielectric properties of $Mg_3B_2O_6$ and $Mg_2B_2O_5$ ceramics. *Journal of the European Ceramic Society*, **30**, 413–418.
98. Wu, X.G., Wang, H., Chen, Y.H., and Zhou, D. (2012) Synthesis and microwave dielectric properties of $Zn_3B_2O_6$ ceramics for substrate applications. *Journal of American Ceramic Society*, **95**, 1793–1795.
99. Takada, T., Yamamoto, H., and Kageyama, K. (2003) Synthesis and microwave dielectric properties of $x$$Re_2O_3$–$y$$B_2O_3$ (Re = La, Nd, Sm, Dy, Ho and Y) compounds. *Japanese Journal of Applied Physics*, **42**, 6162–6167.
100. Chen, X.M., Bai, S., Li, M., and Zhang, W. (2013) Synthesis, characterization and dielectric properties of low loss $LaBO_3$ ceramics. *Journal of the European Ceramic Society*, **33**, 3001–3006.
101. Zachariasen, W.H. (1948) The crystal structure of the normal orthophosphates of barium and strontium. *Acta Crystallographica*, **1**, 263–265.
102. Abhilash, P., Thomas, D., and Sebastian, M.T. (2013) Sintering and microwave dielectric properties of $AlPO_4$–MgF_2 ceramic composites. *International Journal of Modern Physics*, Conference Series **22**, 159–163.
103. Thomas, D. and Sebastian, M.T. (2010) Temperature compensated LiMgPO4: a new glass free low temperature cofired ceramic. *Journal of American Ceramic Society*, **93**, 3828–3831.
104. Bian, J.J., Kim, D.W., and Hong, K.S. (2005) Glass free LTCC microwave dielectric ceramics. *Materials Research Bulletin*, **40**, 2120–2129.
105. Cho, I.S., Choi, G.K., An, J.S., *et al*. (2009) Sintering microstructure and microwave dielectric properties of rare earth phosphates $RePO_4$ (Re = La, Ce, Nd, Sm, Tb, Dy, Y, Yb). *Materials Research Bulletin*, **44**, 173–178.

106. Umemura R., Ogawa, H., Ohsato, H., *et al.* (2005) Microwave dielectric properties of low temperature sintered $Mg_3(VO_4)_2$ ceramics. *Journal of the European Ceramic Society*, **25**, 2865–2870.
107. Ogawa, H., Yokoi, A., Unemura, R., and Kan, S. (2007) Microwave dielectric properties of $Mg_3(VO_4)_2$–$xBa_3(VO_4)_2$ ceramics for LTCC with near zero temperature coefficient of resonant frequency. *Journal of the European Ceramic Society*, **27**, 3099–3104.